Alma Mater Studiorum - University of Bologna

ARCES - Advanced Research Center on Electronic Systems for Information and Communication Technologies E. De Castro

PhD Course in Information Technologies

XXIV CYCLE - Scientific-Disciplinary sector ING-INF /01

CONTINUOUS FLOW SINGLE CELL SEPARATION INTO OPEN MICROWELL ARRAYS

Candidate: **Enri Duqi**

PhD course coordinator: **Prof. Claudio Fiegna**

Advisor: **Prof. Eleonora Franchi Scarselli**

Prof. Roberto Guerrieri

Dr. Massimo Bocchi

Final examination year: 2012

A Francesca

Table of Contents

List of figures

List of tables

1 Introduction

Summary: The first chapter introduces the main aspects related to this thesis. Initially we describe the origins and the motivations which led to the birth of the miniaturized systems world for biological applications. An overview of the state of the art and of the best achievements for cell trapping and dielectric analysis is then presented. The motivations and the objectives of this research are further disclosed followed by the whole manuscript outline.

1.1 Microfluidics platforms for single cell analysis

Research on microfluidic devices has its origin about 30 years ago and was a result of a new fabrication technology named micromechanics or microfabrication which permits to produce miniaturized systems layer by layer with micrometric resolution. The first examples of microfluidic systems were developed at Stanford University (Terry, Jerman, & Angell, 1979) and at IBM (Bassous, Taub, & Kuhn, 1977). A gas chromatograph and ink jet printer nozzles were the prototypes, respectively.

Driven from the silicon microprocessors industry, the microfabrication technology grew rapidly and photolithography, which is one of its fundamental techniques, was well suited for the production of micro-electro-mechanical systems (MEMS) in which the mechanical functions were combined with the electrical ones (Whitesides, 2006). Some MEMS chemistry applications were also based on hydro-mechanical forces by including the presence of fluids thus creating the first examples of microfluidic systems (Duffy, McDonald, Schueller, & Whitesides, 1998).

The interest on the integration of fluids is related to the possibility of carrying or dragging substances such as proteins in fluids. The analysis of more complex biological systems such as living cells, within microfluidic platforms, is very attractive for the large number of applications (Et Ali, Sorger, & Jensen, 2006). As pointed out from Andersson & Van der Berg, (Andersson & Van der Berg, 2003) the main advantages of microfluidic platforms for cellomics are the small volume of reactants, the possibility to integrate all kinds of standard analytes and to manipulate large numbers of cells simultaneously. Further, using small geometries gives the possibility to reach large electrical field strengths

with small voltages which permits to manipulate cells singularly. Heat and mass transfer are also very fast in microfluidic systems enabling, for instance, efficient DNA amplification *via* Polymerase Chain Reaction.

Moreover, separation and analysis of different cell cultures are essential steps for biological research, chemical diagnostics and in health science. In drug discovery, for instance, an important advance is offered by the miniaturization of entire systems with the introduction of high-density plates and nanolitre dispensing systems to allow automated handling of small liquid volumes for high-throughput analysis.

The miniaturization resulting from the progress introduced by electronics and microtechnology is advantageously exploited (Feynman, 1992) to develop new integrated methods for cell separation. Today, most famous universities and companies (Dittrich & Manz, 2006), (Clayton, 2005) investigate on new microfluidic platforms capable of providing solutions to many interesting problems of health-care and life sciences. To date more than 15000 papers have been published in the field of microfluidics and this number is continuously increasing[1]. Microfluidics is emerging and conquering an extensive field of applications in cell biology, neurobiology and pharmacology since much of these technologies require the manipulation of fluids.

In the cellomics field four main stages can be distinguished in the cell analysis process (Andersson & Van der Berg, 2003): (1) cell sampling, (2) cell trapping and cell sorting, (3) cell treatment which can be divided in: cell lysis, electroporation and cell fusion subcategories, (4) and on- or off-chip cell analysis.

This thesis work is included in the second category and involves the separation of cells by means of mechanical and electrical based techniques. The aim of this study is to develop and characterize a method to selectively isolate single-cells. These functions (cell selection and isolation) are implemented in a microfluidic platform, developed in our group, which allows further treatment and analysis for the discovery of microscale phenomena occurring in cells. Before describing the objectives of this work in the following sections 1.2 and 1.3 the state of the art of the devices for cell separation and cell detection, respectively, is presented.

[1] ISI web of knowledge; search topic: “Microfluidics”

1.2 On-chip continuous trapping and separation of bioparticles: state of the art

1.2.1 Single cell trapping and separation techniques

Among the current methods commonly used for the manipulation and separation of bioparticles in biological laboratories and research groups, those based on hydrodynamics, optical tweezers, magnetic or fluorescence activated cell sorting, filtration and electric field-based methods can be mentioned. In this section we present the state of the art of miniaturized concepts for single cells' trapping and sorting.

1.2.1.1 Hydrodynamic and mechanical trapping

Mechanical trapping of biological particles in a microchip poses several challenges related to cells' heterogeneous size and properties. Furthermore, the applications are different and numerous and this adds further unknown elements to the problem.

Microfabricated mechanical filters have been used for trapping different cell types from blood. Carlson et al. (Carlson, Gabel, Chan, & Austin, 1997) presented an array of channels with dimensions that freely permitted red blood cells to penetrate through the lattice while blocking the white cells whose diameter is about 50% larger. In Figure 1 some other techniques presented in the literature for single or multiple cell trapping are reviewed. The most common way for cell trapping is the use of lateral channels patterned on a main flow channel also known as patch clamping. The section of the side channels should be small enough to block cells by suction. In Figure 1.a the structure proposed from (Lee, Hung, Shaw, Jan, & Lee, 2005) is presented. Two NIH3T3 fibroblasts cells can be trapped simultaneously and membrane contact is demonstrated by fluorescent dye transfer. Slanted rows of blocking elements arrays with a recess (Di Carlo, Wu, & Lee, 2006) shown in Figure 1.b were designed to trap single cells. This structure was also used to perform single HeLa cell perfusion cultures as shown in Di Carlo et al. (Di Carlo, Wu, & Lee, 2006). In a similar structure (Skelley, Kirak, Suh, Jaenisch, & Voldman, 2009) but with a double recess, cell pairing is performed in the same trap after loading the cells in two subsequent steps characterized from opposite flow direction (Figure 1.c). The claimed load operation efficiency was 70%.

Deep reactive ion etching (DRIE) was used in (Andersson, Van der Wijngaart, Enoksson, & Stemme, 2000), (Figure 1.d) in order to fabricate a filter whose walls are made from silicon bars. The volume of the microreactor is well suited to trap multiple beads and cells.

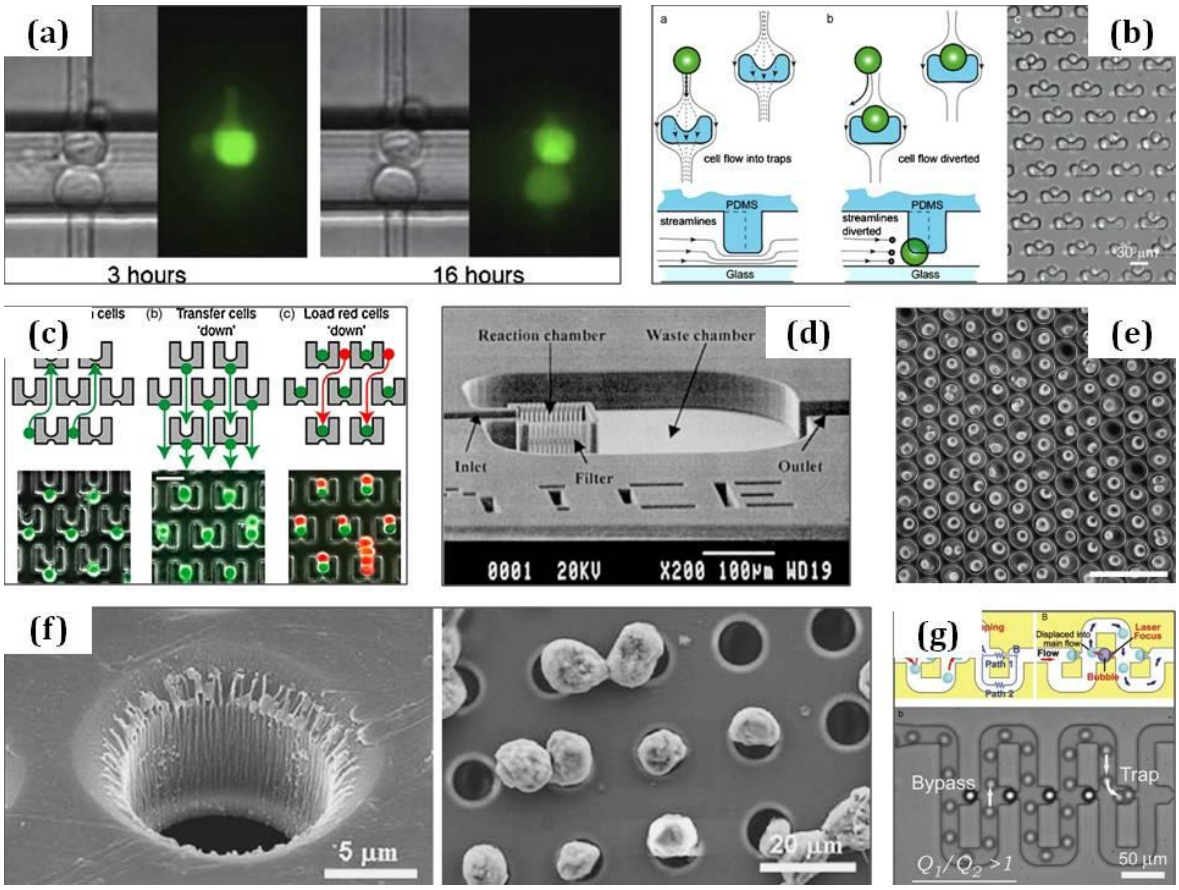

Figure 1. Hydrodynamical traps for cells. (a)20µm wide flow channel with 2x2µm^2 side channels for particle trapping. Picture reprinted from (Lee, Hung, Shaw, Jan, & Lee, 2005). Single cell trapping array from (Di Carlo, Aghdam, & Lee, 2006) (b). Similar with the previous array of mechanical traps for cell pairing (Skelley, Kirak, Suh, Jaenisch, & Voldman, 2009)(c). In (d) silicon bars filter from (Andersson, Van der Wijngaart, Enoksson, & Stemme, 2000) (e) (Rettig & Folch, 2005)PDMS microwell array, (f) (Zheng, et al., 2007), (g) (Tan & Takeuchi, 2007)

Rettig et al. (Rettig & Folch, 2005) described a Polydimethylsiloxane (PDMS) molded microwell array with varying dimensions and demonstrated an efficiency of 85% for single fibroblast cells. In Figure 1.f a very similar array was realized in parylene with reactive ion etching with holes of 10µm with a pitch of 20µm for a total of 16000 trapping sites on 6mm x 6mm area. An example of providing a massively parallel format, yet with individual addressing is presented in Figure 1.g by (Zheng, et al., 2007).

1.2.1.2 Optical and electrical trapping

In optical trapping a tight focused laser beam is used to trap and manipulate particles with high precision. The Gaussian profile of the laser beam constrains the particles to be drawn in the center of the beam. A representative example of this category of manipulators is presented by Arai et al (Arai, et al., 1999) where optical tweezers were used to tie knots with DNA filaments.

Another approach for isolation of single cells is the use of electrical fields. Among these solutions we can distinguish negative (nDEP) (Schnelle, Hagedorn, Fuhr, Fiedler, & Müller, 1993), positive (pDEP) (Taff & Voldman, 2005) and insulator based dielectrophoresis (iDEP) (Cummings & Singh, 2003). The pDEP trapping microsite is visualized in Figure 2. The so-called ring-dot geometry consists of an outer ring electrode and an inner round electrode on separated metal layers. Cells are attracted *via* positive dielectrophoresis to the field maximum corresponding to the central area of the site. The main advantage of this geometry is that the number of control electrodes scales with a factor of $2\sqrt{n}$, where n is the number of traps.

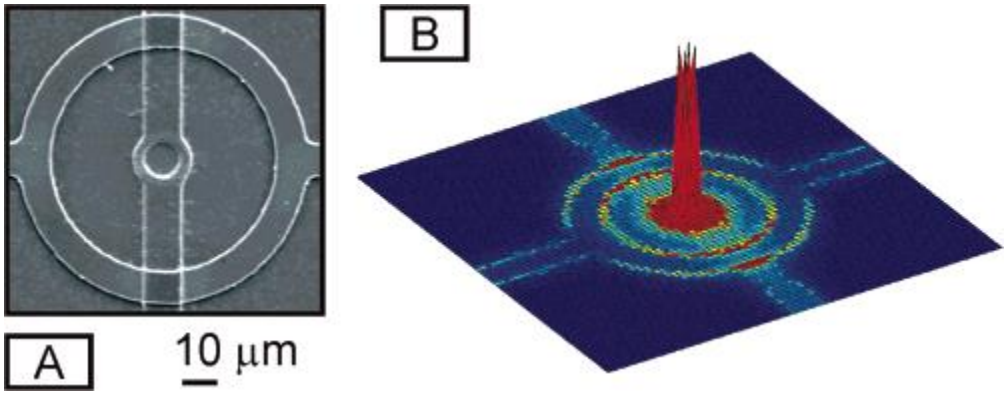

Figure 2. Positive DEP trapping microsite using ring electrodes. Adapted from (Taff & Voldman, 2005). (a) Top view of the measurement site which consists of an outer ring electrode and an inner round electrode on separated metal layers. (b) Electric field distribution within the structure.

Most of the aforementioned hydrodynamic techniques are characterized from a statistical approach to cell trapping and furthermore they fail to address the issue of cell recovery after processing. The only exception (Tan & Takeuchi, 2007) which offers the possibility of individual addressing of cells, presents the limitation of a single-cell trap. Isolation of a controllable and arbitrary number of cells or creation of cells' clusters is not possible.

A major drawback of the electrical field based methods is related to the fact that when trapped in DEP cages, particles are subjected to continuous stress in terms of temperature and transmembrane potential, (Arnold, 2001), (Rosenthal & Voldman, 2005) (Abonnenc, et al., 2005).

In the presented research, the combination of nDEP and hydrodynamic forces has been selected as the cells' separation principle. By contrast with pDEP, nDEP force offers the vantage of pushing the particles towards regions where the electric field intensity is lower reducing thus thermal stress on living cells. The micrometric site where cells are isolated is a microwell opened from both sides and no electric field is needed to keep the cells blocked. The number of the cells that can be isolated is programmable; cells are individually selected and different types of cells can be put in contact (Bocchi, et al., 2012).

1.3 Methods for cell detection in miniaturized devices: state of the art

Cell based impedance spectroscopy in miniaturized systems for cell analysis fulfills many conditions required by modern diagnostics. In addition to the advantages brought by miniaturization such as low consumption of reagents and analytes, reduced diffusion time, fast mass and heat transfer, dielectric spectroscopy features label-free particle monitoring. Traditional techniques, instead, use labeling with fluorochrome tagged reagents which may perturb the biological system and affect the cell physiology. Moreover, combining impedance cell identification with subsequent sorting of cells of interest can contribute to applications as stem cell migration (Linderholm, Braschler, Vannod, Barrandon, Brouard, & Renaud, 2006) and toxicity kinetics (Jahnke, et al., 2009), (Krinke, Jahnke, Mack, Hirche, Striggow, & Robitzki, 2010), (Meissner, Eker, Kasi, Bertsch, & Renaud, 2011).

According to their principle of analysis, impedance based cytometers can be grouped in surface impedance analyzers whose chips are equipped with electrodes covering the surface of the detection area where cells rest or adhere, and single cell flow cytometers. Both categories perform measurements in population of cells but the flow cytometers present the advantage of single-cell interrogation.

Other label free techniques rather than impedance include Raman spectroscopy, near infrared spectroscopy and photoacoustic cytometry (Galanzha, Shashkov, Tuchin, Zharov, & ., 2008), (Lee E, 2006), and (Watson DA, 2008).

The presented work involves the use of both optical and impedance based methods. The former was included in the first version of the automated delivery of cells into microwell arrays. Fluorescence analysis is so far the most popular approach for high-sensitivity detection of cells. However, impedance based cell analysis is implemented as well in this research because of the advantages offered by electric signals in terms of processing and recording with respect to optical ones which need light sources and detectors. This method, compared to the optical one, offers the advantage of parallel processing which is substantial for a high throughput delivery. The drawback of positional dependence is addressed by the combination of the sensing modules with dielectrophoretic focusing stages. Furthermore, because of the label-free nature of impedance analysis, it seems to have the best chance for miniaturized devices in the future in a broad range of applications.

1.4 Thesis motivations and objectives

A microfluidic platform whose functionalities can be used for the analysis of living cells and address some of the open issues described above is presented. More in detail the problems to be dealt with are:

- High-throughput isolation of a programmable number of cells (varying from one to a small cluster). Fast loading of a controlled number of cells in the array of microwells enables parallel analysis which is fundamental for a range of applications.
- On-chip fluid suspension change. Cell resuspension enables online treatment of the studied cell population and permits also to implement fluorescent based labeling techniques which offer high sensitivity detection.

- Analysis cell-cell interactions on-chip can last up to hours. A low stress biocompatible environment for isolated bioparticles is required.
- Selective recovery of the analyzed samples with high parallelism. Retrieving the contents of each microwell for further analysis enables the possibility of further off-chip processing of cells e.g. viability assessment, creation of cultures of cells that are all clones of a unique parent cell etc.

In the microfluidic platform, developed in our group, four main stages in the process of cell analysis can be listed: (1) trapping, (2) treatment, (3) analysis and (4) recovery of cells. The presented structure is based on a microwell open from both sides. Multiple microwells are arranged in arrays, which, in addition to the isolation of a controlled number of cells enable parallel analysis of cell-cell or cell-substances interactions. These substances can be added in the suspension fluid which can be changed during the experiments while the cells are trapped. Further, optical analysis is possible within the trapping microsites and the content of the microwell can be retrieved in parallel into standard laboratory microtiter plates.

(1) **Selective trapping:** *Controlled isolation of cells with single cell resolution.*
Similarly to microarrays often reported in literature, we aim to create a microwell array by through-holes drilling in a flexible printed circuit board substrate (*Flexible PCB*). Electrically active microchannels provide the cells' transport over the microwells. Trapping is performed by the combination of nDEP forces generated between metal electrodes and mechanical isolation into microwells.

(2) **Cell treatment:** *Automated fluid substitution and cells' exposure to reagents*. Fluid replacement in the microchannel is supported after cell isolation in the microwells permitting thus the introduction of different cell populations and a series of operations for cell analysis such as on-chip centrifuge of single-cells and cell-cell contact with a controlled number of cells.

(3) **Cell analysis:** *Electric field free biocompatible isolation sites.*

After being isolated and exposed to other cells and/or reagents, cells rest on the fluid's air interface meniscus in a biocompatible and low electric field intensity region. This allows performing experiments that may last up to several hours.

(4) **Sample recovery:** *Transfer of cells into standard microtiter plates.*

Thanks to the open microwell structure, cells can be transferred in parallel into a microtiter plate for further culturing and/or experiments. This step allows for selective investigation on particles on whose response we are interested. The microwell array ensures geometrical compatibility with the microtiter plate and at the same time enables cross-contamination free recovery of biological samples

The main objective of the presented thesis work is the development of a method for selective trapping of single cells into microwells. In a first prototype, the isolation principle is based in a traditional approach which involved the presence of motorized parts in the system to align each microwell of the array to an external picolitre droplet dispenser. Then, a new self-contained design based on dielectrophoretic forces capable to convey flowing cells versus isolation microwells is implemented.

The cells introduction is controlled by an optical detection method which enables automated cell delivery with single cell resolution. Optical methods for cell delivery involve the use of the microscope thus limit the parallelism of the method. To increase the delivery parallelism an alternative technique based on impedance measures was then developed.

1.5 Structure of this thesis

This dissertation is divided in 6 chapters. Besides the state of the art of the microfluidics for the continuous flow separation and impedimetric detection of cells presented above, in Chapter 2 the theoretical aspects of microfluidics and dielectric dispersions are shown. Then the electrical models of the biological particles used in this study are described in order to introduce the concepts of dielectrophoretic force and dielectric spectroscopy.

In Chapter 3, a first design approach to the open microwell array for single-cell separation is presented, with particular attention to the aspects studied in this thesis which are related to the development of a method for the isolation of single-cells in open microwells by means of external tools. The main achievements are summarized at the end of this chapter.

Chapter 4 is dedicated to an improved design with electrically active microchannels for the isolation of biological cells into open microwells. The modeling, the design and the experimental tests of the functional blocks, contained in the device and without involving external tools in this case, for the isolation of single cells into microwells are then disclosed. The optical method for the detection of flowing particles is also described in this chapter. This new separation method consists of aligning a stream of cells/particles in the central region of the microchannel followed by their successive individual isolating. Conclusions follow at the end of this chapter.

In chapter 5 a multifrequencial impedance based technique for impedance measurements of single cells in continuous flow is presented. This activity has been carried out at the *Microsystems Laboratory 4* at the *EPFL (École Polytechnique Fédérale de Lausanne)* working on a different microfluidic platform. The implemented method uses multiple signals at different frequencies in order to extract the dielectric properties of particles over the frequency spectrum. In this way particles are not only detected but also their internal structure can be probed permitting thus to analyze their status from a dielectric point of view. We first show the microfluidic platform in which the impedance measurement method is integrated. The "liquid electrode" concept is also presented as a valid alternative to traditional faced electrodes in a microchannel, featuring a simpler fabrication technology. As an example a particular application of dielectric spectroscopy related to the cell response to a toxin is described. The first measurements with polystyrene beads and mammalian cells for device calibration are then presented. The main achievements

obtained with this device for measuring the kinetics of the response of mammalian cells to the effect of pore forming toxins are finally shown.
Finally, conclusions on the presented thesis work are listed in Chapter 6.

2 Theoretical background

Summary: In this chapter the main theoretical aspects of microfluidics involved in the manipulation of particles by means of microchannels. The dielectric modeling of biological particles in suspension follows, in order to describe the physical phenomena on which AC electrokinetics and impedance spectroscopy rely. The lock-in amplifying method for the retrieving of small currents at known frequency used to single out the cells' dielectric properties is then presented.

2.1 Basic concepts in microfluidics

Scaling down the traditional laboratory setup characteristic dimension by a factor of 1000 presents several advantages. The more obvious is the reduced quantity of the samples' volume which scales as l^3 where l is the linear reduction. Handling small volumes is convenient because of the short diffusion distances which enable fast analysis. Moreover, system miniaturization offers the possibility to develop portable and cost-effective platforms.

The physical phenomena that dominate at the microscale level have to be understood in order to explain how the devices' functioning is made possible. In this section, the physics of microfluidics are reviewed and several applications are referenced to describe the state of the art for microfluidic devices.

Scaling laws express the variation of physical quantities with the characteristic length l of the given system or object, while keeping other physical quantities constant. In (Bruus, 2007) a summary of a number of key physical quantities involved in microfluidics are listed. A significant example for scaling is the ratio between surface forces (e.g. surface tension) and volume forces (e.g. gravity) that scale as:

$$\frac{surface\ forces}{volume\ forces} \propto \frac{l^2}{l^3} = l^{-1} \underset{l \to 0}{\rightarrow} \infty \qquad \textbf{[1]}$$

For fluids in structures of micrometric scale, surface tension becomes dominant over gravity. Other important effects in microfluidics for microparticles suspensions are creeping (laminar) flow which depends on the Reynolds number and is described by the

Stokes equation, the drag force on the particles and their sedimentation velocity, and the capillary action (Beebe, Mensing, & Walker, 2002).

2.1.1 The Navier-Stokes equation and the dimensionless Reynolds number

A very important parameter in fluid mechanics of the incompressible Newtonian fluid flows is the dimensionless Reynolds number defined as:

$$Re = \frac{\rho_{fluid} \cdot U \cdot L}{\mu} \quad \textbf{[2]}$$

where ρ_{fluid} is the fluid density, μ is its viscosity, U is a characteristic velocity scale factor and L is a characteristic length scale factor. Both depend on the specific problem geometry. For a simple geometry such as a rectangular section tube the characteristic scales are easily defined: U is the average flow velocity in the pipe, and L is the hydraulic diameter.

In general, the Reynolds number represents the ratio between the inertial effects and the viscous effects in the flow. The flow can get turbulent when inertial effects are dominant over viscous terms, which means $Re >> 1$. In contrast, for small Reynolds number, the flow will be laminar.

The fluid mechanics is described by the Navier-Stokes equation that describes the evolution of the velocity vector field (Bruus, 2007) :

$$\frac{\partial \vec{v}}{\partial t} + (\vec{v} \cdot \nabla)\vec{v} = -\frac{1}{\rho}\nabla p + \frac{\eta}{\rho}\nabla^2 \vec{v} \quad \textbf{[3]}$$

where $\vec{v}$ is the velocity vector, η is the fluid constant dynamic viscosity and p is the pressure. The first term on the left side is the unsteady (time-dependent) inertial component and the second term is the non-linear inertial term. On the right hand, the first term is the driving pressure gradient, and the final term is related to viscous dissipation.

We transform equation [3] by scaling its terms by the characteristic quantities U, L defined above. Hence, the velocity $\vec{v}$ scales with U ($\vec{v} = U \cdot \overline{\overline{\vec{v}}}$), the spatial derivative ∇ scales with *1/L* ($\nabla = \frac{1}{L} \cdot \overline{\overline{\nabla}}$), and the time *t* scales with *L/U*. Therefore, $\frac{\partial \vec{v}}{\partial t}$ scales as $\frac{\mathrm{U}^2}{\mathrm{L}}$, *and* in the same way scales $(\vec{v} \cdot \nabla)\vec{v}$, the dissipative viscous term scales as $\frac{\eta}{\rho}\frac{\mathrm{U}}{\mathrm{L}^2}$, while the pressure gradient term scales as $\frac{\eta U}{L^2}$.

The Navier-Stokes equation [3] can be rewritten by introducing the scaling expression for each term:

$$\frac{U^2}{L}\frac{\overline{\overline{\partial \vec{v}}}}{\partial t} + \frac{U^2}{L}\overline{\overline{(\vec{v} \cdot \nabla)\vec{v}}} = -\frac{\eta U}{L^2}\frac{1}{\rho}\overline{\overline{\nabla p}} + \frac{\eta}{\rho}\frac{\mathrm{U}}{\mathrm{L}^2}\overline{\overline{\nabla^2 \vec{v}}} \qquad \textbf{[4]}$$

In this equation all the accented terms $\overline{\overline{\cdot}}$ are dimensionless and it can be reorganized as:

$$Re \cdot \left[\overline{\overline{\frac{\partial \vec{v}}{\partial t}}} + \overline{\overline{(\vec{v} \cdot \nabla)\vec{v}}}\right] = -\overline{\overline{\nabla p}} + \overline{\overline{\nabla^2 \vec{v}}}, \qquad \text{where} \quad Re = \frac{\rho UL}{\eta} \qquad \textbf{[5]}$$

For small dimensionless Reynolds number ($Re = \frac{\rho UL}{\eta} \ll 1$) or in the case of small fluid velocities U, the inertial terms are smaller than the viscous terms which, in the case of microfluidics derive from the small length scales L. In these conditions, the linear equation known as the Stokes equation is valid to describe the fluid flow:

$$0 = -\overline{\overline{\nabla p}} + \overline{\overline{\nabla^2 \vec{v}}} \qquad \textbf{[6]}$$

This equation is not time-dependent (except for a problem case with time-dependent boundary conditions). It is linear thus the response of a Stokes flow will be proportional to the forces applied to it. We remind also that the above derivation is valid for the case of incompressible Newtonian fluid flows.

The Reynolds number can be also defined for an object in a fluid, called the particle Reynolds number. In our application this number is important for predicting

microparticles' sedimentation velocity and drag forces which are introduced in the next section.

2.1.2 Drag on a spherical particle in suspension

Stokes derived an expression in 1851 for a friction force also named drag force that a laminar flow exerts on homogeneous spherical particles with a small Reynolds number. This expression is very useful in microfluidics applications where particles such as biological cells, can be approximated as spherical.

$$\vec{F}_{Drag} = 6\pi\eta R\vec{v}_{fluid} \quad \textbf{[7]}$$

where *R* is the particle radius, $\vec{v}_{fluid}$ is the fluid vector velocity and η its viscosity.

When the buoyancy effects are taken into account, particles in suspension with mass density greater than that of the surrounding fluid will fall due to their weight, with a terminal velocity named settling or sedimentation which is reached when the net force acting on the particle becomes zero. When the terminal velocity is reached the weight of the particle:

$$\vec{F}_G = \frac{4\pi R^3 \rho_p g}{3} \quad \textbf{[8]}$$

is exactly balanced by the drag force and the difference upward buoyancy force:

$$\vec{F}_B = \frac{4\pi R^3 \rho_m g}{3} \quad \textbf{[9]}$$

the settling velocity is reached. By imposing that the sum of the equations [7], [8] and [9] equals 0, the settling velocity for a spherical particle is given by:

$$v_s = \frac{2(\rho_p - \rho_m)gR^2}{9\eta} \quad \textbf{[10]}$$

where v_s is vertically oriented downwards or upwards depending on the mass density difference.

2.1.3 Surface tension and capillary action in a cylindrical well

A molecule in the bulk of a liquid benefits from cohesion forces with all the surrounding other molecules. This is also verified for surface molecules but fewer neighbors are available in this case resulting in an excess of energy for the surface molecules. This is the fundamental reason for which fluids adapt their surface in order to minimize their surface area (De Gennes, Brochard-Wyart, & Quere, 2003). The surface tension γ is defined as the Gibbs free energy per surface area for constant pressure and temperature (Gravesen, Branebjerg, & Jensen, 1993):

$$\delta W = \gamma \cdot dA \;\Rightarrow \gamma = \left(\frac{dW}{dA}\right)_{p,T} \quad \textbf{[11]}$$

Qualitatively, if U is the energy of cohesion between the fluid molecules, a surface molecule will lose an amount of binding energy equal to $U/2$ because of the missing neighbors. A rough estimation of γ is equal to the ratio of the half of energy of cohesion for a single molecule and the molecule area $\sim U/(2R^2)$

Surface tension has the units of N/m or equivalently J/m^2, and so it may be thought of as the external force needed to supply the work to extend a flat rectangular surface (W, L) of in the L direction while keeping the other length constant of a quantity ΔL. The work is then $\Delta G = F\Delta L$, and it is equal to the amount of energy contained in the new surface area $(W\Delta L)$ which, from Eqn. [11], is equal to $\Delta G = \gamma W \Delta L$. This gives:

$$\frac{F}{W} = \frac{\Delta G}{W\Delta L} = \gamma \quad \textbf{[12]}$$

For the case of a curved interface between two immiscible fluids such as water and air there is a difference of pressure due to the surface tension and it is given by the Young-Laplace pressure:

$$\Delta p = \gamma\left(\frac{1}{R_1}+\frac{1}{R_2}\right) = \left(\frac{2\gamma}{R}\right)_{R_1=R_2=R} \quad \textbf{[13]}$$

where R_1 and R_2 are the radii of curvature of the interface and are equal to R for a spherical interface created in a cylinder with section radius *a* as shown in Figure 3.

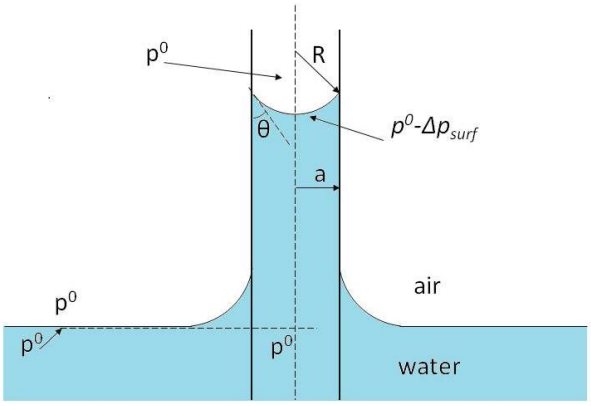

Figure 3. Capillary rise in a cylindrical duct.

The convention we use here is that the pressure is highest in the phase where the centers of the curved surfaces are placed. If the cohesive forces within the liquid are smaller than the adhesive force between the liquid and solid, the liquid is said to wet the surface and the surface of the liquid near the edge of the tube will be curved. The center of the curved spherical surface will be situated in the air. The contact angle θ, which depends on the fluids' and solids' properties with which they are in contact, is the dependent variable of the radius of the sphere expression:

$$R = \frac{a}{\cos\theta} \quad \textbf{[14]}$$

By substituting Eqn. [14] in to Eqn. [13], the difference between the air pressure and the pressure drop across the interface in these conditions can be written as (Bruus, 2007):

$$p_{liq}(H) = p_0 - \Delta p_{surf} = p_0 - \frac{2\gamma\cos\theta}{a} \quad \textbf{[15]}$$

where H is the capillarity rise height. The air pressure p_0 can also be calculated as the sum of the liquid pressure at the height H and the hydrostatic pressure $\rho g H$:

$$p_0 = p_{liq}(H) + \rho g H \quad \textbf{[16]}$$

By substituting Eqn. [16] in Eqn. [15], we get the height reached by a fluid as a result of the capillarity action:

$$H = \frac{2\gamma}{\rho g a} cos\,\theta \quad \textbf{[17]}$$

Starting from Eqn. [17] we can accurately measure the surface tension γ between two immiscible fluid phases since all the physical quantities in Eqn. [17] are known, except for H and θ which can be measured optically.

In the specific case of the microwell array, we need to fill by capillarity a number of microwells with radius from 35 to 50μm and height ranging from 50 to 300μm depending on the specific chip prototype. For these diameters, quite significant rise heights are reached (~ cm) so they are easily filled and a meniscus (curved water/air interface) is obtained at the microwell opening.

Eqn. [17] can be used as a design rule for the meniscus strength. Depending on the radius and the used materials (contact angle) higher or lower pressure across the interface is imposed which means stronger or weaker meniscus.

2.2 Dielectric properties of materials

2.2.1 Interfacial polarization

Every dielectric material can be described by means of its permittivity and conductivity. The latter describes the ability of charges to move freely in the material. A good conductor under the effect of an electric field will establish an equal surface charge density canceling out the electric field in its bulk. Permittivity instead, is defined as the ability of a material to store charges or, in a macroscopic scale, to polarize. A material with high permittivity reduces the electric field in its bulk by creating another internal electric field due to the polarization mechanisms which depend on the frequency of the external electric field. In Figure 4 we evidence the five different polarization mechanisms that can take place when a dielectric material is under the effect of an electric field: electronic, atomic, orientational (δ), interfacial (β), and counterions polarizations (α). Each of them is characterized by a relaxation frequency defined as the frequency for which the period of time the dipole has to 'relax' in and follow the field is equal to the period of the electric field (Morgan & Green, 2002). Below this frequency, maximum polarization and energy storage occurs; at this frequency the dissipation energy is maximized and above it (at very high frequencies) no polarization takes place. The frequency-dependent expression for the complex permittivity is:

$$\tilde{\varepsilon} = \varepsilon^{'} - i\varepsilon^{''} \quad \textbf{[18]}$$

where $\varepsilon' = \varepsilon_0\varepsilon_r$ is the relative permittivity of the material and $\varepsilon^{''}$ is the out-of-phase loss factor $\varepsilon" = {}^{\sigma}/_{\omega}$.

The frequency-dependent response of a medium to the wave propagation due to the lag between the changes in polarization and in the electric field is also known as the material's dispersion. When different materials are interfaced e.g. cells in suspension, the mobile and surface charges accumulate at the interface and give rise to the interfacial polarization that gives rise to the Maxwell-Wagner effect or the β-dispersion. All these terms refer to the complex permittivity frequency function of the mixture composed from the particles and the medium.

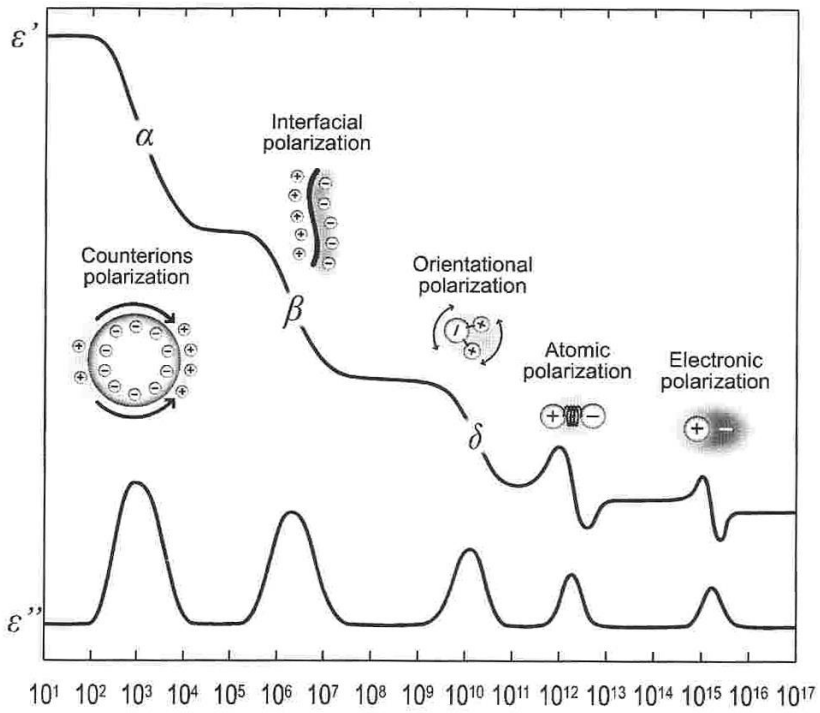

Figure 4. Dielectric materials polarization mechanisms contribute to the frequency-dependent complex permittivity. The frequency range of our interest 10^5 10^7Hz is related to the interfacial (β) dispersion which take place at lower frequencies (Picture taken from (Gawad S. , 2004)).

Both dielectrophoretic force phenomenon and impedance change that take place when an electric field is applied to particles suspended in an electrolyte, are related to the change of the induced dipole moment associated with the membrane charge redistribution which corresponds to the interfacial polarization. The associated β-dispersion is situated between hundreds of kHz and units of MHz depending on the cells and the medium conductivity as it is shown in Figure 4. Besides the fact that information about the membrane integrity and cell shape influence the β-dispersion, the reasons for using this dispersion type are related to the fact that at low frequencies electrochemical degradation of electrodes occurs. Most of chip designs for manipulating particles via electric field forces use frequencies above the *10kHz* range. Large planar electrodes are also used to reduce the current density and increase electrode robustness with respect to electrochemical degradation (Mernier, Duqi, & Renaud, 2012). There is no limit at high frequencies from this point of view so the frequency where the cell information is highest can be chosen.

2.2.2 Force and torque on an infinitesimal dipole

The following approach formulates the expression for the force exerted on a dielectric material by a non-uniform electrostatic field (Jones, 1995). In Figure 5 a dipole consisting of two equal and opposite charges $+q$ and $-q$ located at a distance $\vec{d}$ from each other and the dipole is subjected to an electrostatic non-uniform field $\vec{E}$. Due to the field non-uniformity the charges experience different values of $\vec{E}$ and a net force will be exerted on the dipole:

$$\vec{F} = q\vec{E}\left(\vec{r} + \vec{d}\right) - q\vec{E}(\vec{r}) \quad \textbf{[19]}$$

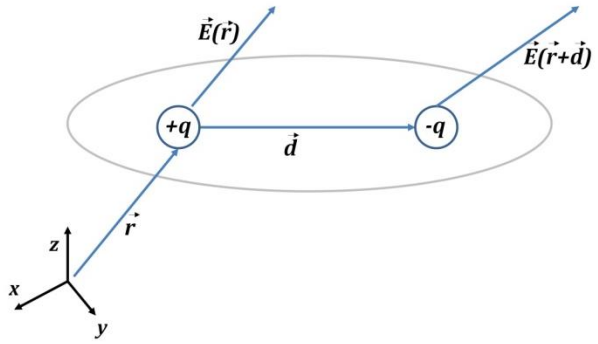

Figure 5. Force exerted upon an infinitesimal dipole by an electric field

When the distance between the charges is small with respect to the field non-uniformity we can expand the first term on the right of the above expression using a vector Taylor series neglecting the series terms from second order and on:

$$\vec{F} = q(\vec{E}(\vec{r}) + \vec{d}\nabla\vec{E}(\vec{r})) - q\vec{E}(\vec{r}) = q\vec{d}\nabla\vec{E}(\vec{r}) \quad \textbf{[20]}$$

Being $\vec{p} = q\vec{d}$ the dipole moment we obtain the expression of the force on an infinitesimal dipole:

$$\vec{F} = \vec{p}\nabla\vec{E}(\vec{r}) \quad \textbf{[21]}$$

Eqn. [21] reveals the non-uniformity of the field condition for having a net force on the dipole.

Similarly with basic vectorial operations, the torque can be calculated referring to the net force which acts at the center of the dipole.

$$\vec{T} = \vec{p} \times \vec{E} \qquad \textbf{[22]}$$

The only requirement for the torque to exist is that the moment and the field are not parallel. It depends on the electric field not on its gradient and this permit to have a net torque even in presence of uniform electric fields.

2.3 Dielectrophoretic forces on spherical particles

2.3.1 Polarization of an homogeneous sphere

The homogeneous sphere is a simple model which approximates for instance polystyrene particles that are widely used in lab-on-chip devices, e.g. for calibration purposes, since their behavior resembles that of cells for certain frequencies.

Referring to (Jones, 1995) the derivation of the dipole moment of a homogeneous sphere that is induced from the electric field can be expressed as:

$$\vec{p} = 4\pi\varepsilon_m \left(\frac{\tilde{\varepsilon}_p - \tilde{\varepsilon}_m}{\tilde{\varepsilon}_p + 2\tilde{\varepsilon}_m} \right) \vec{E} \qquad \textbf{[23]}$$

where $\vec{E}$ is the uniform electric field, the subscripts *p* and *m* stand for particle and medium; the complex permittivity is defined in section 2.2.1. The expression between brackets is named the Clausius-Mossotti factor and describes the frequency dependence of the dipole polarization.

$$f_{cm}(\omega) = \frac{\tilde{\varepsilon}_p - \tilde{\varepsilon}_m}{\tilde{\varepsilon}_p + 2\tilde{\varepsilon}_m} \quad \textbf{[24]}$$

The lower and upper limits of its real part are -0.5 and +1 respectively, and its imaginary part is bounded between -0.75 and +0.75. The Clausius-Mossotti factor describes the relaxation with a time constant as shown in the illustrative example of Figure 6:

$$\tau_{MW} = \frac{\varepsilon_p + 2\varepsilon_m}{\sigma_p + 2\sigma_m} \quad \textbf{[25]}$$

where MW stands for the Maxwell-Wagner dispersion. A generic case of the variation of the Clausius-Mossotti factor over the frequency spectrum is shown in Figure 6 where the low and high frequency analytical expressions of f_{cm} are also indicated.

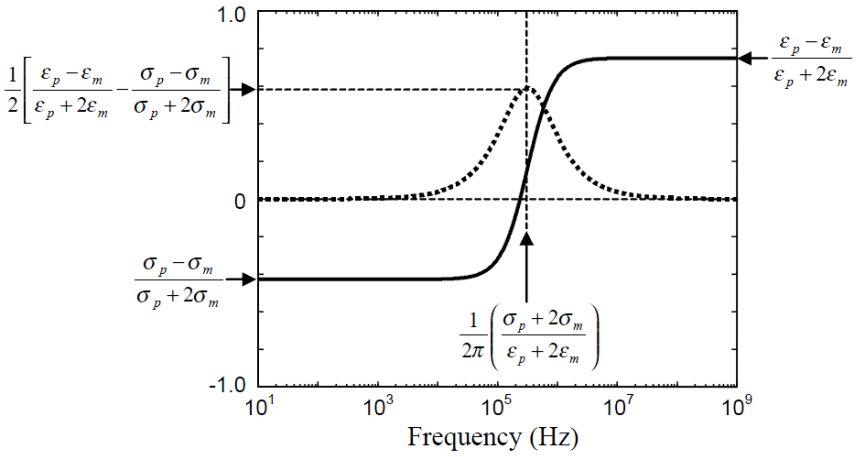

Figure 6. Real(solid line) and imaginary (dotted line) part of the Clausius-Mossotti over frequency for an homogeneous particle((Morgan & Green, 2002)).

The low frequency limit of the real part is dominated by the conductivity of the particle and the medium while the high frequency value depends only on their permittivity. This model is also a valid approximation for AC electric fields under the assumption that field is uniform across the particle. The expression for multipolar moments can be found in (Jones, 1995). The expression of the force exerted on a homogeneous sphere is given in the next section.

2.3.2 Force on a homogeneous particle

Electric fields induce charge displacements and the capability of following the field by charge redistribution (polarizability) decreases with frequency. It was mentioned above that the speed of charge accumulation mechanism is exceeded from the field frequency in certain frequency values named relaxation frequencies.

Dielectrophoresis is generated from the action of a non homogeneous electric field on the cell dipole induced by the field itself. Dielectrophoresis strongly depends on the polarization mechanisms. If we suppose that the field is quasi-uniform within the particle (homogenous field approximation) the time-averaged DEP force on a spherical particle (similarly to the force on the infinitesimal dipole of Eqn. 17) is defined as (Morgan & Green, 2002), (Jones, 1995):

$$\langle \vec{F}_{DEP} \rangle = \pi \varepsilon_m R^3 \Re(\tilde{f}_{CM}) \nabla \left| \vec{E} \right|^2 \quad \textbf{[26]}$$

In this approximation which is valid in the whole extent of this study, $\langle \cdot \rangle$ represents a time-averaged operation. Referring to the real part of the CM factor in Figure 9 with σ=0.1 S/m. The expression [26] shows that the force is proportional to the particle volume, to the gradient of the squared electric field intensity and to the real part of the CM factor. Furthermore, its sign depends on the sign of the CM factor. The CM factor is positive when the particle is more polarizable than the surrounding fluid and positive dielectrophoresis (pDEP) takes place i.e. a net force pushes the particles toward the high electric field domains. Opposed to pDEP, negative dielectrophoresis (nDEP) pushes the particles toward the regions characterized by a minimum electric field norm.

From a practical point of view, a sinusoidal voltage is applied to the electrodes in order to generate a non uniform electric field within the domain where particles flow. The DEP force expression in [26] can also be related to the root mean square of the electrical field by simply multiplying this expression by 0.5. This factor derives from the root mean square (RMS) value of the applied potential which is $V_0/\sqrt{2}$ being V_0 the amplitude of the applied voltage. Such a signal with frequency ω can be applied by polarizing the electrodes

with a sinusoidal signal. The electric field root mean square (from which the nDEP force modulus depends) is controlled by shifting the phase difference of the sinusoids. In this case the RMS value of the signal obtained as their difference is (Bocchi, et al., 2009):

$$V_{RMS} = V_0 \sqrt{2\pi/\omega \int_0^{2\pi/\omega} [\cos(\omega t + \varphi_1) + \cos(\omega t + \varphi_2)]^2} = V_0 \cdot G(\phi_D) \qquad [27]$$

where $G(\phi_D)$ depends on the phase difference and is maximized for $\phi_D = \pi$ following the trend visualized in Figure 7.

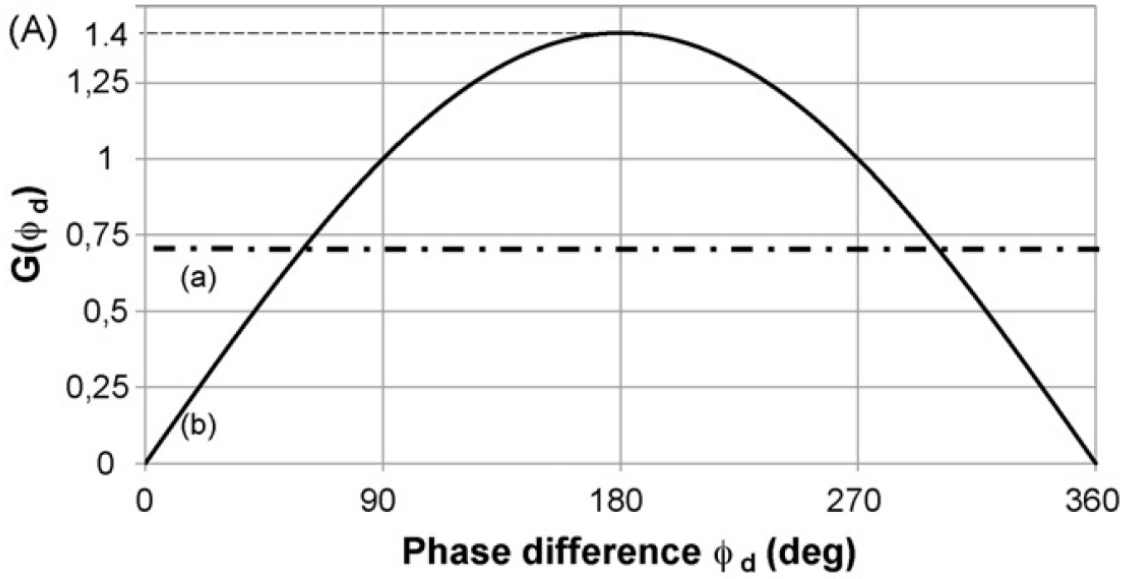

Figure 7. The effective RMS electric field between two electrodes is a function of the phase difference between signals. Curve (a) shows the G value when one of the electrodes is grounded. (b) The case of two electrodes polarized by the same signals with a phase difference ranging from 0°-360°.

Similarly, DEP forces are generated also when one of the electrodes is grounded (the electric field is non-uniform in this case as well); the RMS value in this case is shown with a dotted line in Figure 7 (equal to $1/\sqrt{2}$). Both combinations of signals are used in this study to generate DEP forces within the designed microstructures for cell manipulations.

2.4 Dielectric spectroscopy

2.4.1 The single shell model for biological particles

The need of the single shell model for spherical particles in suspension derives from a number of physical cases for which the homogeneous model is not good anymore. For instance, dielectric microparticles sometimes are coated with conducting materials to reduce static electrification. Another example is given by the internal interfaces of the biological cells due to the nucleus and the insulating lipid membrane, which have to be taken into account for a more accurate modeling. The common approach is to consider cells as a composition of concentric shells. By iterative analytical calculations an expression for the equivalent dielectric properties of a homogeneous sphere can be found.

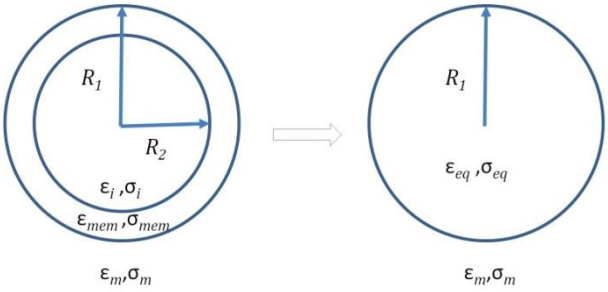

Figure 8. Spherical single shell model and its equivalent in terms of dielectric properties. Adapted from (Jones, 1995).

In our study, the single-shell model is used for numerical simulations and the resulting Clausius-Mossotti factor is:

$$\tilde{f}_{CM} = \frac{\tilde{\varepsilon}_{eq} - \tilde{\varepsilon}_m}{\tilde{\varepsilon}_{eq} + 2\tilde{\varepsilon}_m} \quad \textbf{[28]}$$

where $\tilde{\varepsilon}_{eq}$ is the equivalent particle complex permittivity defined as:

$$\tilde{\varepsilon}_{eq} = \tilde{\varepsilon}_{mem} \frac{\gamma^3 + 2\left(\frac{\tilde{\varepsilon}_i - \tilde{\varepsilon}_{mem}}{\tilde{\varepsilon}_i + 2\tilde{\varepsilon}_{mem}}\right)}{\gamma^3 - \left(\frac{\tilde{\varepsilon}_i - \tilde{\varepsilon}_{mem}}{\tilde{\varepsilon}_i + 2\tilde{\varepsilon}_{mem}}\right)} \quad \textbf{[29]}$$

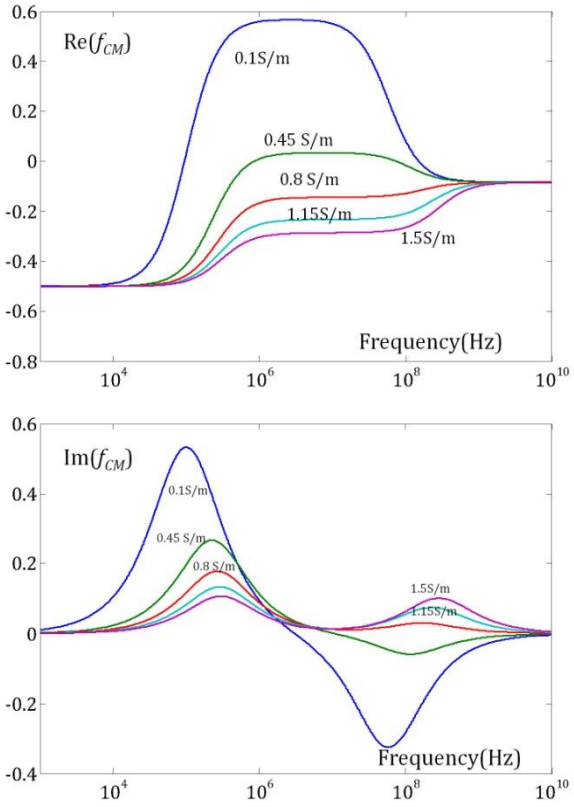

Figure 9. Real and imaginary part of the Clausius-Mossotti factor for a single shell modeled particle with suspended in a medium with parametric conductivity (σ_m=0.1-1.5S/m, ε_m=78). Particle's properties: σ_{mem}=1e-8S/m, ε_{mem}=2.5, σ_i=0.5S/m, ε_i=60.

In Eqn. [29] $\gamma = R1/R2$, and the other parameters are defined in Figure 8. Figure 9 shows real (top) and imaginary (bottom) plots for the Claussius-Mossotti factor for a single-shell model where two dispersions are visible corresponding to the medium-membrane and medium-cytosol interface respectively. The conductivity of the medium is the parameter indicated in each curve whereas the values of the other dielectric properties are indicated in the figure's caption.

The mathematical model can be developed to N number of shells which give rise to $N + 1$ dispersions. As mentioned above in this study a single shell model was used for the numerical simulations.

Impedance measurements, likewise dielectrophoretic forces, are based on the impedance change due to the induced dipole's presence. The particle perturbs the applied electric field becoming, in this way, detectable by measuring the current.

The impedance of the measurement site which consists of a couple of electrodes immersed in an electrolyte is given by:

$$Z = \frac{\kappa}{i\omega\tilde{\varepsilon}} \quad \textbf{[30]}$$

where κ is a geometric cell constant related to the measurement volume geometry and is defined as the ratio between the resistance and the resistivity of the filling medium or as the ratio between the permittivity of the medium and the capacitance:

$$\kappa = \frac{R}{\rho}, \text{and since } RC = \frac{\varepsilon_0\varepsilon_r}{\sigma} \Rightarrow \kappa = \frac{\varepsilon_0\varepsilon_r}{C} \quad \textbf{[31]}$$

The variation of the suspension's complex permittivity can be estimated by measuring the impedance. The suspension's limit case is the single-particle between the electrodes. The mixture permittivity expression for a diluted cell suspension was derived by Maxwell:

$$\tilde{\varepsilon}_{mix} = \tilde{\varepsilon}_m \frac{1 + 2\varphi\tilde{f}_{CM}}{1 - \varphi\tilde{f}_{CM}} \approx \tilde{\varepsilon}_m(1 + 3\varphi\tilde{f}_{CM}) \quad \textbf{[32]}$$

The volume fraction φ is the ratio between the particle and the measurement site volume and the formula is valid only for $\varphi \ll 1$. If this is not the case, expressions derived for high particle concentrations (Hanai, Asami, & Koizumi, 1979) are to be used. Eqn. [32] highlights the fact that the electrolyte complex permittivity is modulated from the particle; the expression between brackets depending on the Clausius-Mossotti factor. The relative impedance variation is given by:

$$\frac{\Delta Z}{Z_o} = \frac{Z - Z_0}{Z_o} = -\left(1 - \frac{\tilde{\varepsilon}_m}{\tilde{\varepsilon}_{mix}}\right) = -\left(1 - \frac{1}{1 + 3\varphi\tilde{f}_{CM}}\right) \approx -3\varphi\tilde{f}_{CM}, \varphi \ll 1 \qquad \textbf{[33]}$$

where Z_0 is the impedance of the medium alone. The above expression is related to the relative impedance change due to the presence of a cell.

Impedance changes due to the presence of a particle and dielectrophoretic forces are both due to the induced dipoles. In the case of the impedance measurement, the induced dipole is detected by evaluating its effect on the primary applied voltage.

In dielectrophoresis, the induced dipole experiences a net force in the inhomogeneous field which causes its movement.

Electrical equivalent circuit discrete models involving only a few capacitors and resistors can give very good approximations to the Maxwell–Garnett mixture equation (Eqn. [32]) (Morgan & Green, 2002). In (Foster & Schwan, 1989) an equivalent circuit is shown which is valid for a cell in suspension between two parallel facing electrodes. Let us consider only the central part of the circuit which represents the cell's and the electrolyte's impedance. In this circuit, the cell is represented by a capacitor C_{mem} and a resistor R_i in series. The electrolyte is represented from C_m and R_m in parallel. The cell's membrane resistance and cytosol capacitance are neglected in this simplified model.

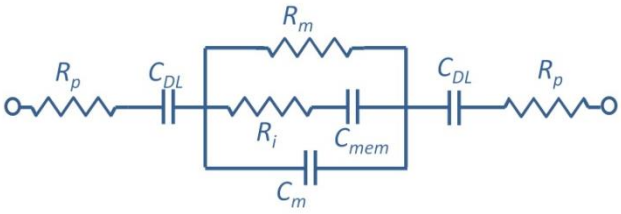

Figure 10. Schwan's electric equivalent circuit for single cell in suspension between two electrodes. The cell is modeled as a resistance R_i and a capacitance C_{mem} in series.

The cell membrane acts as a capacitor at low frequencies (up to 1MHz). As the frequency increases (>5MHz), the membrane capacitor is shorted and cell internal properties are represented by the resistor.

The values of the parameters for the equivalent circuit proposed by (Schwan, 1957) shown in Figure 9 are given by:

$$\begin{cases} \mathrm{R}_m = \dfrac{1}{\sigma_m \left(1 - \dfrac{3\varphi}{2}\right)\kappa} \\ C_{mem} = \dfrac{9\varphi R C_{mem,0}}{4}\kappa \\ R_i = \dfrac{4\left(\dfrac{1}{2\sigma_m} + \dfrac{1}{\sigma_i}\right)}{9\varphi\kappa} \\ C_m = \varepsilon_\infty \kappa \end{cases} \quad \textbf{[34]}$$

with the membrane capacitance per unit area $C_{mem,0} = \varepsilon_{mem}/d$ and the permittivity at infinite frequency being:

$$\varepsilon_\infty = \varepsilon_m \frac{2\varepsilon_m + \varepsilon_i - 2\varphi(\varepsilon_m - \varepsilon_i)}{2\varepsilon_m + \varepsilon_i + \varphi(\varepsilon_m - \varepsilon_i)} \quad \textbf{[35]}$$

The Schwan's circuit model has been used (Gawad, Schild, & Renaud, 2001), (Sun & Morgan, 2010) to interpret single cell impedance measurements providing good agreement with experiments.

Besides the resistance of the medium R_m a parasitic resistance R_p is also present in the circuit. This resistance results from the connecting cables and mainly the metal electrodes resistance. Furthermore when a metal electrode immersed in an electrolyte the surface charge is balanced from the accumulation of charged particles in the electrolyte in order to maintain charge neutrality. The accumulation of ions give rise to an electrical double layer and this phenomenon can is represented by a capacitance named C_{DL}. This capacitance influences the measured impedance at frequencies below some kHz. At the frequency ranges of our interest ($\sim$ 100kHz - 15MHz) the double layer effect can be neglected and will not be covered in this dissertation. The measured impedance at the mentioned range of frequency is proportional to the electrolyte and cell impedance. A treatment of the double layer effect can be found in (Morgan & Green, 2002), and in (Gawad S. , 2004).

2.5 Lock-in amplifying scheme

Lock-in amplifiers use a technique known as phase-sensitive detection for singling out the signal component at a specific reference frequency and phase. The lock-in amplifier has been widely used in applications in which a small current at a known frequency is the signal to be measured and noise at the unused frequency spectrum has to be suppressed. In biological field its applications range from intracellular and transmembrane measurements to cell suspensions, single cells and tissues.

In the case of a monochromatic sine wave the excitation signal is modulated by the channel impedance and the signal at the input of the demodulator unit can be expressed as:

$$V_o(\omega_0) = V_0 \cdot \sin(\omega_0 t + \theta_0) \quad \textbf{[36]}$$

This signal flows through the device under test which modulates its amplitude. To recover the amplitude of the signal in-phase at the excitation frequency we should then multiply V_o by a signal with the same frequency. Let us suppose that its phase is θ_1.

$$\begin{aligned} V_{o1}(\omega, \theta, t) &= V_0 \cdot V_1 \cdot \sin(\omega_0 t + \theta_0) \cdot \sin(\omega_0 t + \theta_1) \\ &= 0.5 \cdot V_0 \cdot V_1 \cdot \cos(\theta_1 - \theta_0) + 0.5 \cdot \sin(2 \cdot \omega_1 t + \theta_0 + \theta_1) \end{aligned} \quad \textbf{[37]}$$

By low pass filtering the component at $2\omega_1$ we get a DC voltage dependent from the amplitude of V_0 which is the unknown value we want to determine. Similarly we multiply V_o with a signal of the same amplitude $V_1$with a phase difference of π/2 and after filtering we get for each case:

$$V_{o1}(\theta) = 0.5 \cdot V_0 \cdot V_1 \cdot \sin(\theta_1 - \theta_0), \quad V_{o2}(\theta) = 0.5 \cdot V_0 \cdot V_1 \cdot \sin(\theta_2 - \theta_1) \quad \textbf{[38]}$$

At this point it is sufficient to use polar coordinates and obtain the amplitude and the phase of the modulating signal:

$$|V_0| = \frac{2}{V_1} \cdot \sqrt{(V_{01})^2 + (V_{02})^2}, \qquad \theta = tan^{-1} \frac{V_{02}}{V_{01}} \quad \textbf{[39]}$$

3 Cell delivery through a microdispenser using “open microwell” arrays

Summary: In this chapter a method for aligning with micrometric precision a dispenser able to deliver picolitre droplets of fluid possibly containing cells and particles into an array of microwells fabricated on a flexible large area substrate is presented. Initially the system is described and the causes of the alignment problem are highlighted. Then the proposed analytical method on which the three dimensional reconstruction of the device is based is presented and the reasons for choosing this method are outlined. The implemented calibration procedure is then described. In the end, testing of the system performance in terms of delivery accuracy and device calibration speedup are presented.

3.1 The *direct* “open microwell” concept

The initial structure proposed by our group (Bocchi, et al., 2009) aimed to fulfill a number of requirements for lab-on-chip solutions. The first design requirement is the handling and analysis of single cells with high parallelism. It is dictated by several drug discovery applications necessity to monitor in parallel the cell responses to drugs and other cells’ presence. Another desired feature of the device was the possibility to recover cells after analysis for further culturing and examination of selective monoclonal cell lines.

The core element of the design is the open microwell defined as a microwell whose both bottom and top ends are open. Its working principle is shown in Figure 11.

To fulfill the single cell isolation requirement, a large array of active microwells was designed. The working principle of this device described is the levitating of cells within the microwell *via* nDEP forces for massive parallel analysis. Cells are introduced into the wells by a piezoelectric micro droplet dispenser from the top opened side of the microwells (Figure 11.i).

The microwells feature also the presence of three annular electrodes which are patterned by drilling holes through a flexible printed circuit board (PCB). Embedded metal layers allow the patterning of electrodes faced to the microwells walls and are responsible to

bring the electrical field within the microwells, so to generate dielectrophoretic forces necessary to trap particles in suspension.

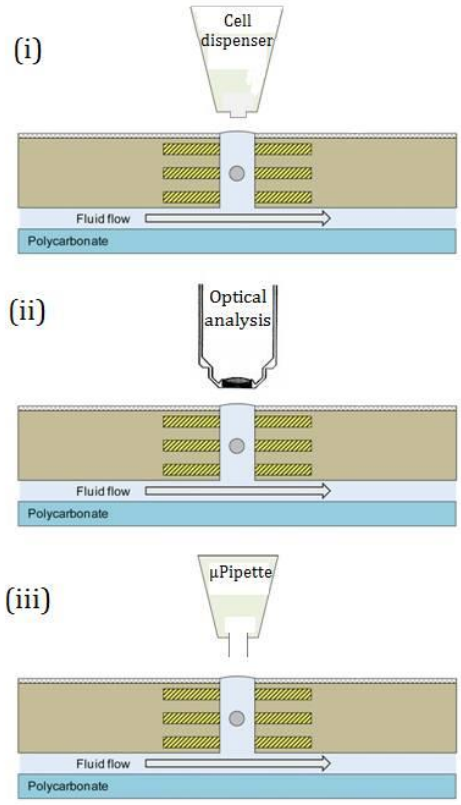

Figure 11. Working principle of the open microwell initial design. Delivery and recovery of samples are assigned to external tools (i) and (iii). Optical analysis of levitated cells after sample re-suspension (ii).

After one or more cells' introduction, the fluid suspension flowing in the bottom pool can be changed. The analysis of the cell response to each other presence or to drugs present in the fluid suspension can be then performed as in Figure 11.ii.

After analysis the content of every well can be recuperated *via* a micropipette (Figure 11.iii).

The device shown in Figure 12 represents an array of 32 x 48 microwells. Delivery and recovery of particles is done serially while the supernatant substitution is done in parallel from the bottom side. This permits a fast automated on-chip single cell centrifugation.

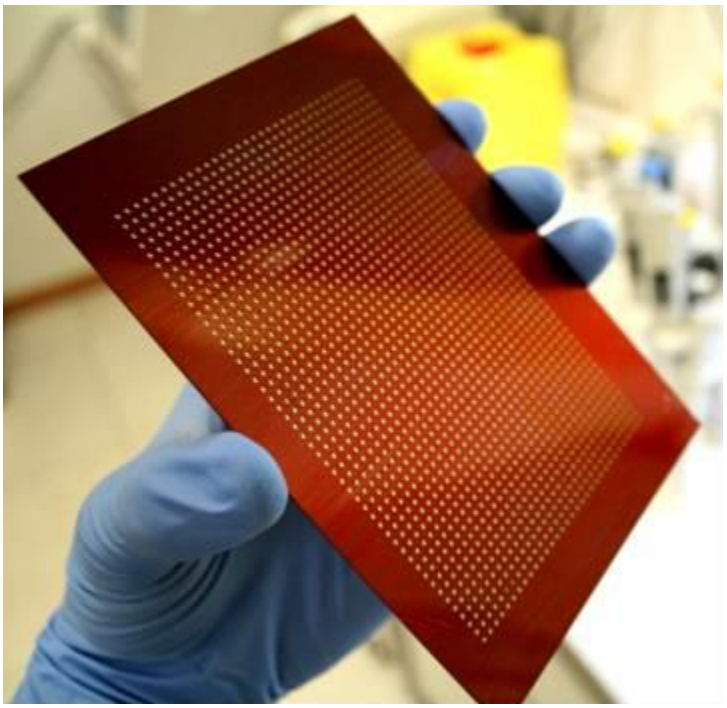

Figure 12. 32 rows x 48 columns microwell array fabricated in flexible PCB technology.

3.2 Cell isolation using an external piezoelectric microdispenser

3.2.1 System setup

The large area microwell array, whose buildup was presented above, includes 1536 microwells spread over an area of about 78 cm^2. The substrate contains active microwells opened at both ends. Embedded metal layers allow the patterning of electrodes faced to the microwells' walls.

Among the possible solutions for delivering particles to an array of microsites *via* low-volume liquid handling technologies, such as pneumatic, bubble jet and piezoelectric actuators (Koltay, Steger, Bohl, & Zengerle, 2004) (Allain, Askari, Stokes, & Vo-Dinh, 2001) (De Heij, Steinert, Sandmaier, & Zengerle, 2003) we opted for a commercial piezoelectric dispenser (Saunders, Gough, & Derby, 2008). It features low volume droplet ejection ranging from 0.2 to 1 nL.

Figure 13.b shows the delivery operation principle. A survey on the methods for the world-to-chip interfaces is presented in (Fredrickson & Fan, 2004).

The biosensor is mounted on a host board which provides fluidic and electric interfaces, and then fixed onto the microscope stage and a photograph of the system is shown in Figure 13.a. The bottom side of the array device is in contact with a pool into which a physiological solution is pumped in (Figure 13.b). As depicted in Figure 11 the buffer fills the microwells by capillarity action from the bottom, whereas the top side is in contact with air and can be accessed from external devices.

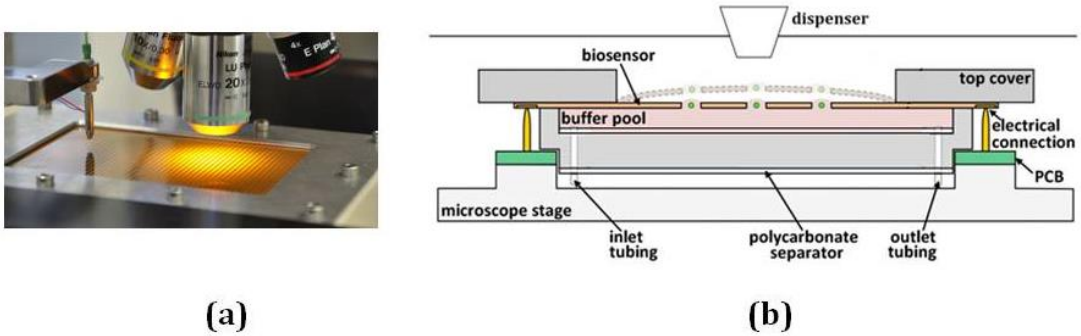

Figure 13. Cross section of the micro array and the package including fluidic and electrical connections.

The main objective is to analyze single-cell behavior and cell response to cell–cell contact events, with the aim to provide a device for functional cell sorting, i.e. the device should offer the possibility to extract the cells for further processes such as analysis in traditional microtiter plates or cell growth in cultures. As already mentioned, in this platform the cells' delivery is performed from the top by a piezoelectric dispenser. This is a challenging procedure because it requires a highly accurate alignment of the 50μm orifice of the dispenser with 100μm wells.

Furthermore, a native bending phenomenon affects the devices. This is due to a lack of symmetry with respect to the middle plane between the various polyimide and metal layers in the build-up. A supplementary deformation is also caused by the pressure field created by liquid in the buffer pool and by asymmetrical clamping between the top cover and the carrier caused by the spring-loaded connectors. In Figure 13.b the device bending due to the pressure field from the bottom pool is illustrated.

The bottleneck of the system particle delivery operation is represented from its serial nature, which has to be automated for such a large number of wells (1536). We developed

a method for fast calibration of a serial dispensing system for applications that requires volumes of fluid delivery as small as 0.2 nL to discrete micrometric target locations on a flexible array of microwells. The proposed technique reconstructs a three-dimensional model of the array surface from a reduced number of sampled surface points and uses this model to control the relative spatial positioning of the dispenser and the substrate. This software-based method overcomes the key issue relating to mechanical deformation of the microarray and the consequent difficulty of aligning each target microwell to external tools, a process that can lead to faulty vertical positioning and compromised delivery procedures.

The system interfaced to the lab-on-a-chip includes a fluorescence microscope (Nikon Eclipse 80i) equipped with a Nikon DS-2Mv digital camera and an XYZ motorized stage (Märzhäuser Wetzlar). To acquire each well's coordinates a focusing procedure is executed automatically. This autofocus procedure is based on the maximization of a focus index sampled at different positions on the Z axis. The index used is the standard deviation (*SD*) of the image histogram in grayscale, defined as the square root of the variance of the histogram (Allegro, Chanel, & Jacot, 1996). Since the focus plane corresponds to the lab-on-a-chip surface, which can be considered flat around the boundaries of a microwell, the focus index profile has a well defined global maximum, without local maxima as shown in Figure 14.

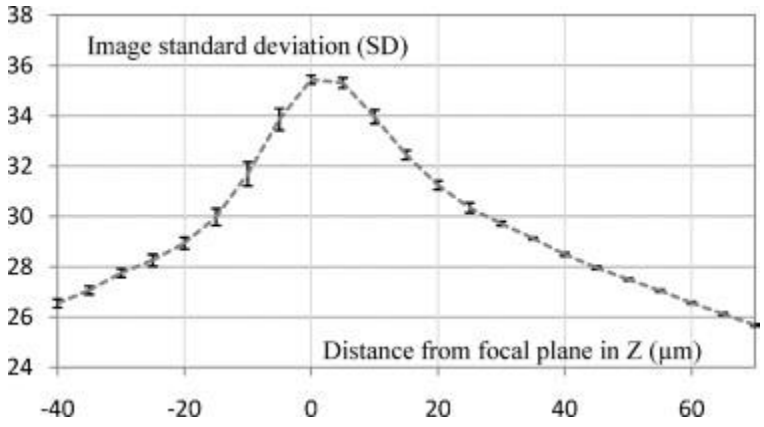

Figure 14. SD trend close to the focal plane of the microscope. Markers show the average SD value of several frames taken every 5 µm in both directions in Z from the focal plane.

The minimization of the *SD* gradient, obtained by comparing the last couple of *SD* values acquired, is used as the criterion for finding the best focus position. An inversion in the computed gradient causes the procedure to reverse the seek direction and to narrow the step down according to the Fibonacci sequence (Sun, Duthaler, & Nelson, 2004). This provides a fast initial approach to the *SD* maximum and fine detection, as the step size decreases rapidly.

3.2.2 Analytical modeling of the lab-on-a-chip surface deformation

The acquisition of the microwell coordinates following a well-by-well sampling would provide the actual position of all microwells with no interpolation error, but this approach would involve a high cost in terms of time. The implemented optimized procedure reconstructs the whole surface by sampling only a subset of n points in the array and calculates the remaining points using a spline-based interpolation method.

The surface is considered to be a single valued function of two variables (2-D), $f: R^2 \rightarrow R$ where the interpolation nodes (x_i,y_i), at which the value of the function is known belong to a regular grid of microwells. The data sites depict certain points on a map, while a data value $f_i=f(x_i,y_i)$ indicates the height at point (x_i,y_i).

Because the lab-on-a-chip is based on a flexible plate, which is generally characterized by smooth deformations without first order discontinuities, we chose to make use of the thin-plate spline (TPS) method as it is usually adopted to physically model smooth bending of thin metal sheets that are forced to pass through known data points (Buhmann, 2000).

Using radial basis functions (RBF), we created a model of the surface by reconstructing the unknown function $s^*(x,y)$ from known values f_i sampled at nodes (x_i,y_i). An RBF is a real-valued function whose value depends only on the distance from the origin. Although these functions are bivariate, they reduce to a scalar function of the Euclidean norm of their vector argument $|\boldsymbol{z}| = |(x - x_i), (y - y_i)|$.

The approximation is based on a linear combination of translates φ of a single RBF

$$s^*(x,y) = \sum_{i=1}^{n} \lambda_i^* \varphi\left(||x - x_i, y - y_i||\right) + p^*(x,y) \qquad \textbf{[40]}$$

where p^* is a polynomial of degree at most one or is not present and $\|\cdot\|$ is the Euclidean norm. In the case of TPS φ can be formulated as:

$$\varphi(x,y) = \varphi(r) = r^2 \log r, \qquad r > 0, \qquad \phi(0) = 0, \qquad r = \sqrt{x^2 + y^2} \qquad \textbf{[41]}$$

The real coefficients λ_i $(i=1,\ldots,n)$ are determined by requiring that $f_i = s^*(x_i, y_i)$. The solvability of the system above is guaranteed if φ is positive definite in R^2. Conditionally positive definiteness can be assured by adding a polynomial $p^*(x,y)$ with a degree of order at most one. The additional degrees of freedom introduced by the polynomial are removed by obliging the coefficients λ_i to satisfy the additional conditions:

$$\sum_{i=1}^{n} \lambda_i^* \boldsymbol{z}_i = 0 \quad and \quad \sum_{i=1}^{n} \lambda_i^* = 0 \qquad \textbf{[42]}$$

These conditions ensure that s^* has square integrable second derivatives.

3.2.3 Implementation and experimental results

3.2.3.1 Determining the optimal spotting distance

The accuracy and reliability of the delivery procedure depends on the distance between the dispenser and the array. The distance was calibrated experimentally to ensure accurate delivery of beads to the microsites by keeping the deviation of the droplets from the vertical direction within a target spot size. Figure 15.b visualizes the superposition of 400 stroboscopic frames. The image is obtained by multiplying all the frames, and it defines the deflection diameter D and the flying distance H. The most important parameter we determine from this experiment is the deflection angle α_D, which can be calculated as:

$$\alpha_D = tan^{-1}\left(\frac{D}{H}\right) = 5.5° \quad \textbf{[43]}$$

Therefore, the upper limit for the delivery distance is constrained by the horizontal dispersion that depends from this angle. The delivery process will be more accurate as we get closer to the substrate. We set the maximum acceptable spot diameter to D=80 µm. From Eqn. [43] we obtain a maximum spotting distance of H=830 µm. The spotting distance is given by:

$$H = H_{mech} + H_{err} + H_{margin} \quad \textbf{[44]}$$

where H_{mech}=600 µm is given by the height of a protective end cap shielding the nozzle and H_{margin} is a safety margin set to 100 µm. We eventually obtained that the maximum positioning error needs to be lower than H_{err}=130 µm. This value was then used to determine the optimal number of points to be sampled when reconstructing the substrate surface from a subset of spotting points.

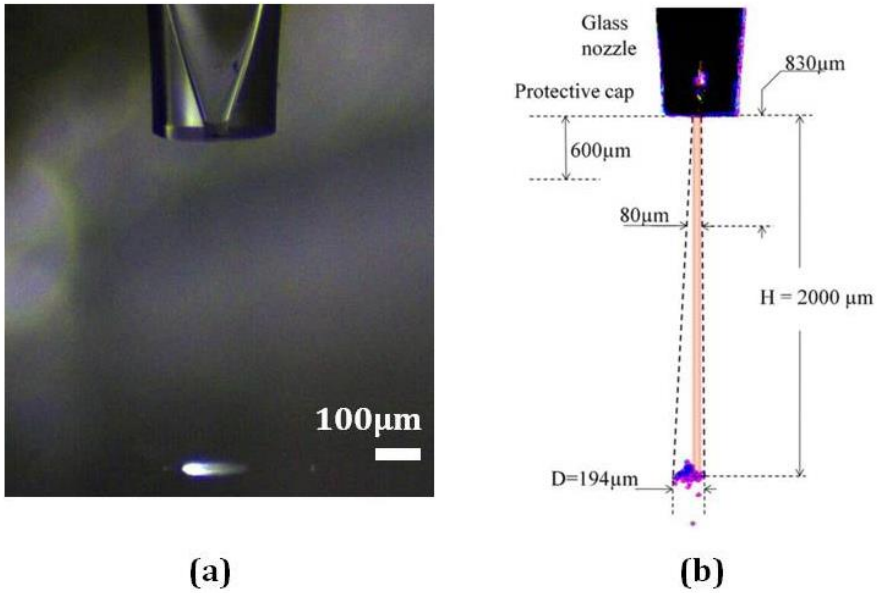

Figure 15. (a) Dispenser's glass tip over a microwell . (b) Superposition of 400 frames showing captured droplets in flight to determine the optimal spotting distance.

By reconstructing the array surface for determining the well's coordinates, we are able to adapt the dispenser's z-coordinate to the bended substrate, thus aiming to limit the droplet's deflection by maintaining a fixed delivery distance.

3.2.3.2 Positioning error assessment

The positioning error for each microwell was determined by comparing a 3D model of three devices with 36, 64 and 1536 microwells named respectively from now on SD36, SD64 and B1536. A Matlab illustration in Figure 16 shows the smooth surface obtained by applying the interpolation routine to SD36 starting from all 36 points.

The deformation caused by the pressure field created by the liquid in the buffer pool and by the clamping of the device into the host board is here reconstructed. To be noticed that the maximum deformation entity is encountered in the central area of the device. Selecting the correct physical law to describe the deformation would permit to minimize the number of needed points' coordinates for an reconstruction accuracy within the specified error limits.

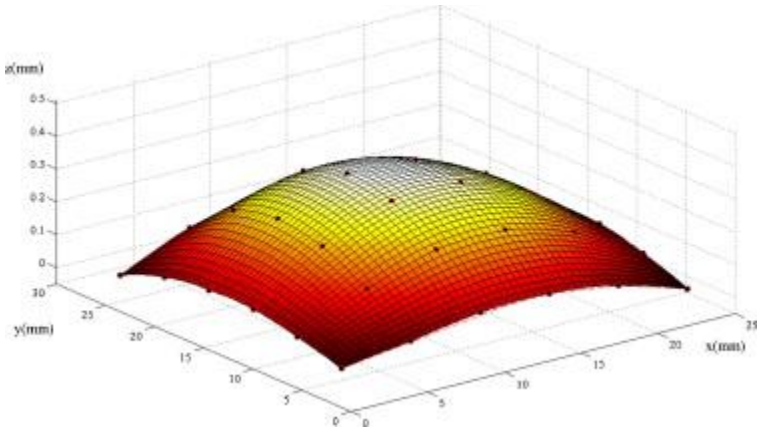

Figure 16. Surface bending of SD36, reconstructed by sampling the position of all 36 microwells.

To resume, the interpolation scheme used for calibrating the biosensor device can be resumed in two phases: (i) acquisition of a subset of well coordinates and (ii) prediction of the coordinates of the remaining wells in the array. While the execution time of the first phase mainly depends on the autofocus procedure, the interpolation procedure used to predict the displaced position of the other wells is cheap in terms of timing costs and is based on a software routine.

In Figure 17, the maps obtained from the model reconstructed from a subset of points are compared with those obtained from a full acquisition of all the wells' coordinates.

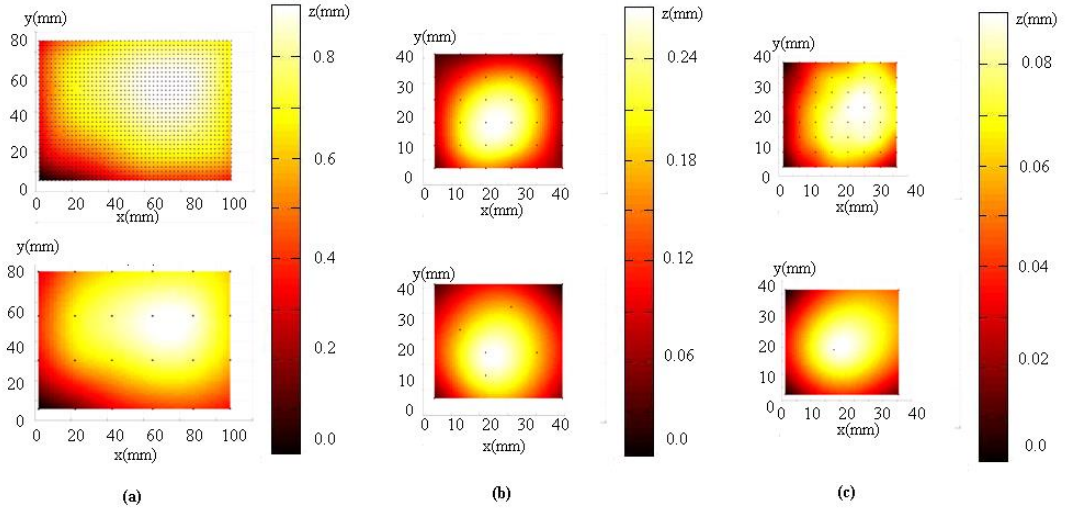

Figure 17. Full acquisition and optimal reconstruction for (a) B1536, (b) SD36, (c) SD64. The top row shows the result of the full acquisition, while optimal subset-based reconstructions are shown in the bottom maps for each biosensor, sampling (a) 24, (b) 9 and (c) 5 points.

The positioning error was calculated as the difference between the acquired coordinates and those found by interpolation. While this error is found to be negligible in the x and y direction for all biosensors, the error along the vertical direction depends closely on the number of points n defined in Eqn. 35. The number of samples n was chosen as the smallest subset of points that still guarantees an acceptable maximum error H_{err}, as defined in Eqn. 39.

When sampling a subset of points in the array, the quality of the interpolated surface, quantified in terms of error between the real and the predicted position of the microwells, depends on the number and the location of the sampled points. Since manual assembling causes random positioning of the array with respect to the carrier opening window, the location of sampling points has to be *a priori* determined. A tradeoff is expected between the acquisition time and the precision of the interpolation algorithm, which both increase with the number of sampled points.

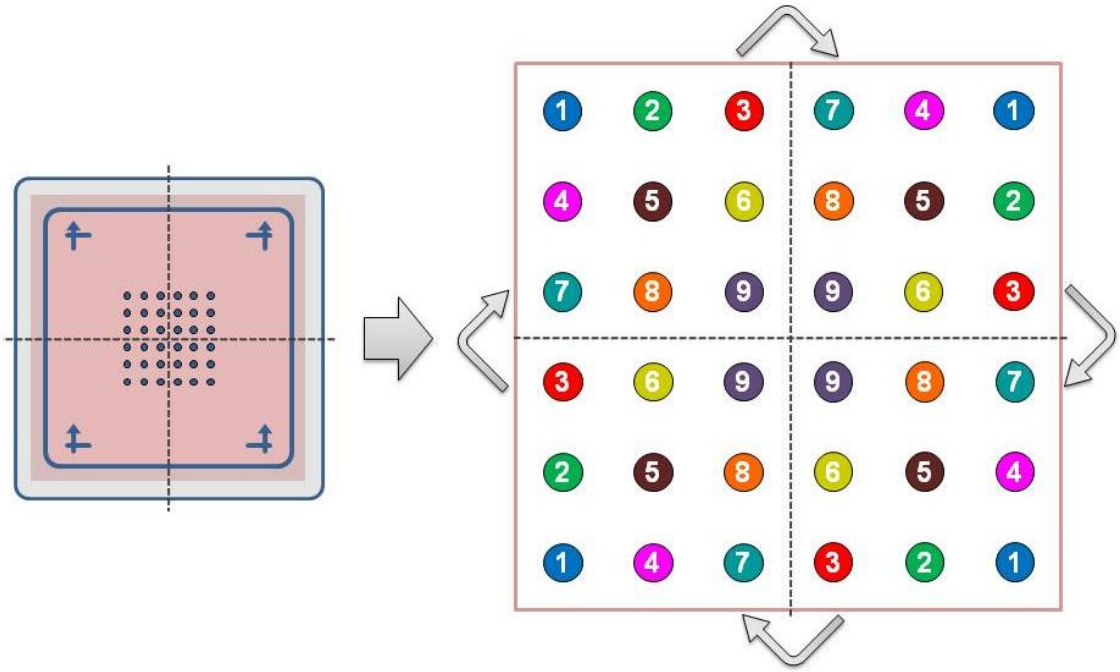

Figure 18. Strategy adopted for the selection of the points to be sampled.

To identify the best strategy about the selection of the points to be sampled, we referred to a real measurement on a 36-well array, with a microwells pitch of 4.5 mm. The coordinates of all 36 points in the array were acquired and used as actual data. Different interpolations were then built by changing the number and location of a subset of points, and the maximum error for each interpolation scheme was computed. Due to the randomness of the biosensor positioning, the strategy we followed was to consider a set of 5 starting points, four at the corners and one at the center of the array, and to subsequently add new points using a symmetric mapping. The number of sampling points is increased by four each time, following the rule illustrated in Figure 18. We divided the array into four symmetric areas and, after selecting a well on the first quarter, we imagine to rotate this area by 90 degrees and to overlap it to the second area to obtain the resulting point. This procedure was repeated for all the quarters.

Following the above approach, as an example, Figure 19 shows the absolute maximum positioning error along z measured for B1536 as a function of the number of points acquired. In this case the optimal value of n was 24 (defined as the value which permits to satisfy the error specifics while minimizing the acquisition time). To gain in precision

means to lose time while acquiring more sample points on the surface. The descending line represents the absolute maximum positioning error in Z for B1536 whose value, as described in section 3.2.3.3, affects the horizontal dispersion of the droplets, while the line graded on the right vertical axis shows the time necessary to acquire the point coordinates.

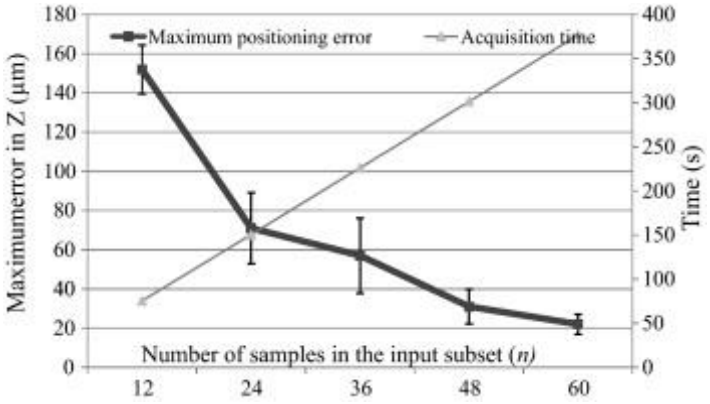

Figure 19. Absolute positioning error in the dispensing direction Z and acquisition time as a function of sample number of microwells for B1536. The average error values were obtained as a result of 20 different acquisitions of all microwell coordinates.

Table 1 quantifies the positioning error and maximum vertical bending for each device. The three devices (SD36, SD64 and B1536) differ not only in the total number of microwells but also in area and thickness. The maximum deformation entity depends on the area to thickness ratio which is different for each substrate. SD36 features the same pitch of a 384-well microtiter plate (4.5 mm) for a squared shape array of 36 wells and 240 µm thickness, while SD64 has a thickness of 550 µm and the distance between its wells is 2.25 mm. Both devices have an area of nearly 16 cm2.

Table 1.Positioning error post interpolation and the geometrical characteristics of each device. The number of samples was selected to achieve an acceptable error value while keeping sampling time as low as possible.

Device	LxW(mm)	Thickness(µm)	Pitch(mm)	Maximum deformation (µm)	# of samples (n)	Maximum error in z(µm)	Average error in z(µm)
SD36	40x 40	240	4.50	239	5	34.7	17.7
SD64	40x 40	550	2.25	91	5	16.0	6.0
B1536	120 x 80	240	2.25	813	24	74.0	28.1

The subset number of samples n for SD36 and SD64 to reconstruct the surface was obtained with the same method used for B1536.

3.2.3.3 Delivery accuracy assessment without surface reconstruction

The experimental validation of the relation between the spotting distance and the planar dispersion was determined by delivering droplets containing fluorescent microbeads in 1536 sites and then checking their position. The use of fluorescent beads allows the accurate measurement of the droplet position after the delivery process even after evaporation of the droplets which occurs in a few seconds. The droplets have a typical radius of about 30 μm while the radius of the microbeads is 7.5 μm. Given that the position of the bead within the droplet is random, this method introduces an additional tolerance of ±22.5 μm in determining the droplet position. This random error is added to the droplet positioning error. Hence, from a statistical point of view, by measuring the maximum distance of each particle from the target we are able to determine if each entire droplet results to be within the acceptable spotting region.

Instead of delivering droplets into the wells, we chose to place them at a known position close to the wells to ensure optimal detection conditions (Figure 20). The offset is sufficiently small to maintain both the well and the delivery target at approximately the same z-coordinate. An image detection routine was used to determine the number of beads and their location with respect to the center of the hole.

To experimentally determine the dependence of the droplet's deflection on the delivery distance, we examined a delivery process where no calibration was used i.e. no surface reconstruction which allows to adapt the distance between the nozzle and the substrate accordingly with the optically acquired surface. From Table 1 the maximum positioning error in Z is equal to the maximum deformation and is H_{err} = 813 μm. To allow a safety margin of H_{mech} + H_{margin} = 700 μm we obtain H = 1513 μm from Eqn. 39 and fixed the final distance to H = 1600 μm. Hence, the distance of the nozzle from the substrate varies from nearly 800 μm (highest microwells in the central area of the array) to 1600 μm (lowest microwells near the boundaries), depending on the z coordinate of every single

microwell. The total number of beads identified was 364, and their relative position with respect to their nominal location is shown in Figure 20.

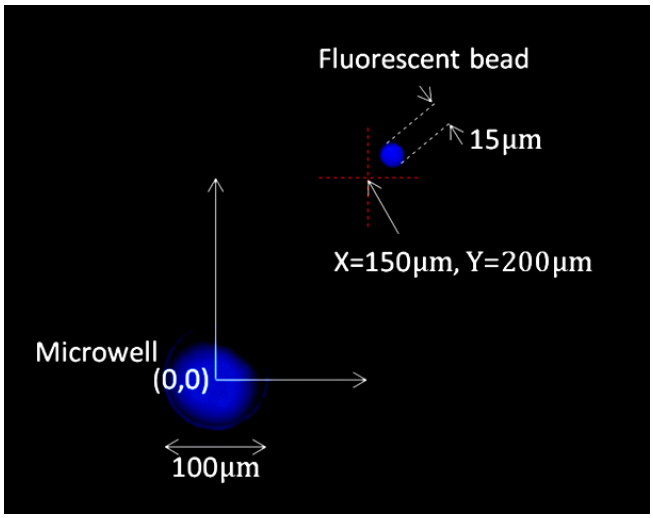

Figure 20. Detected fluorescent bead (15 µm diameter) close to the microwell (100 µm diameter).

As the delivery distance increases, the deflection from the vertical direction is affected in a linear trend with a coefficient of determination nearly 0.65. We also found that only 47% of the microbeads are located less than 50 µm away from the expected spotting coordinates, with a consequent spotting error in 53% of the cases.

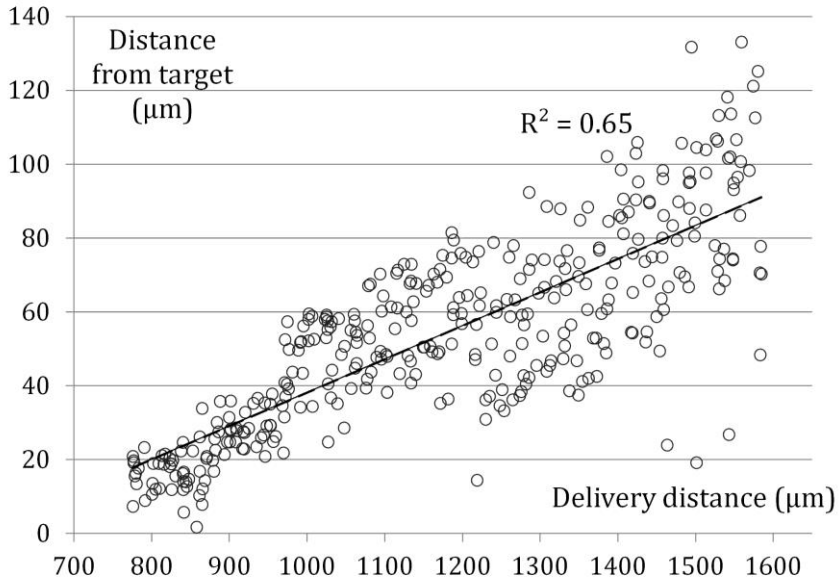

Figure 21. Delivery error with respect to the delivery distance in the absence of 3D modeling of the surface deformation.

3.2.3.4 Interpolation based delivery

The delivery procedure was then executed after 3D surface reconstruction. In this case, the nozzle distance is always adapted to the surface height to achieve the target distance of 800 µm. In Figure 22.a we report in an x-y map the same 364 points of Figure 21, and Figure 22.b shows data obtained from 855 beads after 3D reconstruction. The axis origin (0,0) coincides with the delivery target. Without 3D reconstruction the average position of the 364 detected beads is equal to μ_x=-0.3 µm, μ_y= -14.3 µm with respective standard deviations σ_x= 50.1 µm (65% hit ratio: beads within the well area/total number of beads), σ_y =82.9 µm (47% hit ratio). When 3D reconstruction is used, the data average is μ_x=-4.2 µm, μ_y= -2.7 µm and standard deviations σ_x= 16.7 µm (100% hit ratio), σ_y =18.8 µm (100% hit ratio).

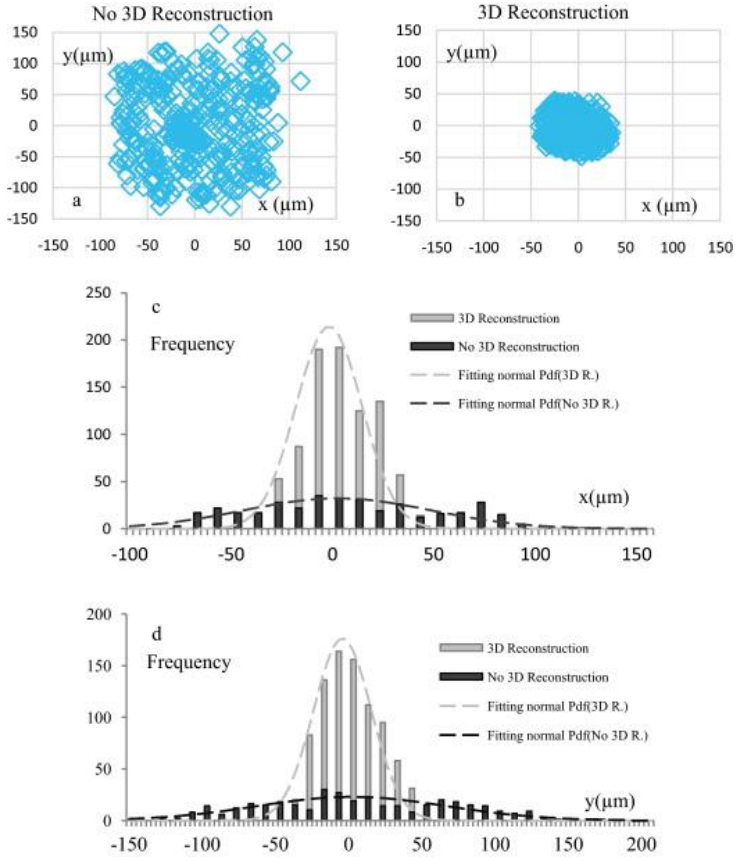

Figure 22 (a) and (b) Two sets of delivery data without and with 3D reconstruction, respectively. Each marker corresponds to a detected bead on the substrate. A histogram in the x-direction for both dispersions is shown in (c). A discrete normal probability density function (same average and standard deviation) is superimposed to underline similarities between the beads delivery process and a Gaussian

distribution. (d) Same as (c) in the y coordinate. Adapted from (Duqi, Bocchi, Giulianelli, Pecorari, Franchi Scarselli, & Guerrieri, 2011)

More clearly, the histograms in Figure 22.c and Figure 22.d show the dispersion shrinkage along x and y, respectively, when delivery is executed at the optimal distance. Normal density functions were generated from the same average and standard deviation of the experimental data and superimposed to both charts to evaluate their correlation with our data. The high hit ratio obtained from the experiments is confirmed by statistical analysis, as the ranges $\pm 3\sigma_x$ and $\pm 3\sigma_y$ are about equal to 100 μm which is also the diameter of the required spotting area.

3.2.4 Timing performance evaluation

Beads delivery experiments were executed while measuring the acquisition time associated with each sub-operation of the alignment and droplet delivery procedure. The stage translation time was evaluated along a serpentine path scanning all the microwells in the array, setting the most performing combination of speed (20 mm/s) and acceleration (400 mm/s2). Since measurements were performed by a stage controller LabVIEW software, an additional communication time due to software and controller protocol delays is included. Single-well positioning time is 302.4±0.5 ms (630 samples) for B1536 (Table 2). The average time required to position a single microwell, to autofocus it and to calculate its coordinates is nearly 13.97±0.823 s (192 samples) for 2.25 mm pitch array (SD64, B1536). The comparable value for SD36 is slightly larger since the distance between its wells is 4.5 mm.

The delivery procedure is conducted when all the micro-site coordinates have been predicted from those of the subset; it consists of a sequence of events, each one including: movement of the stage to align the target well with the dispenser, activation of the droplet dispenser and a message of acknowledgement sent back to the software resulting in an overall execution time defined in [45].

Table 2. Summary of the execution time of each system procedure for single markers and microwells. The reported values are obtained by averaging 5 repeated measurements for each sub-operation.

Procedure	B1536	SD36	SD64
t_a: Single-well positioning (4.5 and 2.25mm stage movement) (ms)	302.4±0.5	355.1±3.6	302.4±0.5
t_b: Microwell autofocusing (ms)	5098±352	5098±352	5098±352
t_c: Microwell coordinate extraction (ms)	868.6±20.7	868.6±20.7	868.6±20.7
$t_{exe} = t_a + t_b + t_c$: Positioning, autofocusing and coordinate extraction (ms)	6269±373.2	6321.7±376.3	6269±373.2
Acquisition time (t_{exe} n) (s)*	150.5±8.9	31.6±1.9	31.4±1.8
Acquisition time (t_{exe} N_{well}) (s)**	9629.2±106.3	227.6±13.5	401.2±11.9
Delivery procedure (s)	1057	29.1	43.34

* with interpolation
** full array acquisition

$$Delivery\ Time = \left(2 + N_{drop}\right)N_{well}T_{spot} + (N_{well} - 1)T_{\ stage} \quad \textbf{[45]}$$

Being N_{drop} the number of drops spotted per well and N_{well} the number of wells in the array, T_{spot} is the time period between two successive drops and T_{stage} is the time required for each movement of the microscope stage. In the above formula N_{drop} is incremented by two to take into account the time required by the dispenser controller to acquire and release the control to the LabVIEW software, which is equal to $2T_{spot}$. The only unknown value in Eqn. [45] is the time required for stage movement. To measure this value several spotting sequences on SD64 were performed and execution times were recorded. The best linear interpolation of the delivery time data obtained is given by:

$$Delivery\ Time_{SD64} = 192.57 \cdot T_{spot} + 43.22 \quad \textbf{[46]}$$

The single stage movement was then calculated as T_{stage} = 43.32/63 s = 688ms and the delivery time for SD64 with T_{spot} =4e−5s, Ndrop = 2 was 43.34 s. Delivery times for B1536 and SD36 can be calculated by inserting this value in Eqn. 40.

The delivery procedure was executed for the three devices comparing the execution time of the approach based on the interpolation method and the initial approach of full sampling. Despite the negligible error (<5.5 μm) obtained for the full sampling approach, the

acquisition time in this case was extremely high and not acceptable for practical use. The interpolation method, based on 24 sampled points for B1536 and 5 samples for SD36 and SD64, provided a consistent reduction of the calibration time. For B1536, the total execution time (acquisition and delivery) was 1207 s, with a reduction of nearly 11× over the full acquisition case and with the acquisition procedure occupying about 12% of the execution time. For the smaller SD36 and SD64 devices the calibration procedure occupied a larger portion of the time because of the reduced number of spotting sites which also reduces the delivery time. Comparing the SD64 and B1536 devices having the same densities of target locations, we measured an average acquisition time of 490 ms and 98 ms per well, respectively obtained by dividing the time needed to acquire and deliver over the full array by the total number of wells.

3.2.5 Conclusions and discussion

A calibration technique for the accurate delivery of liquid volume in the range of 200pL over an array of microwells fabricated on flexible printed circuit board technology has been conceived and implemented. A 3D model of the device surface was reconstructed using a procedure that interpolates the position of all the microwells in the array, starting from a subset of sampled microwells. The experimental results confirmed that it is possible to find a trade-off between minimizing the acquisition time and limiting the absolute alignment positioning error. For a flexible substrate array of microsites, with 32 rows and 48 columns, the surface was reconstructed starting from a subset of only 24 sampled locations, and the largest absolute positioning error was found to be within the specifications of 130 μm in Z direction. The proposed procedure is also about an order of magnitude faster than a straightforward calibration carried out at each location (about 150 sec. against 9600 sec.). Additionally, the 3D reconstruction method can be easily adapted to devices with different geometrical features such as area and thickness. This would only require to choose the optimal subset of sampled points which minimizes the execution time preserving an adequate spotting precision.

As a final conclusion, we demonstrated that our procedure allows an automated system based on a motorized microscope, a camera and a drop-on demand single jet dispenser to

provide an efficient fluidic interface for large area devices fabricated on flexible substrates, making it suitable for use in biotechnology and nanochemistry applications.

In contrast to the advantages described previously the system presented some fluidic issues related to the difficulty to overcome the surface tension when delivering picolitre droplets in microwell whose diameter is less than 100 μm i.e. the cell does not enter in the microwell. Furthermore, the number of cells for each droplet, generated with a piezoelectric dispenser, is regulated with a statistical approach and control of single cell delivery is difficult.

Another weakness of this working principle is related the extremely slow recovery procedure which was performed by means of a micropipette from the top opening side (Bocchi, et al., 2009). These drawbacks derive from the fact that the device is not self contained i.e. external tools are required for the delivery and the recovery of particles.

In the next chapter a second design of the open microwell array is presented and a novel method to perform delivery and recovery of cells based on embedded microchannels is illustrated. The approach based on piezoelectric external dispensing is replaced with an electrical field-based technique which allows individual isolating of a controlled number of cell/particles in suspension.

4 Cell isolation *via* nDEP-based active microchannels and open microwells

Summary: This chapter reports on a new method adopted for cell isolation into microwells by means of electrically active microchannels. Simulation based modeling, and experimental characterization with polystyrene beads are evaluated as well as the capability of the proposed active microchannel-based device to isolate K562 leukemia cells. An impedance based method to detect the cell passage by means of impedance variation is finally presented.

4.1 The *inverted* "open microwell" concept

The presented system is based on the inverted open microwell. This structure derives from the open microwell concept which was described in Figure 11. Conceptually, the structure visualized in Figure 11 has been turned upside down to obtain the inverted open microwell shown in Figure 23.

Instead of external tools for the delivery of particles, inverted open microwell arrays integrate active microchannels on the top side of the microwells to provide fluids and samples. When a fluid is inserted in the microchannel, the microwell fills by capillarity. A meniscus is formed at the open bottom side of the well, sustained by surface tension at the air-fluid interface which prevents fluid leakage from the bottom aperture.

Further, a biological sample is delivered into the microchannels by flowing changing the fluid suspension at low flow rates. Cell introduction into microwells can be selectively performed by using electrical forces to block (*Forward mode*) or free (*Load mode*) the microwell entrance (Figure 23.A-D).

Cells trapped on the fluid meniscus are expected to remain alive as happens in the well-known hanging drop technique, where cells are cultured at the air-fluid interface.

The analysis is performed optically using a direct or inverted microscope under fluorescent lighting to observe the change in fluorescent signal emitted by single cells, typically caused by the uptake or loss of one or more fluorescent dye(s). If necessary, staining can be performed on-chip by delivering the fluorescent dye through the microchannel. The last

step in the process is recovery of living cells from the microsystem and transfer to a standard microtiter plate where proliferation takes place (Figure 23.F). In the case of single cells isolated in microwells, the procedure generates monoclonal cell lines (Bocchi, et al., 2012).

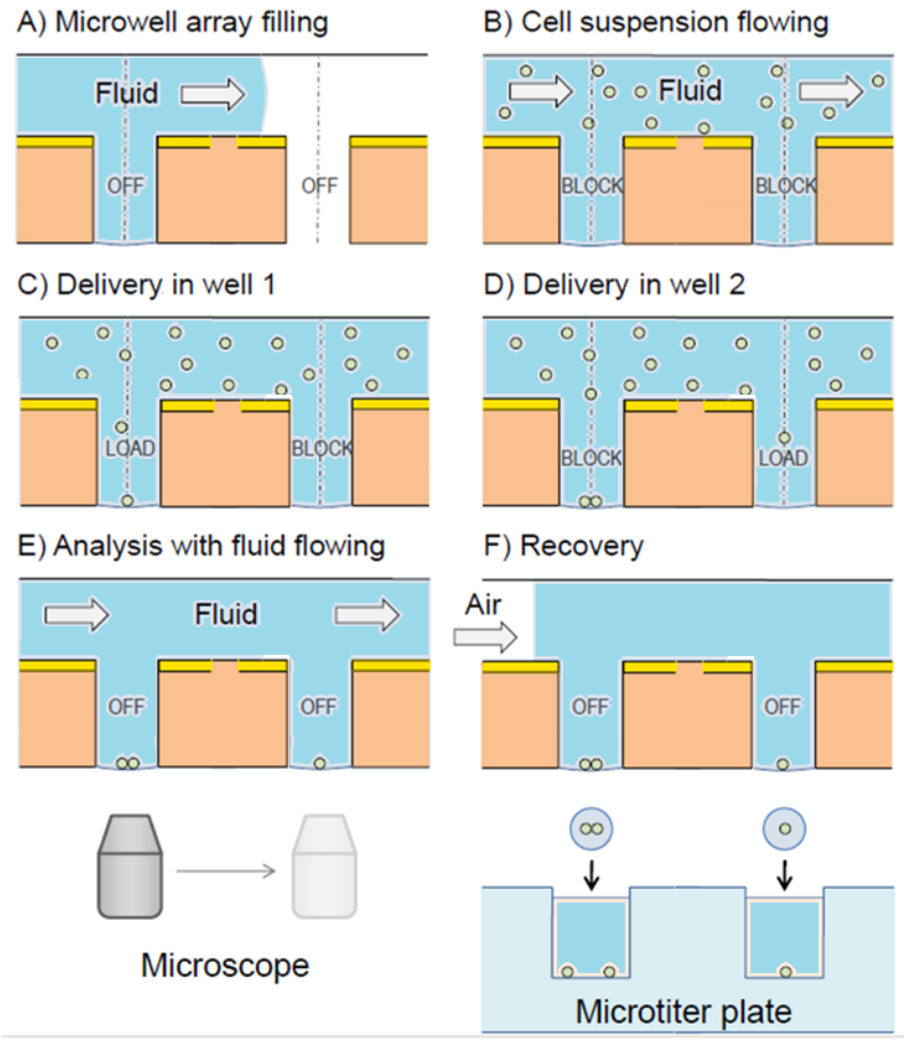

Figure 23. Workflow of the inverted open microwell system. (A) Microchannels and microwells priming with fluid. (B) Cells introduction (C) with continuous flow isolation in *Load mode* microwells. (D) Serial processing of microwells is done by activating the *Load mode* in a second microwell; (E) cells trapped at the air-flow interface remain stable with no need of electrical field based forces. and can be analyzed by a microscope, (F) after analysis live cells are separately recovered in parallel microwells onto the wells of a standard microtiter plate. Picture adapted from (Bocchi, et al., 2012).

In Figure 23 the yellow strips represent the metal gold electrodes in the substrate of the microchannels which allow selective shielding or freeing of the microwell entrance. In the

following paragraph, we describe the design steps of the microelectrode patterning which permit to bring AC electrical fields into the microchannel that exert net forces on polarized dielectric particles in suspension.

4.2 Combination of nDEP and microwells for particle isolation

A prototype of the inverted open microwell array is shown in Figure 24. It consists of three microchannels with 4 microwells each. Their cylindrical inlets and outlets ports are also visible in the figure. On the right hand we show the structures responsible for the particle manipulation and their dimensions.

Initially the particles are introduced in the microchannel's inlet. A *Focusing* stage (Figure 24) whose electric field aligns the cells in the central part of the microchannel is then encountered. Alignment of particles is done to match the cells flow direction with the microwell opening. Downstream, the particles enter in a *Detection* area where the particles to be delivered are automatically selected by an optical detection routine. The detection is implemented using an inverted microscope, a CCD camera and NI LabVIEW software.

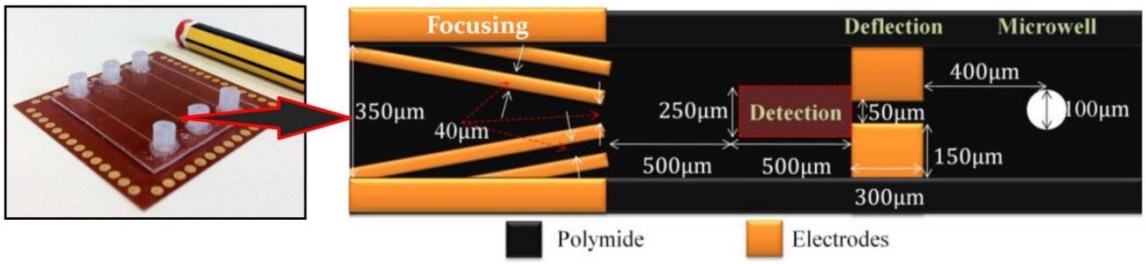

Figure 24. A prototype array of 3 x 4 microwells and detail of the active microchannel concept illustration (top view). The fluid flows in the microchannels dragging the particles in suspension. A focusing region centers the flowing particles.

After detection, cells are selectively allowed to enter the microwell depending on the signals applied to another couple of rectangular electrodes patterned in the substrate (*Deflection* in Figure 24). These signals are generated from the optical detection routine which counts the number of particles to be inserted in each microwell and shields the entrance once this number is reached.

The net DEP force, created by the electric field between the electrodes, acts as a shield and prevents the introduction of the undesired cells into the microwell. This structure forces

non-target cells to fly over the well and move along the microchannel to the next focusing stage. When a cell is selected, the shield electrodes are grounded, allowing the cell delivery into a microwell.

4.2.1 Fabrication technology: build up and electrodes design

The open microwell array devices were implemented on flexible PCB technology. This technology allows producing large area devices (tens of cm^2). The device area was made equal to that of a standard laboratory plate well. This brings the advantage to align each microwell to a macrowell one by one in parallel if the distance between the microwells and between the macrowells is also equal as well. Transferring of microwells contents to a standard laboratory mirotiter plate is strongly simplified after cell analysis into the microwell array.

The microwells were created by mechanically drilling through-holes on a 2-metal layer flexible PCB whose buildup is shown in Figure 25 under the symbol B2. The role of the integrated electrodes is to bring the electric signals from the signal generator to a precise location inside the microchannel. Since the electrodes are directly in contact with the fluid where cells are suspended, the copper electrodes were metalized with a Ni-Au galvanic process, to guarantee biocompatibility of the materials.

Microchannels were fabricated on the top side of the microwell array (Symbol B1 in Figure 25). Microchannel walls were implemented by laser cutting the single metal layer B1 flexible PCB and successive lamination with B2.

The top side of the microchannels is sealed with a polycarbonate cover. A transparent adhesive laminated at 100°C and finally cured at 70°C for 2 hours was used in order to ensure the biocompatibility of the adhesive and prevent formation of air bubbles. The cover also provides input and output fluidic made possible by drilling holes with a diameter of 0.6mm before bonding.

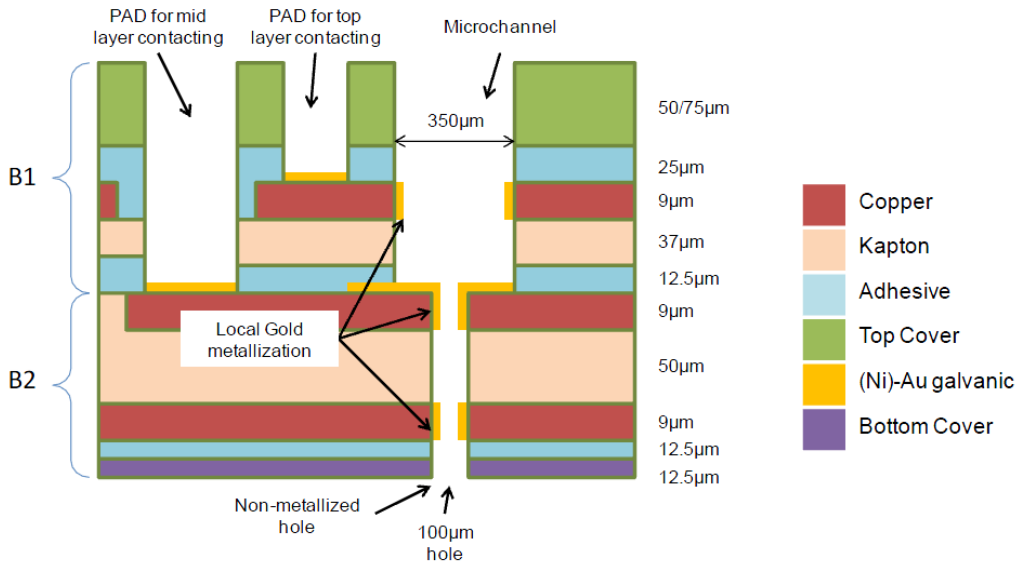

Figure 25. Device schematic layers' buildup. A combination of metal electrodes with Kapton insulator and adhesive is used to generate an electric field within the 350µm channel where particles flow.

A laser-cut cross section in correspondence to a microwell of a fabricated device is shown in Figure 26. Similarly to the virtual cut of Figure 25, in the figure below, the cut was executed in correspondence to the microwell. The result of the production process was for the most part successful. The measures in the figure are in µm.

The bottom metal layer of B2 and its role is not part of this work. Briefly we can say that its presence gives us the possibility to focus the particles which are falling within the well in order to force contact between different particles.

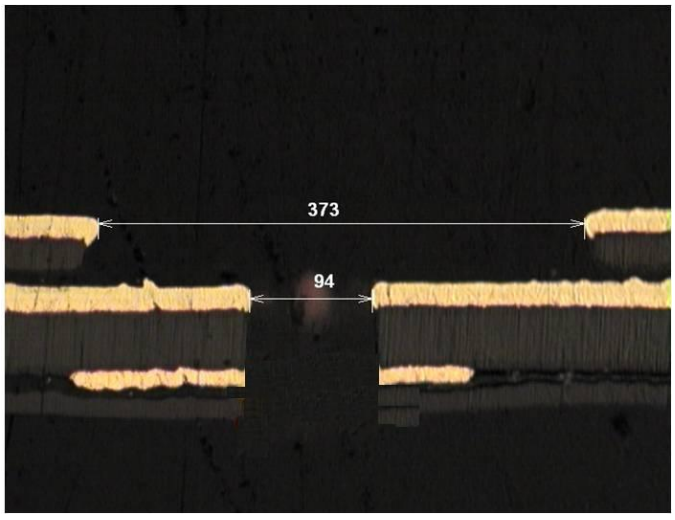

Figure 26. Cross-section of the fabricated chip in correspondence to the microwell

The main layers of the design are shown in Figure 27. Respectively the first metal layer shown in Figure 27.a corresponds to the top metal layer of B2 (in the buildup) and is used for the electrodes of the focusing and *Load/Forward* stages. The patterned electrodes are thus placed over the microchannel's substrate.

For the focusing stage these electrodes are combined with the metal electrodes in Figure 27.b which are defined in the metal layer of B1. Their combination permits to have an electric field from the top metal layer of B1 to the top metal layer of B2. It will be clear later that this electric field generates the nDEP forces necessary to align the particles in the central area of the microchannel.

The top layer (Figure 27.c) is used as the mask for the channels' sidewalls and the electrical contacts openings and is produced by laser cutting the B1 polyimide with single metal layer shown in the buildup in Figure 25.

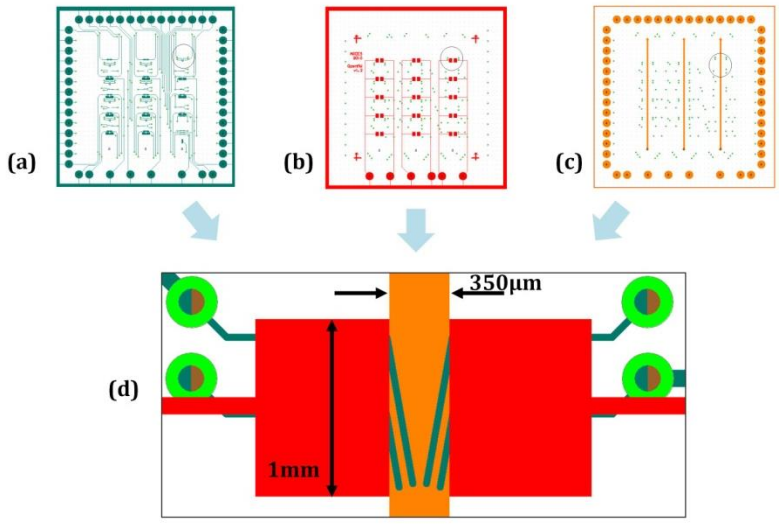

Figure 27. Masks for the device fabrication

The top view of the focusing module created by overlapping the three layers at different heights as described above is visualized in Figure 27.d. Modeling and expected functioning of the stages will be covered in the next section.

4.2.2 Actuation structures modeling and design

4.2.2.1 Numerical simulations

In order to evaluate the total force that acts on a particle flowing in a microchannel, we need to calculate the electric field distribution and the fluid velocity distribution. Both problems were solved with *ComsolMultiphysics* based on a finite elements method (FEM). The former is calculated after solving the Poisson equation (*Electric currents* module) and the latter problem is governed by the Stokes equation (*Creeping flow* module).

AC electric fields are used to avoid electrochemical effects; the frequencies used in this application range from 100kHz to 500kHz for which the dielectric response of cells is typically homogeneous and nDEP takes place (refer to Figure 9 for the CM factor trend). When applying AC signals to the electrodes an electric field is generated whose expression is:

$$\overrightarrow{E} = -\nabla(\varphi) \qquad \textbf{[47]}$$

where φ is the potential distribution $\varphi(x, y, z)$ in the our domain. For a clearer visualization the whole simulated geometry is shown in Figure 28, even though, thanks to the symmetry with respect to the *x* axis only half of it was often solved. The potential distribution is obtained after solving:

$$\nabla^2\varphi = -\frac{\rho_f}{\varepsilon} \qquad \textbf{[48]}$$

where ρ_f is the free charge density and ε is the permittivity of the material and the free charge is the solely charge responsible for the conductivity.

After applying the boundary conditions (Dirichlet for the electrodes equal to the applied potential and Neumann for the insulator) we get the electric field distribution which permits to calculate the DEP force as shown in section 2.3.

The vectorial field distribution has to be summed with the drag force field distribution and the gravity force in order to obtain the total force exerted on the particle throughout the domain.

$$F_{tot} = F_{Drag} + F_{DEP} + F_G \quad \textbf{[49]}$$

where F_{tot} is the total force and F_{Drag}, F_{DEP}, F_G are the drag , DEP and gravity forces, respectively.

For the microfluidic flow problem the equations were described in Section 2.1. The fluid is considered as incompressible and inertial terms are neglected (Stokes flow). The inlet boundary condition was set as fully developed laminar flow.

For the gravitational force calculation we considered a mass density of 1060kg/m^3 for polystyrene beads with a diameter of 10μm.

In Figure 28.d the electrodes' nomenclature is added to ease their further mentioning. We point out that A1 and A2 are shorted and the same is true for B1 and B2. This was done to minimize the number of dedicated pins by shorting some electrodes thus missing out in redundancy. The flexible PCB fabrication technology allows minimum electrodes width equal to 40μm. Also the minimum clearance between A1 (A2) and B1 (B2) is limited to 40μm. As a result of geometrical parametric simulations the focusing electrodes width and clearance were chosen at the minimum values equal to 40μm and their rotation with respect to the lengthwise direction of the microchannel is about 10°.

D1 and D2 are 50μm distant and 30μm long and were first defined in a previous design from our group (Faenza, 2011). The microchannel width and height are 350μm and 50μm respectively. The origin of the coordinate system is situated in the bottom left angle in Figure 28.a.

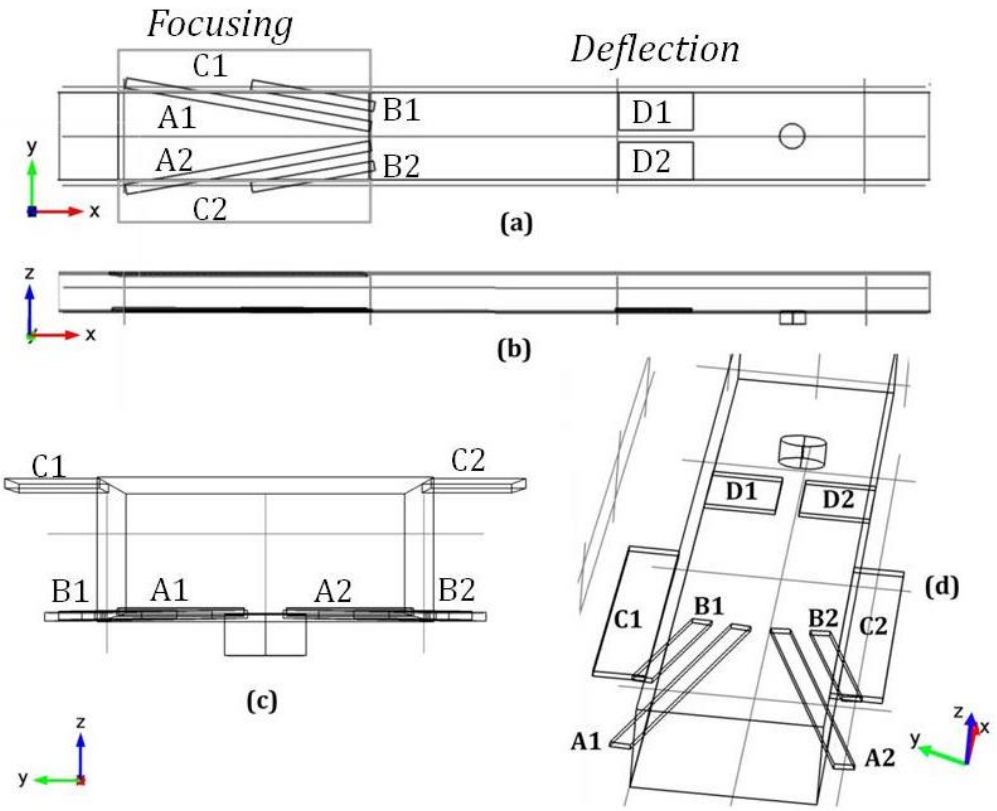

Figure 28. Microchannel's geometry used in the numerical simulations. Top (a) and side view (b). In (c) the top electrode thickness is indicated which is the same for the electrodes on the substrate. Perspective view in (d).

The device should fulfill two basic functions. The first one is to make possible the introduction of cells into the microwells. In contrast, the second function is to shield the microwell entrance. Starting from these two functions, in combination with the cells recovery procedure from the chip to the laboratory microtiter plate, a number of experiments can be performed in our device.

Analysis of cell-cell interactions, for instance, can be performed after introducing a controlled number of cells, thus forming homogeneous or heterogeneous clusters. Similarly, functional sorting based on cell response to interactions with molecules can also be achieved (Bocchi, et al., 2012).

These two fundamental functions of the active microchannel are characterized in the next sections starting with the *Load mode* (isolation of cells) and to follow with the *Forward mode* (Microwell shielding).

4.2.2.2 Load mode

This signal configuration performs nDEP focusing of particles. The result is to axially center the particles within the channel in the focusing stage. By adding π to the phase of the signals applied to the electrodes on the top metal layer C1, C2 and also to the B1 and B2 couple with respect to the A1 and A2 electrodes as described in Eqn. [27] the potential difference is continuously maximized. This result in a dielectrophoretic force barrier created between the A1-B1, A1-C1 and A2-B2, A2-C2.

No potential difference is applied to D1 and D2 electrodes in order to allow the particles passage without modifying their trajectory. This situation is obtained by applying the set of signals shown in Table 3.

Table 3. *Load* mode signal configuration.

Electrode	Applied signal
A1,A2	$V0 \cdot cos(2\pi ft)$
B1,B2	$V_0 \cdot cos(2\pi f_0 t + \pi)$
C1,C2	$V_0 \cdot cos(2\pi f_0 t + \pi)$
D1,D2	*GND*

Downstream to the focusing stage, the cells intersect the microwell opening and they fall in the microwell under the effect of the gravitational force as long as both D1 and D2 electrodes are grounded. Cells will remain trapped at the air-fluid interface at the bottom edge of the open microwell.

Figure 29 shows how the path of the cells is defined in the focusing stage by means of the electric field between the electrodes whose applied signals are indicated in Table 3. The series of slice plots in the left perspective image represent the electric potential distribution which permits to calculate the electric field and the nDEP force modulus. For each slice we show on the right the corresponding nDEP forces (contour) and the sum of the y and z

component of the total force which is obtained by summing the DEP, the drag and the gravity force defined in chapter 0.

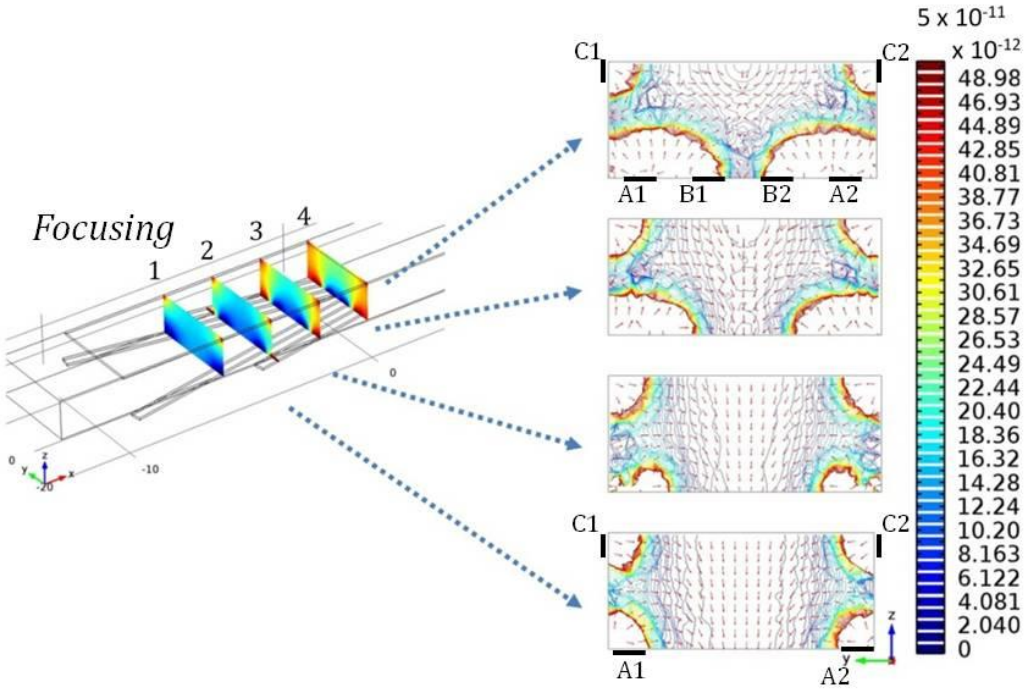

Figure 29.nDEP forces in the focusing stage. A three-dimensional focusing is achieved and particles are pushed towards the microchannel center. Signals' amplitude V_0 was 3V.

The amplitude V_0 of the applied signals was $V_0 = 2V$ which implies a potential difference of 4V between the electrodes whose signal phase is shifted of 180 deg. The resulting signal's root mean square is nearly 2.8V.

From the bottom to the top of the series we see that if we fix the upper limit of the DEP force at 50pN, due to the electrodes entering more and more in the channel, the area at which the cells are allowed to pass gets more and more restricted. We see, however, from the contours distributions that at mid-height there is an area for which it would be possible for particles flowing at that height to continue undisturbed their flow without being pushed in the channel's center. A short discussion on the force variation along the Z direction is necessary.

At given voltages, frequency (100kHz) the maximum DEP force within the domain is nearly 1.2 nN and it is encountered between the electrodes patterned on the substrate whose thickness is 9μm. In our system coordinates the Z coordinate increases from 0 to 150μm along the microchannel's height. Figure 30 shows the nDEP modulus of a cut line with X coordinate equal to that of slice number 4 in Figure 29 and Y parametric. The line's quote was varied along Z with 25μm steps.

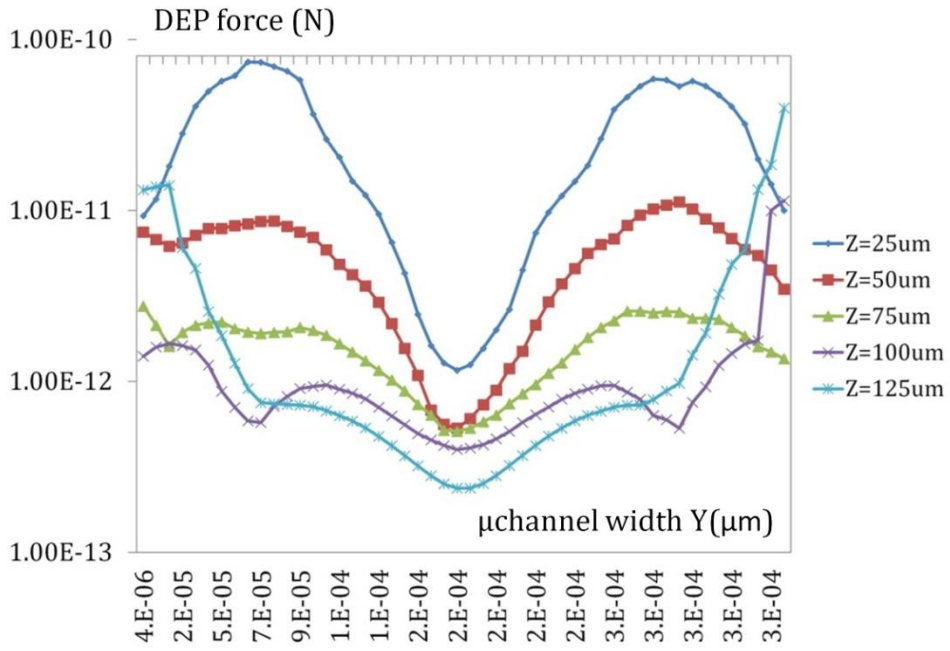

Figure 30.DEP force at cut lines with constant X and varying Y. Each curve corresponds to a different height (Z).

As expected the nDEP force modulus decreases with distance from electrodes; for particles flowing at a lower quote the dielectrophoretic barrier is much more effective. We demand at this point which is the threshold (if there is any) Z-coordinate value for which the DEP force modulus is not high enough to contrast the drag force.

In absence of flow the velocity established by the nDEP repulsion effect in a particle can be expressed as (assuming that the velocity is instantaneously set) (Morgan & Green, 2002):

$$\vec{v}_{DEP} = \frac{\vec{F}_{DEP}}{6\pi\eta R} \quad \textbf{[50]}$$

where η is the fluid viscosity and R is the particle radius. The threshold velocity is the value for which $|\vec{v}_{DEP}|$ equals $|\vec{v}_{DRAG}| \cdot \cos 80°$. The cosine factor is introduced to project $\vec{v}_{DRAG}$ into the $\vec{v}_{DEP}$ direction whose angle is 80° for rotated focusing electrodes of 10°.

The difference between these two physical quantities is shown in Figure 31 along the cutline introduced above, at different quotes. We can notice that the threshold value of Z, above where the drag force is higher than the nDEP force, is less than 50µm. It is interesting to notice that for Z=100µm the difference gives a parabolic profile which coincides with the profile of a laminar flow within a microchannel.

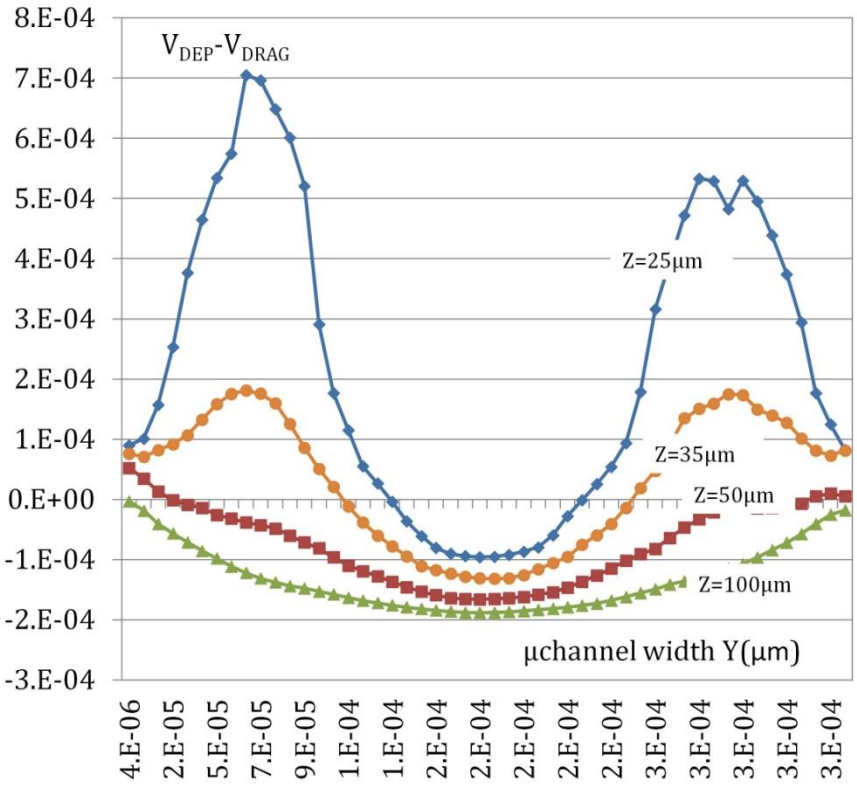

Figure 31. Difference between DEP velocity and $v_{drag} \times \cos(80°)$.

So far, the result is that if particles flow above 50μm the DEP force is not efficient to push them in the middle. As shown in Section 4.2.1 the nominal microchannel's height is 50μm and this fact guarantees the effectiveness of the focusing stage.

There is another limit in the structure, however, which derives from the necessity to introduce the particles into the microwell by gravity. It will be shown later that the fluid velocity cannot exceed some hundreds of μm/s. This value also guarantees the particles' sedimentation before getting to the focusing stage.

For a particle with radius R and mass density ρ_p suspended in a medium with mass density ρ_m, the settling or sedimentation velocity was determined in section 2.1.2 and is reported here for convenience:

$$v_s = \frac{2(\rho_p - \rho_m)gR^2}{9\eta}$$

where g is the gravitational acceleration and $\eta$is the dynamic viscosity of the fluid. Since the polystyrene density is 1060kg/m^3 the settling velocity is about 14μm/s.

To resume, by grounding the deflection electrodes D1 and D2, the microwell entrance will be 'open' only for the target cell as indicated by the streamlines in Figure 32.

By summing the drag force, the DEP force and gravity we obtain the visualized stream lines. The black arrows indicate the flow profile within the microchannel at mid-height.

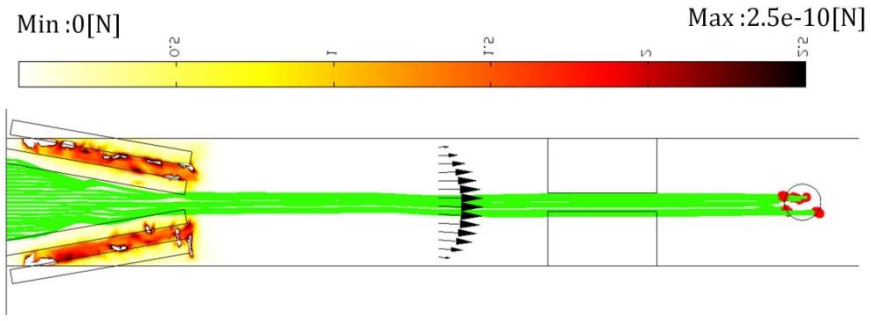

Figure 32. Load mode simulation results.

The opposed situation (*Forward mode*) is obviously the same for the focusing stage but the nDEP barrier prevents the particles from entering the microwell as explained in the next section.

4.2.2.3 Forward mode

To shield the entrance counter-phase signals with V_1=1V, f=100KHz were used for the D1 and D2 electrodes while, in the focusing stage, V_0 =2V counter-phase signals were applied at a frequency of 100kHz as described before. The applied signals are resumed in Table 4.

Table 4. *Forward mode* applied signals.

Electrode	Applied signal
A1,A2	$V_0 \cdot cos(2\pi ft)$
B1,B2	$V_0 \cdot cos(2\pi f_0 t+\pi)$
C1,C2	$V_0 \cdot cos(2\pi f_0 t+\pi)$
D1	$V_1 \cdot cos(2\pi f_0 t)$
D2	$V_1 \cdot cos(2\pi f_0 t+\pi)$

The effect is a radial dielectrophoretic force which pushes the particles toward the ceiling of the microchannel in radial directions. This barrier is able to shield the microwell entrance in combination with the drag force of the flowing fluid.

The *Forward mode* is also characterized by the highest electrical field intensity and for this case a numerical simulation of the Joule heating was also coupled to the fluidic and the electrostatic problem in *Comsol Multiphysics (*Heat transfer module*).*

The solved equation in this case is given by:

$$\nabla \cdot (-k\nabla T) = Q \quad \textbf{[51]}$$

where k is the thermal conductivity of the material and the room temperature was set equal to 20℃ (293.15K). The heat source Q is obtained from the electrostatic problem and it is equal to the dissipated power within the subdomain:

$$P_D = Q = \frac{1}{2}\tilde{\sigma}_{medium}|E|^2 \quad \textbf{[52]}$$

where $\tilde{\sigma}_{medium}$ is the complex conductivity and its expression is equivalent to Eqn. 14 with $\tilde{\sigma}_{medium} = i\omega\tilde{\varepsilon}_{medium}$.

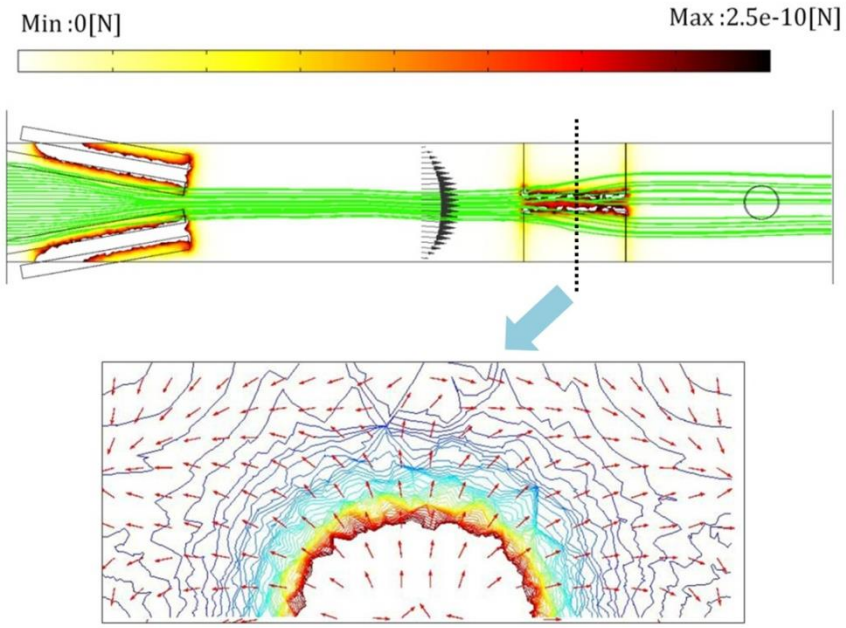

Figure 33. ***Forward mode*** **total force (streamlines) and DEP force(contour) in correspondence to the dotted line. The arrows in the bottom image are obtained by summing the DEP and gravity force.**

Joule heating is due to the power dissipated within the fluid and causes an increase of temperature which, if above 37℃ would strongly affect cell viability. Standing to the simulation results, temperature is kept below the 37℃ threshold for values of applied voltage amplitude up to V=3V, with f=100KHz and with the electrolyte conductivity equal to 0.15S/m. This is the reason for using low conductivity isotonic buffers in our experiments with cell suspensions which preserve phosphate buffered saline (PBS) osmolarity and reduce current intensity thus power dissipation at a given potential.

4.2.3 Modules for impedance measures: modeling and design

4.2.3.1 Modeling and fabrication

The detection principle involved in this thesis is optical and it will be described in section 4.3.2. As an alternative we also designed some test electrode modules for impedance-based detection of flowing cells as an alternative to optical recognition. First, this method gives the opportunity to deliver cells with high-parallelism; optical detection requires the microscope objective thus involves automated movement of the motorized stage from well to well for the *Load*. This operation can only be performed serially which limits the delivery procedure's speed.

Moreover, electrical signals processing is fast and advantageous in terms of a self-contained system.

The idea to combine electrical fields for both manipulating and measuring cells' dielectric properties has been presented in several works (Gawad S. , 2004), (Pamme, 2007), (Holmes & Morgan, 2010).

The goal is simply to identify the presence of the particle in the proximity to the electrodes. We expect that most of the current will follow the shorter path between the electrodes which are patterned in the substrate (shorter path) as schematized in Figure 34.

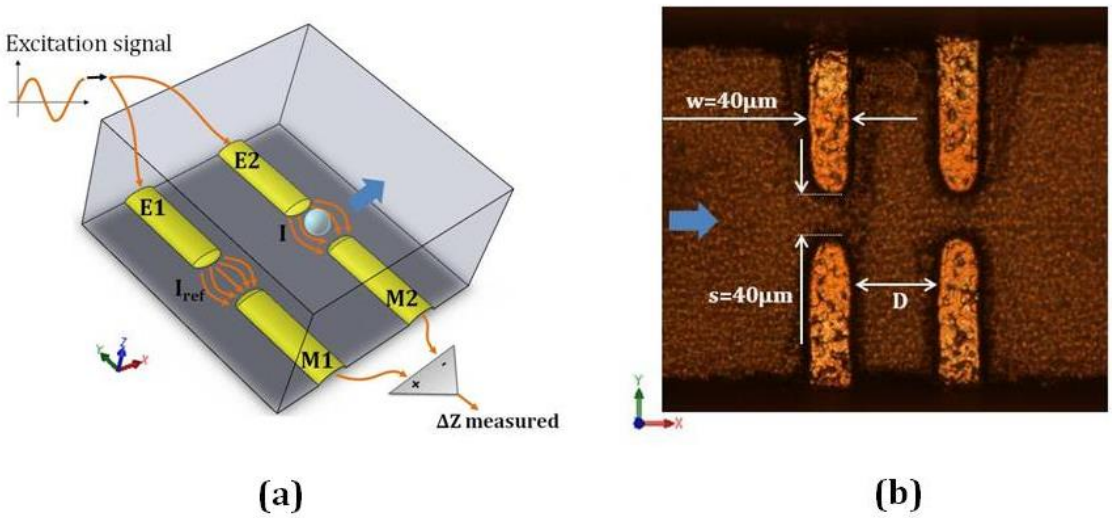

Figure 34. Sensing modules concept (a). Fabricated module and geometrical dimensions in (b).

Referring to the discussion disclosed in section 4.2.2.2, the particles' trajectory will then intersect a high density current region increasing the impedance difference between the E1-M1 and E2-M2 couples. Moreover, the sensing module can be placed downstream to the focusing stage in order to take advantage of the fact that particles can be positioned in the middle of the channel.

When a particle passes through the electrical field in the region between one of the two couples of electrodes (e.g. E2-M2 as shown in Figure 34), an impedance change occurs in that portion of the microchannel and this produces a variation in the current measured at this couple of electrodes.

The idea is to actuate the deflection module when a particle is detected, by supplying with appropriate timing a signal to the shielding stage in order to block or allow particles to enter in the microwell.

4.2.3.2 Simulation results

The geometrical design parameters were calculated with FEM simulations in *ComsolMultiphysics,* taking into account that the resolution limit of the used fabrication technology is equal to 40μm. It was shown in the previous section that the measuring principle is based on the difference between the current entering the electrodes M1 and M2. The Y position of the bead is varied now to simulate the random position of the bead in the channel's width. The Z position is fixed at the microchannels mid-height (25μm) and the bead diameter is 25μm.

The current difference is shown in Figure 35. The different curves are obtained by varying the distance between the electrode couples E1 – M1 and E2 – M2, parameterized to assess this distance effect on the current difference with respect to a flowing bead.

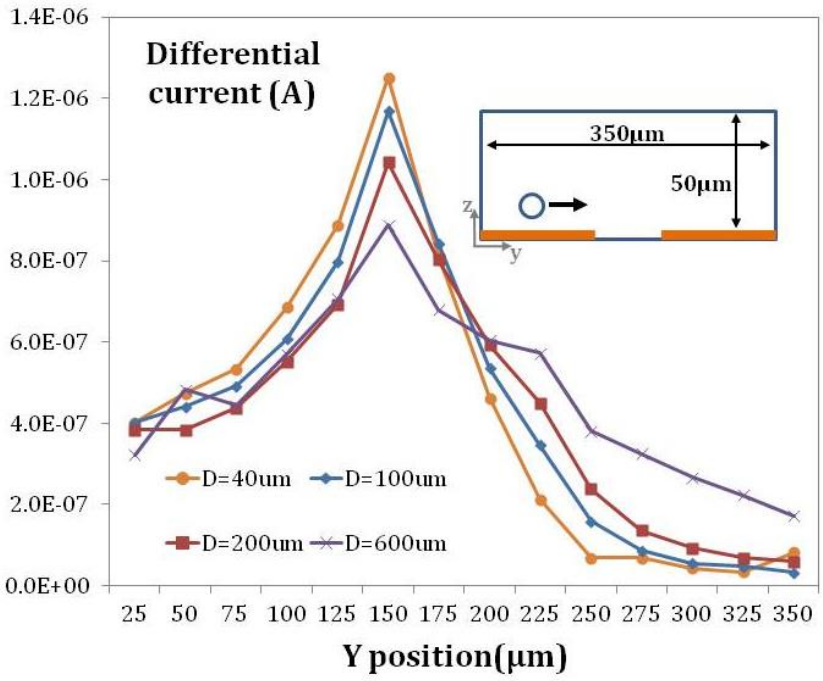

Figure 35. Current difference between M1 and M2 electrodes varying the particle Y position. Each point represents the differential current (I_{M1}-I_{M2}) obtained by integrating the current over the M1 and M2 surface. Curves chow the change induced by a bead Y position variation (The microchannel's center is at Y=175µm). The parameter D is the distance between the couples E1- M1 and E1-M2 electrodes as shown in Figure 34.

The current is maximized in correspondence to the measuring electrodes' tips and this is confirmed by the experimental results. This simulation result is not so intuitive since the electrodes are patterned symmetrically which leads to expect a symmetrical current distribution as well. It can be explained by considering the current paths of the schematic equivalent circuits of Figure 36. The following discussion is valid for the case of a low conductivity bead or cell suspended in a high conductivity medium ($\sigma_{cell} \ll \sigma_m$).

When no particle is present (Figure 36.a) the current intensities are symmetrical and their difference is zero. The cross-coupling currents are equal as well in this case.

When a particle flows through the device in an arbitrary y position away from the center of the microchannel as in Figure 36.b the current I'_1 changes, and so do the cross-paths I'_{12} and I'_{21}. An additional current flows from E2 to M1 causing the differential current to increase. This gives a non zero difference value on the microchannel sides. However, since most of the current flows close to the electrodes' tips the current intensity change is limited.

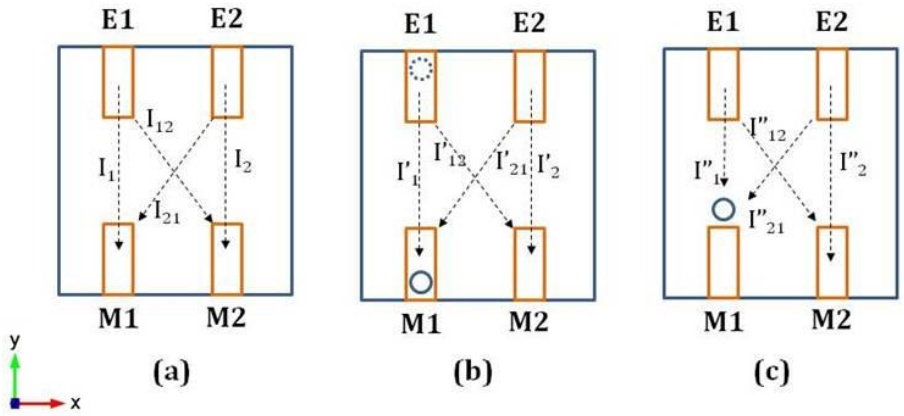

Figure 36. Current paths between the 4 electrodes in the impedance measuring module without (a) and with(b),(c) a particle. If there is no particle the current paths are symmetrical; the current difference is 0. When a particle is present as indicated from the dotted or solid line (b) the currents will change with respect to (a) but since most of the current flows in the vicinity of the electrode tips this change will be limited. In (c) the particle is placed in front of the measurement electrode. We apply a voltage in E1 and E2 and the resulting current entering in M1 and M2 is dependent from the impedance between this electrodes quadruple. In this case the E1-M1 and E2-M1 impedance is increase with a resulting decrease of the respective currents. The difference between M1 and M2 is maximized.

A different situation arises when the bead passes close to the center of the channel. The impedance of the region where most part of the current flows changes substantially in this case. This contributes to a relevant decrease of the current in paths I''_1 and I''_{21} which both decrease. In contrast, I''_{12} grows at the expense of the I''_1 and I''_{21} currents.

The overall sum of the currents remains the same for all situations but the effect of the particle on the impedance seen from the difference between the currents entering the measurement electrodes is maximized when the particle flows close to their tips. When the particle stays close to the excitation electrode tip, e.g. to E1, the other excitation electrode E2 will supply more current to the M1 electrode, contributing thus to lower the difference between M1 and M2.

As opposed to this situation when a particle is situated close to the M1 tip, minimal current will enter in the same electrode while maximum current enters in M2, maximizing thus their difference as shown in Figure 35.

The sensitivity of the impedance measuring modules was also assessed from the simulation results. To evaluate the impedance of the subdomain we first calculate the power P_e

defined as the integral of the resistive loss power density $p_e = 0.5 \cdot \sigma_{subdomain} \cdot |E|^2$ over the entire liquid domain. Then the impedance value is obtained as $Z = 0.5 \cdot |V|^2 / P_e$. The position of a bead with diameter equal to 25µm and quote in Z =25µmn over the substrate was parameterized to obtain the perturbation of the impedance depending on the bead position. Clearly the bead affects more the impedance value when it is in the middle of the electrodes where the current density is higher. In Figure 37 each point of the surface represents the impedance value of the entire domain in correspondence to the particle position (X, Y). The higher value is obtained at the electrode tips.

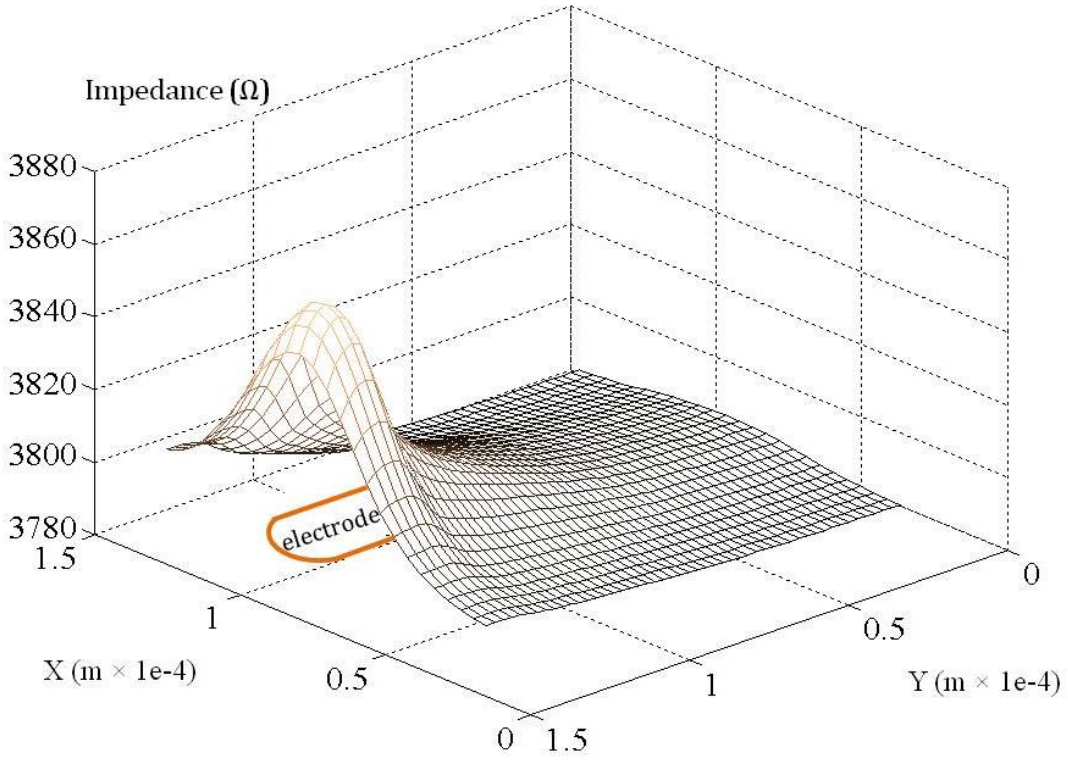

Figure 37. Evaluation of the impedance change due to the particle's position variation in X and Y with Z=25µm.

By calculating the impedance change $\Delta Z = (Z - Z_{medium})/Z$ where Z is the impedance of the subdomain with a particle and Z_{medium} is the impedance without the particle the sensitivity of the device is obtained. Since the particle flows along X, taking the maximum value of the curves at the same X gives the sensitivity dependence from Y. We get in this way the sensitivity trend of the sensing module depending in Y and the result for Y varying from 20µm (side) to 150µm (channel center) is shown in Figure 38. Looking at this chart

explains the use of the focusing stage to center the particles. The relative impedance change increases more than ten times (from 0.14% to 1.85%) for a particle moving from the side to the center of the channel.

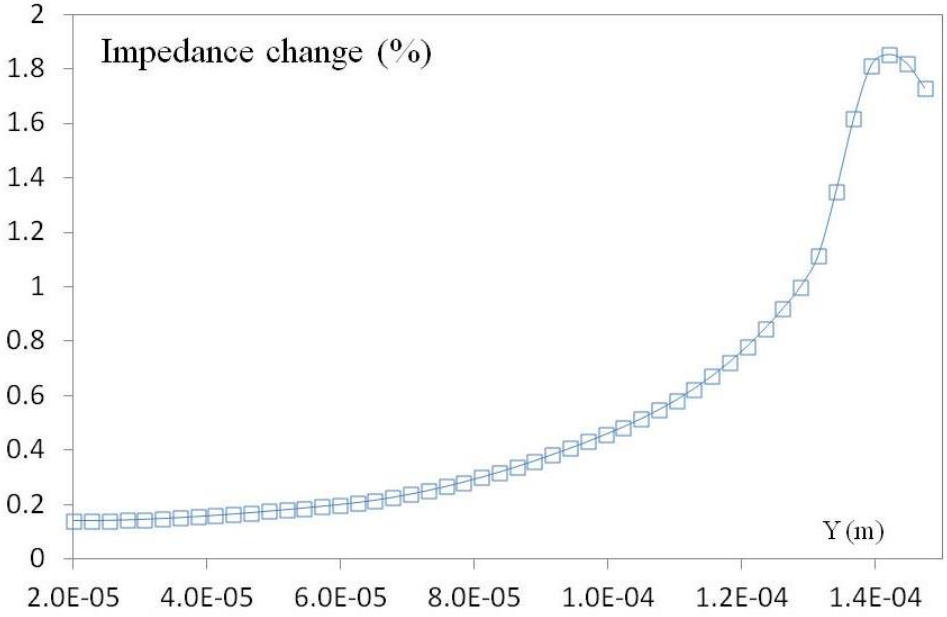

Figure 38. Relative impedance change due to the particle's position variation in X and Y with Z=25µm.

4.3 Materials and methods

4.3.1 Suspension medium

Unless otherwise specified, for all experiments with beads and cells we use a low conductivity isotonic solution which consists of 90% glycerol diluted in water to reach an osmolarity of 300 *mOsm* and 10% PBS. This buffer compound is isotonic (pH of 7.4) and has a conductivity of 0.16S/m (for PBS σ is equal to 1.5S/m, about 10 times higher). When the osmolarity is equal to 300 mOsm the solution is defined as isotonic. For applications involving the use of biological cells, bovine serum albumin (BSA) was used as a supplement to reduce cell sticking on the channel walls (with concentration 0.1% w/w). Polystyrene beads with a diameter of 10µm were suspended in the buffer. The CM factor for beads is constant over the frequency range of our application (-0.5 at given electric conductivities for the suspension electrolyte and polystyrene). The reason for using low

conductivity buffers is related to Joule heating issues in DEP actuated microfluidic channels filled with high conductivity buffers described in the previous section.

4.3.2 Software for image analysis and particle isolation into microwells

For online particle passage detection the system interfaced to the lab-on-a-chip includes a fluorescence microscope (Nikon Eclipse 80i) equipped with a Nikon DS-2Mv digital camera (up to 30 *fps*) and an XYZ motorized stage (Märzhäuser Wetzlar).

An automated system (Figure 39.a) integrates optical observation of microwells, alignment of regions of interest beneath the microscope, automated motion, microfluidics handling and image/video acquisition (Bocchi, et al., 2009). Fluid flow in the microchannels channel was provided by a model323 peristaltic pump (Watson Marlow). Manual intervention is also necessary for fluid replacing in the microchannel if needed during the experiment (e.g. channel flushing with saline solution, drugs and/or cells introduced in a second moment etc.) by simply changing the eppendorf tube. The suspension change is done usually after stopping the flow to assure a bubble-free fluid replacement. All system parts were controlled by a set of modules implemented in LabVIEW software (National Instruments) to achieve complete automation of experimental procedures.

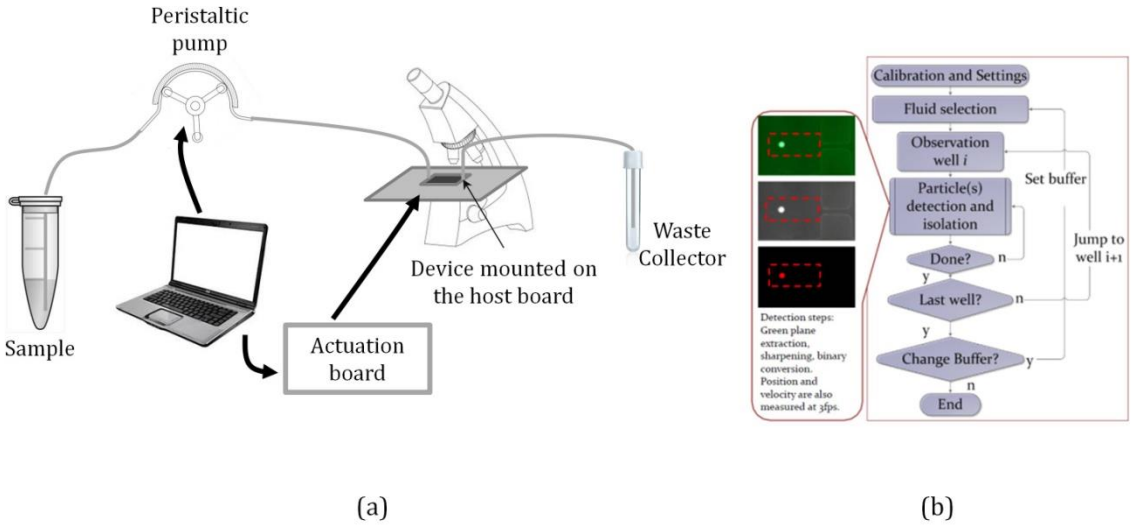

Figure 39. (a)System for automated particle optical detection and isolation *via* nDEP forces overview. Flowchart of the optical control routine in (b).

Particle tracking, whose main steps are shown in Figure 39.b, is also performed in real time by means of a LabVIEW routine which processes the frames by applying a color plane extraction to obtain the information of interest (e.g. green color plane for cells marked with calcein). The same routine produces a list of geometrical measures of the particle and evidences its position within the microchannel.

A sub-routine of the main control software for particle isolation, responsible for the optical particle detection, receives as inputs the number of particles to be isolated and the particles type (e.g. beads or cells to select the correct color plane extraction filter). The output of the routine is the isolation flag which is sent back to the main control software which, depending on the flag's value, actuates or not the DEP forces responsible for the microwell entrance shielding as shown in section 4.2.2.3.

4.4 Chip interfaces

4.4.1 Fluidic setup

The microfabrication process presented above produces fluidic channels which are sealed from the top with a Conformask cover layer which provides inlet and outlet apertures. Elastic silicon tubes with inner diameter of 0.5mm are glued at each inlet and outlet port providing a simple but very effective interface. Tubing for fluids' transfer with outer diameter of 0.6mm can be reversibly introduced in the ports by applying a light pressure (Figure 40).

The handling of liquids is performed by a peristaltic pump (Watson Marlow 101U/R) with fluid flow range between 2μL/min and 8μL/min. Cell suspensions were maintained in eppendorf tubes.

4.4.2 Electrical setup

4.4.2.1 nDEP signals generation

The custom PCB host board provides the electric spring connectors for each electrode pad present in the circuit. Cell delivery has to be performed serially one well at a time since the optical detection routine for particle detection involves the microscope positioned in the detection area. The particle detection routine has access to the electrodes control software which controls another PCB, named the actuation board, by a National Instruments Digital Input Output (DIO) interface. The actuation PCB contains 56 multiplexers (one per each chip pad) at whose output one of the four different input signals is transmitted (in-phase signal, 90 and 180deg phase-shifted signals and ground). For a detailed description of the board and the control software we refer to (Faenza, 2011).

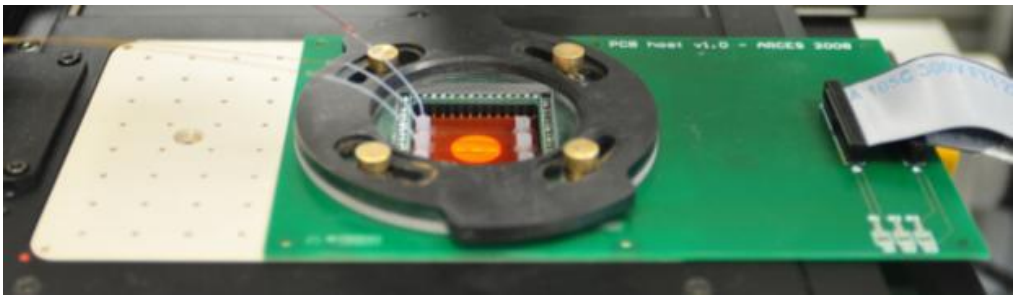

Figure 40. Host board. Picture taken from (Bocchi, et al., 2012)

4.4.2.2 Impedance measurement scheme

The PCB host board used also as a mechanical support provides the signals received from the measurement electrodes for the impedance measurements. Another PCB board was dedicated to the signal differentiation, amplification and demodulation tasks and its schematic is shown in Figure 41. The board was adapted from a previous project done in this lab[2].

At a glance, a sinusoidal signal is sent to the excitation electrodes and read from the measuring electrodes by a low gain transimpedance stage. Both channels' currents (with and without cell) are converted into voltages and further amplified and differentiated in order to get the impedance change due to the particle presence. In contrast to absolute measurements (with only one couple of electrodes) this method cancels eventual drift of the signal due to the change of physical quantities (e.g. flow rate, temperature etc.). As described in section 0 the differential signal, whose amplitude was modulated from the microchannel impedance, contains the information about the impedance change in correspondence to the excitation signal frequency.

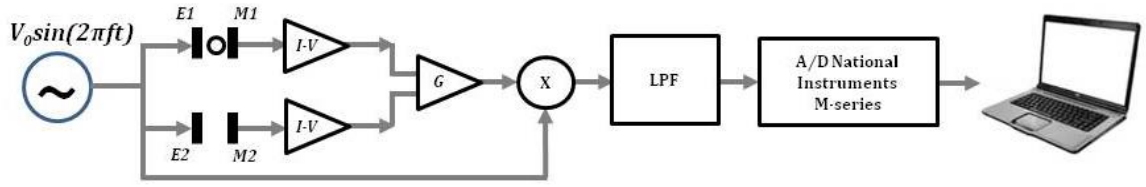

Figure 41. Electrical setup for impedance measurements.

[2]Cochise project, http://cochise.arces.unibo.it/

To extract this information from the modulated signal, it is multiplied with a sinusoidal wave at the same frequency of the excitation wave (carrier signal). We obtain (Eqn. 32) a voltage with doubled frequency whose DC value is dependent on the impedance change. Data were acquired in LabVIEW using an 18 bit ADC converter (M series National Instruments).

4.5 Focusing of polystyrene beads

The first electric manipulation of particles that flow in the microchannel is the deviation of their direction. This focusing operation is the result of two counter acting deviating structures. At this purpose two pairs of electrodes rotated of 10° with respect to the lengthwise direction of the microchannel are used to achieve the focusing of 25μm polystyrene beads. The image shown in Figure 42 is the result of the successive subtraction of 125 frames taken at 25 *fps;* the processing was performed in Matlab. The trail of four beads can be easily identified in the figure. The applied electric field is the same for both couples of electrodes.

Figure 42. Tracking of the particle focusing for 25μm beads with a constant $\Re(f_{CM})$=-0.5. The fluid speed was 150μm/s and the image is obtained by subtracting 100 frames.

The calibration with beads permits to first investigate the influence of the flow rate, signal frequency and amplitude on the particles' direction. For example, below a certain speed (40μm/s with 2.8V_{rms} at 100kHz) the nDep force acts as a barrier and blocks particles in the middle of the electrodes' tips. The number of trapped cells is limited from the volume between the inner electrodes tips. Usually not more than 3 or 4 beads can be trapped at a

time at the given voltage. If other particles arrive at the tips they will circumvent the trapped particles and proceed focused along the channel.

Above this speed, the particles are axially focused in the microchannel. Further increase of the flow rate prevents the correct focusing of particles as shown in Table 5 where we show the dependence of the focusing efficiency from the flow rate.

The velocity of the particles was calculated by converting the traveled distance of each bead from pixels' number to μm (Figure 42). The pixel number was measured after overlapping a fixed number of frames and, under the assumption of constant velocity, by dividing the corresponding distance in μm with the frame rate of the camera whose unity is *frames per second*.

Table 5. Focusing efficiency with varying particles velocity. Voltage amplitude V_0 = 2V at 100kHz

% of correctly focused beads	20μm	40μm	60μm	80μm
30μm/s	100	-	-	-
60μm/s	100	-	-	-
90μm/s	75	91.7	100	-
180μm/s	56.5	72.7	91.3	100
250μm/s	45.5	62.5	74	88.3

The columns' headers of Table 5 represent a virtual stream width at the focusing stage output. The result is the percentage of cells which flow within the selected stream width at given velocities and applied voltage. Since the microwells' diameter is equal to 100μm an upper limit of the velocity of about 180μm/s can be deducted from the table in order to have all flowing particles conveyed within 80μm at the output.

4.6 Continuous flow isolation of K562 leukemia cells using nDEP

The initial set of focusing electrodes pushes the cells into a tight axially centered beam using negative DEP forces as shown in Figure 43. This ensures that all of them follow the same trajectory at the maximum flow rate within the device (parabolic profile flow). For the following tests a cell concentration of 10^5/mL was used.

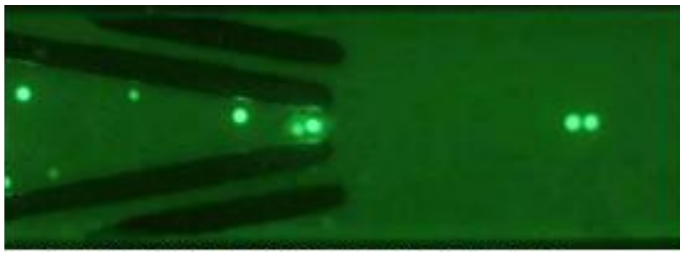

Figure 43. K562 calcein marked cells in the focusing stage.

In Table 6 the results for both *Load* and *Forward* modes are shown. The yield of the controlled delivery was studied in the particles speed range from 40 to 100μm/s. The maximum velocity is marked based on the necessity to introduce the cells in the well by gravity and was experimentally determined by sweeping the flow rate of the fluid in the microchannel.

Considering velocities less than 80μm/s, the *Load mode* yield is on average 93%. An error rate of 7% is due to the presence of closely flowing particles that are detected as single particles. At 100μm/s only 12% of cells are trapped within the well because of higher drag forces. A typical situation of the *Load mode* is shown in Figure 44.a.

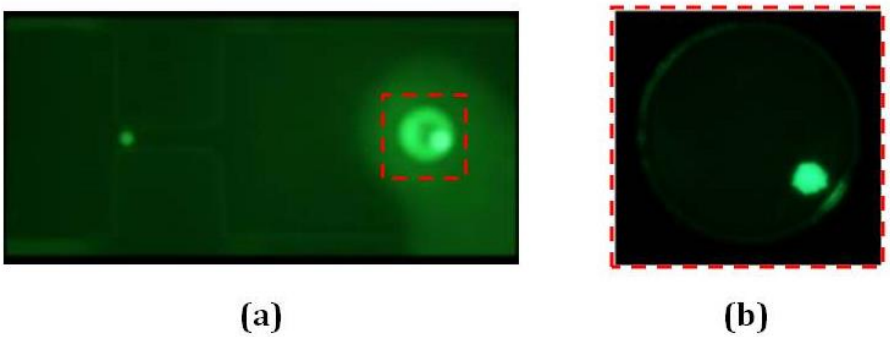

Figure 44. (a)One cell flowing between the deflection electrodes in Load mode and another cell trapped in the microwell. (b)Detail of the trapped cell

The *Forward mode* instead, has a yield of 100% applying 1Vrms signals to the deflection module electrodes, for particles velocities of more than 60μm/s. For lower flow rates i.e. lower drag force, particles still fall inside the microwell since the sedimentation velocity is high enough with respect to the drag velocity and particles sedimentation into the wells takes place (25% at 40μm/s).

Table 6. Forward and Delivery modes yield. Each value was obtained from about 100 events.

Particles velocity (μm/s)	40	60	80	100
Load ($V_{rms,focusing}$=2.8V)	96%	94%	90%	12%
Forward ($V_{rms,focusing}$=2.8V, $V_{rms,deflector}$=1V)	25%	100%	100%	100%

Table 6 includes also the optical detection routine efficiency. The delivery yield is in average is about 93% and this is related to the fact that clusters of particles are recognized as single cells. The problem of the cells adhesion is limited somewhat by adding *Bovine serum albumin (BSA)* with concentration 0.1% (*w/w*) and this permit to have only 4% of adherent cells.

The cells' viability was assessed by arresting the fluid flow after cells were exposed to the worst case configuration in terms of electrical field intensity (*Forward mode*). Successively, a calcein release assay in the microchannel was performed. After 60 minutes a fluorescence intensity of 93±6% was measured (control 96±4%). The decrease from the initial intensity is consistent with a physiological loss (Figure 45).

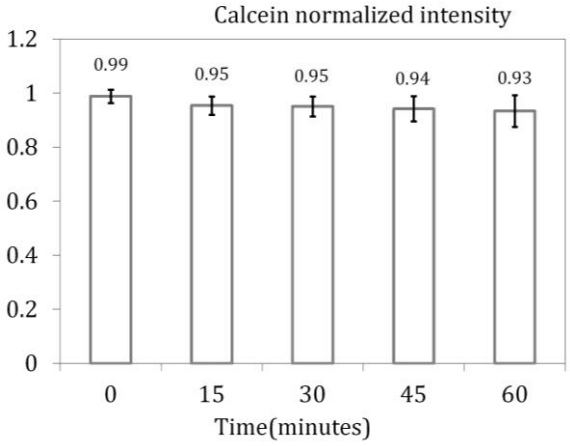

Figure 45. Calcein release over time to test cells' viability

The creation of groups of heterogeneous cells and beads in each microwell is also possible and examples are shown in Figure 46. Cells and/or particles can be put in contact in a microwell array. Since online supernatant substitution is also allowed single-cell centrifugation is enabled and the analysis of the drug particles' interactions response is possible.

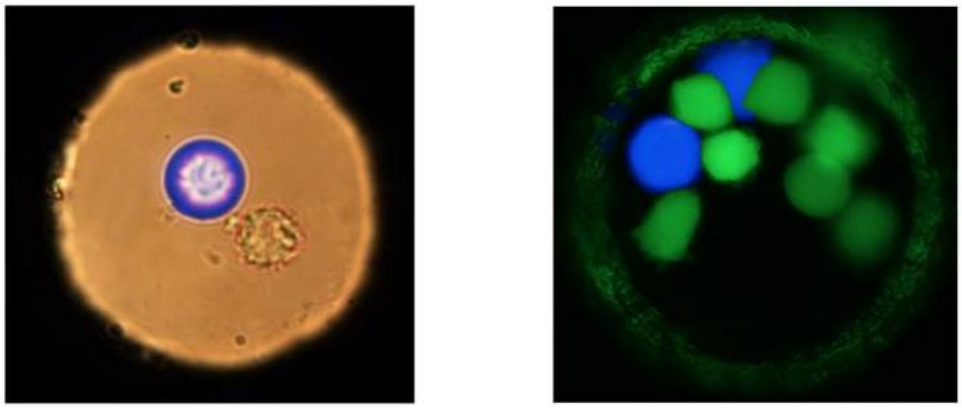

Figure 46. (a) A blue fluorescent 10µm bead is trapped with a K562 cell in a microwell. (b) Cluster of beads and cells.

4.7 Continuous flow impedance based detection of flowing beads

In order to determine the effects of the DEP focusing electrodes, 25 μm beads suspended in PBS were measured with (Figure 47) and without DEP focusing. nDEP force pushes the beads and focus them to the center of the channel, thus decreasing the spread in signal amplitude i.e. the measured impedance change due to the passage of a cell. Using different frequencies for the actuation and the sensing excitation signal and thanks to the lock-in principle the actuation signal can be filtered easily from the impedance measure. The frequency of the nDEP actuators was about 100kHz whereas the frequency of the excitation signal for sensing was 145kHz. Using different frequencies is crucial to eliminate the cross-talk between the focusing electrodes and the measurement sensing electrodes. These frequencies must not be multiple of each other as well, to avoid coupling of higher harmonics.

As said above, high conductivity buffer was used for the suspension; when the measurement impedance is low small variations due to the particle presence are better detected.

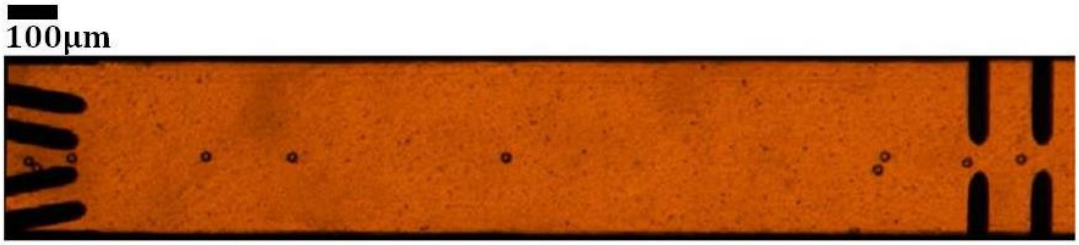

Figure 47. Beads with diameter of 25μm in the focusing stage and the sensing module. Magnification 4.00x.

Measurements without DEP focusing show a 50.7% variation in signal amplitude, while DEP focusing decreases the signal amplitude variation to 11.2%. The typical measured signal from the impedance measures is a double peak pulsed shape as the ones shown in Figure 48. Each extrema correspond to the particle passage between each of the electrodes couple.

Comparing the two waveforms it can be noticed that at the cost of a lowering of the peaks' average amplitude the signal in Figure 48.b is more uniform.

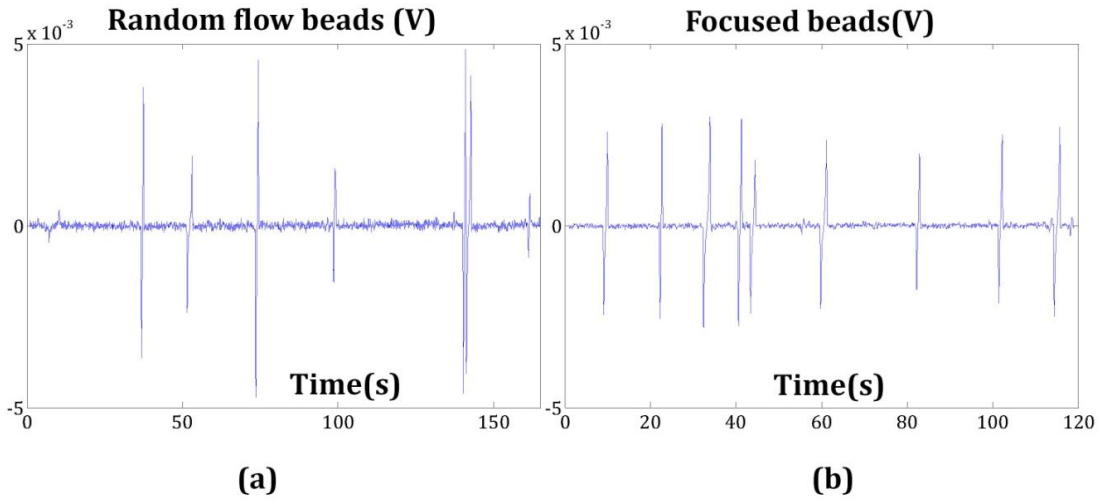

Figure 48. Not focused beads(a), Focused beads (b).

To quantify the focusing effect the signals were arranged into histograms and this shows once again the amplitude average decrease for the focused signal. We must specify, however, that these modules are still in a study step.

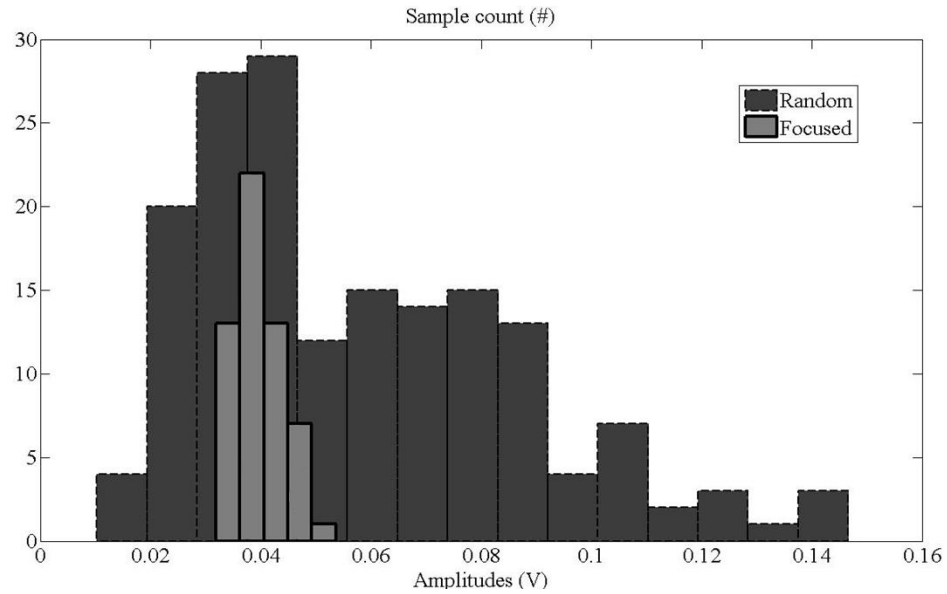

Figure 49. Histogram of the peak amplitudes for focused and non focused particles. Focusing reduces the amplitudes' dispersion at the cost of a lower average of the signal amplitude.

The beads' volume we used for the experiments is about 5 times larger than the average cells volume and the size dispersion of the cells would contrast the signal uniformity. For the non-focused 25μm beads we get μ_1 =0.06, σ_1 =0.029, resulting in CV≈50%. Data from the focused particles present μ_1 =0.04, σ_1 =0.0045, with CV≈11%.

4.8 Conclusions

In this section an innovative design for a Lab-on-a-Chip based on arrays of open microwells for the isolation of single cells or controlled-number clusters of particles was presented. The isolation is performed by manipulating with electrical fields the particles flowing in microchannels on whose substrate electrodes are patterned. Automated introduction of particles into the microwells is made possible by a microscope-based optical detection routine. The parallel interaction of cell-cell and cell-particle is possible after isolation. Potentially, online drug perfusion during the experiments is possible for cell-drug analysis. The platform allows sample recovery after analysis with a fast parallel transfer from each microsite to a traditional microtiter plate.

The fabrication technology uses flexible polymeric materials which allow for cost-effective large area devices in order to maintain geometric compatibility with microtiter plates

A major operative limit is related to the serial delivery of particles well by well based on the optical detection routine. To overcome this, some testing modules for impedance detection of flowing particles were introduced in the design of the microwell array.

The difficulty of introducing an optimal design for impedance measurements in the presented device is related to the presence of the air/fluid interface for each microwell. The microchannels' section is dimensioned in order to minimize the pressure within the microchannel (Bocchi, et al., 2012) avoiding leaking from wells.

In summary, if on one hand parallel recovery of particles involves large channels' section to avoid leaking, on the other, the impedance difference due to the particle's presence is related to the ratio between the cell and the detection volume.

Besides the large measurement site volume, the beads we used have a diameter of 25 μm which, compared to a cell with a diameter of 7.5μm, results in a volume 4.6 times larger. It was evidenced in section 2.4 that the ratio of the particle volume over the measurement site

volume directly impacts on the impedance difference. Cells also present size dispersion with a coefficient of variation up to 30% while the beads are size calibrated with CV=1%.

5 Impedimetric measures to monitor the toxicity kinetics induced by Listeriolysin-O in mammalian HeLa cells

Summary: This chapter part resumes 6 months of research activity carried on at the *Microsystems Laboratory 4* at the *EPFL (École Polytechnique Fédérale de Lausanne)*.
It reports the development and the validation of a new method to measure single cells impedance based on a microfluidic flow cytometer which makes use of a simple fabrication process with a single metal layer. The analytical and numerical modeling of the chip and the fabrication of the microfluidic devices by means of standard photolithography techniques is initially described. The electrical setup which features the possibility of performing measures at multiple discrete frequencies is then shown. After the first measurements accomplished with size calibrated microbeads and HeLa cells the chip is finally used for the monitoring of the effect of bacterial toxins on mammalian cell membranes.

5.1 Impedance spectroscopy for biological measurements

Microfluidic cytometers can detect, count and analyze particles using impedance measurements (Ayliffe, Frazier, & Rabitt,, 1999). They can characterize cells in a label-free way using low-cost and portable devices, providing a powerful alternative to conventional optical cytometers. Applications include analysis of erythrocytes, leukocytes and yeast cells.
Various electrode configurations have been used to measure the properties of the cells, including coplanar electrodes and parallel facing electrodes. A coplanar design has the advantage of being easy to fabricate with a single metal layer, but creates electrical fields restricted to a fraction of the channel area. On the other hand, parallel facing electrodes offer a better field distribution and are generally preferred due their better performance as a result of smaller measurement sites volume. This design however requires electrodes on both the top and the bottom of the microfluidic channel, making the fabrication more complex, including the patterning of two separate substrates, and aligned bonding of those (Gawad, Cheung, Seger, Bertsch, & Renaud, 2004).

This brings obstacles towards cost-effective, possibly disposable chips for commercial impedance cytometry applications.

Recently, a new electrode design using a single planar electrode layer have been developed for cell focusing by lateral dielectrophoresis (Demierre, Braschler, Linderholm, Seger, & Renaud, 2007). This design uses so-called "liquid electrodes", which are recessed electrodes patterned at the bottom of dead-end chambers positioned perpendicularly to the main channel. They provide a homogeneous electrical field over the total channel height while keeping a simple process flow with a single planar metal layer.

This chapter presents the characterization of a design based on liquid electrodes for impedance flow cytometry, and its application to the measurement of cells response over time to the presence of a pore forming toxin. The relative impedance change due to the cells presence is studied by numerical simulations and compared with other designs. Measurements are then performed for the specific application.

In the next section the chemical reversible permeabilization of cells is depicted giving particular emphasis to the link between cell membrane damages and impedimetric measurements.

5.2 Reversible permeabilization of cells *via* pore forming toxins

Plasma membrane represents a major barrier for the delivery of macromolecules into the cell cytosol. Selective and reversible permeabilization of the membrane is a prerequisite for many biotechnological applications. Transferring of macromolecules into living cells modifies specific cytosolic processes and provides an effective way to study the systems that underlie basic cellular functions. The general principles of membrane permeabilization are based on biological, chemical, and physical methods. Some examples of membrane permeabilization techniques are microinjection, electroporation and chemical. Microinjection consists of a mechanical process in which a needle penetrates the membrane to deliver the contents inside the cell. It is a technically demanding technique and furthermore the number of cells that can be permeabilized is restricted (up to 200 in one experiment) (Stephens & Pepperkok, 2001). Electroporation or electropermeabilization is widely used in molecular biology to introduce substances into a cell, such as proteins or

molecular markers. It is advantageous because it can be applied to a wide range of cells. In contrast, specialized instrumentation is required and better efficiency is obtained with cells in suspension.

Chemical techniques are also used to reversibly break the membrane barrier of adherent and suspension cells. These methods are mainly based on the use of the pore-forming toxins (PFTs) which are bacterial secreted proteins. The advantages of this technique are high efficiency and the large number of addressable cells. It is also cost effective and simple to perform. On the other hand, however the size of the molecules that can be taken up cannot exceed 100kDa.

Cholesterol-dependent cytolysins (CDCs) represent a large family of PFTs secreted by several bacteria such as *Streptococcus myogenes*, *Listeria monocytogenes* etc. Streptolysin O (SLO) and Listeriolysin O, prototypes of CDCs which are produced by *Streptococcus myogenes* and *Listeria monocytogenes* form very large pores (up to 35nm) in the plasma membrane of mammalian cells (Gilbert, 2010). Under certain conditions, cells can repair lesions (Walev, Bhakdi, Hofman, Djonder, Valeva, & Aktories, 2001) and protocols for delivering proteins have been established.

The existing methods for evaluating the timing constraints of the cells' reaction to the presence of a toxic agent in the extracellular medium are mainly optical. Staining with Trypan blue or propidium iodide is performed after the cells' exposure to the PFT and the percentage of positively stained cells is evaluated by microscopy or Fluorescence-activated cell sorting (FACS). Chemiluminescent measurements of ATP levels are also performed to assure cell recuperation.

Prompted by the use of FACS in these studies we ventured to monitor the kinetics of the cell response to the Listeriolysin O (LLO) pore forming toxin *via* an impedance flow cytometer. Cell impedance spectroscopy is a label-free and harmless method which can single out high-content multifrequencial data to analyze cell size, membrane capacitance and cytosol dielectric properties. At low frequency signals the plasma membrane capacitance represents a major barrier to the AC current which flows mainly around the cell and permits to obtain information on the cell size. At higher frequency the membrane interfacial polarization is lower, the current enters the cytosol and the cytosol impedance will contribute to the measured impedance.

Single cell dielectric spectroscopy has been already used in a number of studies. Experiments have been conducted with human erythrocytes (Gawad, Schild, & Renaud, 2001), Babesia bovis (Kuttel, et al., 2007), HeLa cells (Malleo, Nevill, Lee, & Morgan, 2009). A summary of the recent microfluidic impedance-based flow cytometry systems and their applications can be found in (Cheung, et al., 2010) and in (Sun & Morgan, 2010). In this study we monitor the kinetics of the response of HeLa cells to the attack of LLO pore-forming toxin using a microfabricated dielectric flow cytometer. The chip design is based on large coplanar electrodes and was characterized in a previous work (Demierre, Braschler, Linderholm, Seger, & Renaud, 2007) for dielectrophoretic based cell sorting. The electric field distribution within the structure is studied by analytical and numerical simulations and the sensitivity of the device is compared with other chip designs. We were able to distinguish dielectric and morphological changes caused by the damage of the plasma membrane by studying the impedance.

5.3 Microfluidic device design and technology

5.3.1 Introduction

Several techniques have been developed over the last century to measure the dielectric properties of biological particles in suspension. Most of these techniques provided an averaged value of the cell population impedance except for the Coulter counter[3] (Koch, Evans, & Brunnschweiler, 1999). More recently, with the advent of the Lab-on-a-chip it has been possible to single out individual properties of cells in suspension. In general the impedance of a suspension is measured by sending an AC signal to a measuring site that consists of a certain number of electrodes faced in a chamber which is filled by the suspension fluid. The impedance spectrum of biological particles depends on the frequency of the applied signal. Measuring cells at different frequencies allows retrieving high-content information on their electrical properties. Typically, at frequencies in the MHz range, the so-called beta-dispersion originating from interfacial charges described in

[3] A typical Coulter counter consists of two chambers containing electrolyte cell suspensions, separated by a small orifice. As fluid containing particles or cells is drawn through the orifice, each cell causes a brief change to the electrical resistance of the liquid. The counter detects these changes in electrical resistance by means of two electrodes one situated in each chamber.

section 2.2 can be observed. Low frequency measurements allow the determination of the cell size, whereas measurements at higher frequencies provide information of the properties of the cell membrane and cytosol.

In contrast to the dielectric spectroscopy, on the two last decades AC electrokinetics has been preferred to other techniques for single particle analysis. This method studies the mechanical response of particles that are subject to an electric field. Induced dipoles are formed in the particles by interfacial polarization and if the electric field is non-uniform they are subject to a net force (DEP) which causes the movement of the particle.

A torque is exerted on a dipole subjected to a rotating electric field; this gives rise to electrorotation (ROT). Several studies about the numerous approaches for these measurements have been published (Cheung, et al., 2010).

The principal advantage of DEP and ROT is the independence of the method from the volume of the measuring chamber, this occurs because the polarizability of the particles is directly measured. However, the frequency-dependent property of DEP and ROT is respectively, the real or the imaginary part of the Clausius-Mossotti factor, making necessary using both measurements in order to obtain the impedance modulus. The measurement speed can be another major limitation for ROT measurements, because it introduces an upper bound on the measured cells number per experiment.

Impedance spectroscopy can be used to measure the dielectric properties of single cells at high speeds in contrast with DEP and ROT. Microfabricated impedance-based flow cytometers can detect and analyze cells in microfluidic channels equipped with electrodes to continuously probe the mixture dielectric properties.

5.3.2 The “liquid electrode” concept

In this work we use an arrangement of large planar electrodes presented in (Demierre, Braschler, Linderholm, Seger, & Renaud, 2007) for flow cytometry measurements. The design has already been used for DEP sorting (Demierre, Braschler, Linderholm, Seger, & Renaud, 2007) and impedance measurements as well (Kuttel, et al., 2007).

The device consists of a measurement main channel intersected by lateral dead end chambers at whose substrate the metal electrodes are defined (Figure 50). When an AC

voltage is applied on the electrodes, an electrical field is created from one side to the other perpendicularly to the main channel. The side openings can be approximated as equipotential, this is the reason the planes corresponding to the openings are called "liquid electrodes" (e_1 and e_2 for the excitation side, m_1 and m_2 fort the measurement side). A simplified illustration of the structure is presented in Figure 50.a whereas a picture of the measurement area is shown in Figure 51.b. The coplanar metal electrodes are very large with respect to the microchannel (mm^2 against μm^2) and this provides high interfacial capacitance and robustness since the current density will be lower at a certain applied potential.

This setup features a microfluidic chip in which each cell flowing within a detection site is measured individually. A differential scheme as shown in Figure 50.b is implemented. The impedance difference induced by flowing particles will be reflected in the measured current which is converted into a voltage. The signals coming from both channels are subtracted and amplified in order to give the final characteristic pulse shaped signal[4] shown in Figure 50.b.

Since the cell impedance is frequency-dependent more frequency signals are mixed to obtain the excitation signal. At low frequency, the membrane of the cell represents a major barrier to the current lines and the impedance amplitude is related to the extracellular current thus revealing information about the cell size.

The low frequency current depends only on the relative volume of the cell compared to the measurement site volume and it was the detected parameter in the first impedance cell counting system, the Coulter counter (Hoffmann & Britt, 1979). At high frequencies, membrane polarization is minimal and part of the current flows in the intracellular volume giving information about cell interior complex permittivity. The ratio between the amplitude of the detected peak shown in Figure 50, at high frequency (HF) and low frequency (LF) is named opacity. This parameter abstracts the measurement from the particle size and from its position between the electrodes in the microfluidic channel.

[4] The pulsed shape signal shown in the figure is obtained from a 3d simulation of the structure with *ComsolMultiphysics*. Details about the model and simulation settings are described below.

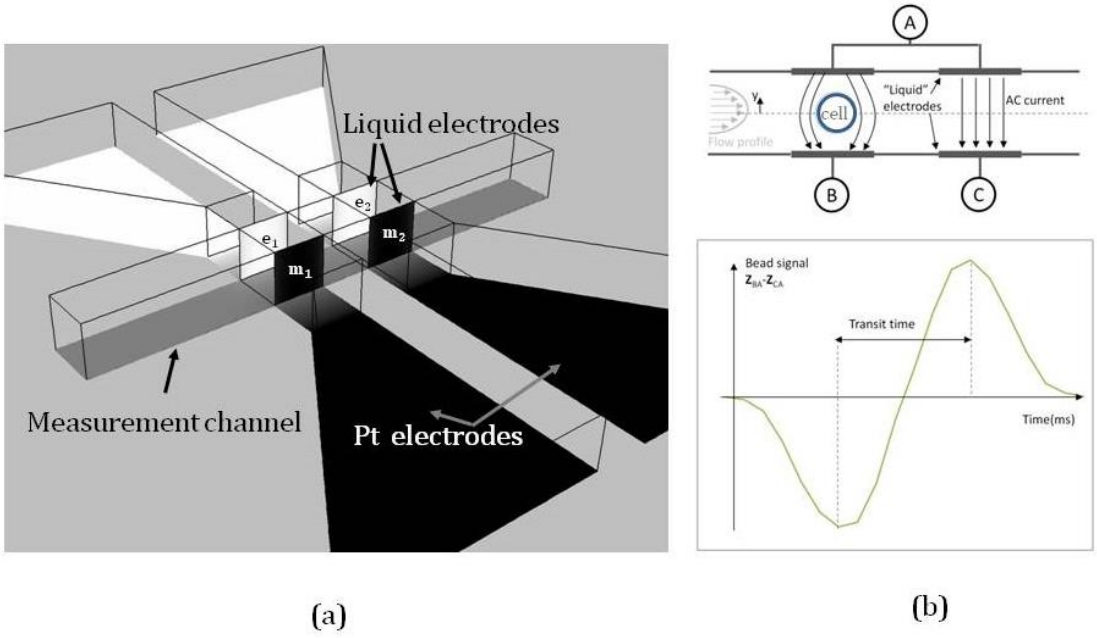

Figure 50. Impedance flow cytometer and liquid electrode concept. (a)The liquid electrodes noted as e_1, e_2 for the excitation side, m_1, m_2 fort the measurement side. Because of the quasi-uniform potential distribution in these surfaces the access channels openings are named liquid electrodes. The grayscale map represents the potential distribution within the structure when a difference of potential is applied between the excitation and the measurement metal electrodes. (b)Top view of the impedance flow cytometer. When the cell passes between the electrodes it alters the current lines. The detection volume impedance changes are quantified by measuring the current. The measurement scheme is differential to reduce drift and multi-frequency signals are applied to the excitation electrodes to give information about the cell size or cytoplasm dielectric properties.

5.3.3 Sensing area

The present differential measurement technique makes use of two couples of liquid electrodes and a reconstruction is shown in Figure 51.a. Cells pass sequentially through the microfluidic channel dragged by the pressure-driven flow and are analyzed individually. The detection principle is the current perturbation of two electric field regions caused by the cells presence.

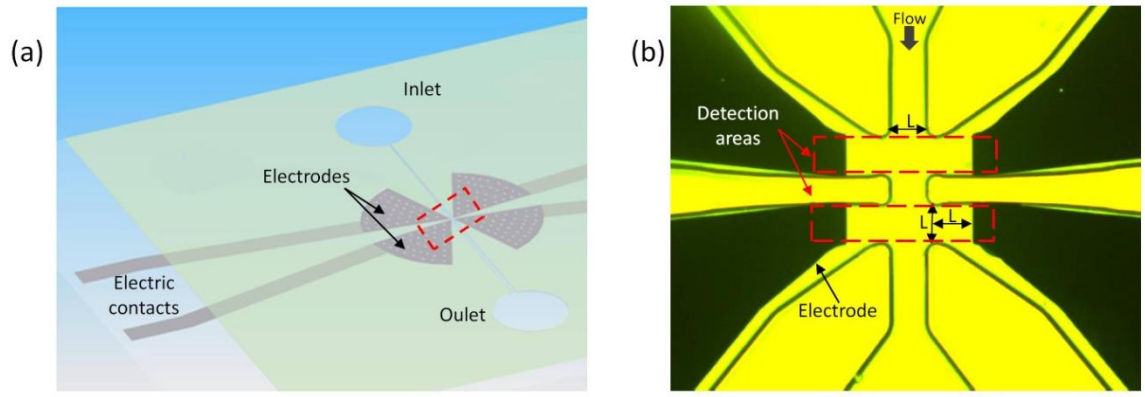

Figure 51: (a) View of the device for on-chip label-free multifrequency dielectric spectroscopy. Particles are dragged by the flow through the measurement volumes. (b) Detail photograph of the sensing area. The electrodes are patterned on the substrate and are recessed from the main vertical channel by L which is the characteristic dimension of the chip and is equal to 20µm.

The characteristic length of the device is set equal to 20µm in order to avoid clogging of particles with diameter varying from 10-15µm. Since the main channel section area is equal to 20µm x 20µm the chances to have more than one cell passing simultaneously are significantly reduced.

A benefit of the differential design, is the immunity to signal drift in contrast with absolute measurements. Another advantage of the liquid electrodes concept is that the metal electrodes can be kept out from the measurement channel and this allows to define large surface metal electrodes, which are very robust against eventual metal degradation. Moreover the electrodes are patterned in a single metal layer which simplifies the fabrication technology but act as two virtual equipotential electrodes patterned on the channel walls.

The measurements at lower frequencies with less influence from the electric double layer is made possible from the large area of the electrodes. In order to explain this effect we refer to the equivalent electrical circuit model described in section 2.4. Briefly, the capacitance of the double layer C_{DL} dominates the impedance at lower frequencies until the resistance of the solution between the electrodes R_{SOL} becomes larger than the impedance of this capacitor. The higher the capacitance, the lower the cut-off frequency which, with an electrical equivalent circuit approach, can be expressed as:

$$f_C \approx \frac{1}{2\pi R_{SOL} C_{DL}} \quad \textbf{[53]}$$

The design also features a simple fabrication process with only one metal layer, simplifying substantially the fabrication technology compared to other traditional designs (Gawad, Cheung, Seger, Bertsch, & Renaud, 2004).

The principal drawback of this design is the large detection volume due to the distance between the electrodes. Referring to the Schwan single shell model the conductivity of the mixture at low frequency is related to the electrolyte solution conductivity by the following equation defined in section 2.4 and reported here for convenience:

$$\sigma_{lf} = \sigma_{sol} \frac{1 - p}{1 + {}^{p}/_{2}}$$

where p is the volume fraction of the particle in the detection volume. This means that we should expect a smaller perturbation of the current flowing between the electrodes by the cell presence if the detection volume grows. In our case it grows by a factor of 3 due to the access channels compared to a hypothetical design with metal electrodes in place of our liquid electrodes.

5.4 Microfabrication

Float glass wafer with a thickness of 550µm is used for the substrate of the devices because of its high dielectric constant which extends the measurements frequency upper range limit. Moreover glass features an excellent optical transparency which is crucial during the experiments from a practical point of view. This is not a requirement for impedance measures, however, the use of transparent chips permits to cope with a number of issues during the experiments e.g. presence of air bubbles in the microchannel, impurities clogging the orifice etc.

The glass wafer is first Piranha bath cleaned (2min) in order to remove organic impurities. A layer of 200nm of platinum (Pt) over a 20nm thick titanium (Ti) used as an adhesion layer are deposited by evaporation on the float glass wafer. Patterning of the metal layer is performed by lift-off. Channels are designed on a second mask and are developed by photolithography of a coated 20µm SU-8 material. After that the wafer is diced in 20mm x 15mm chips.

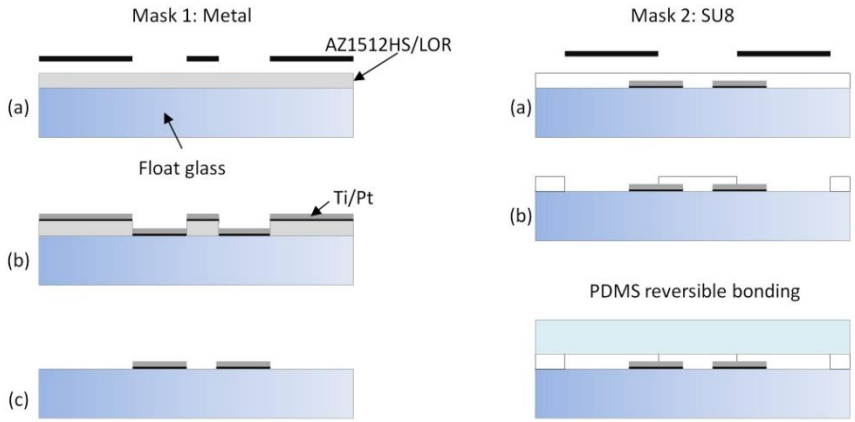

Figure 52. Microfabrication process. The Ti/Pt electrodes are evaporated and deposited by lift-off on a glass substrate before patterning of SU8. A PDMS block seals the channel from top and provides fluidic inlet and outlet.

Each device contains microfluidic channels that are opened from the top and then sealed with a PDMS block that provides inlets and outlets as well. Sealing is reversible and this permits to thoroughly clean the device from the top if clogging occurs.

Simple fabrication process permits to reduce the cost and time for chip prototyping. Furthermore, the reliability of the process is directly impacted by lowering the number of the fabrication steps. Another benefit of the selected design is the reusability of the chips because the microchannels are not sealed permanently and this permits a fast cleaning of the device.

5.5 Fluidic and electrical setup

The fluidic interface consists of a PDMS block which seals the channels from top under the pressure of a polycarbonate part. They are both mounted over the device which relies on the preamplifier PCB host. The PDMS block also includes the input and output reservoirs and is connected through the polycarbonate block to the positive pressure source (Braschler, et al., 2007) (Braschler, Demierre, Nascimento, Silva, Oliva, & Renaud, 2007). Mounting is preceded by an oxygen plasma treatment to ease channels filling with liquid.

The electrical setup comprises a preamplifier host board that supplies spring connectors for the platinum device pads, a current to voltage converter stage for each electrode couple composed of a trans-impedance amplifier and a differential amplifying output stage. An AC signal is sent to both couples of electrodes from an impedance spectroscope (HF2IS Zurich Instruments AG) for electrical impedance detection. The spectroscope mixes up to 8 different frequencies in the same output signal and simultaneously demodulates the same number of signals. It provides 8 demodulating units that permit to extract the in-phase and out-of-phase signals at each frequency of one of its two input signals. ADC sampling units and low pass filters necessary to complete the lock-in amplifier scheme are also present. Proprietary software is furnished with the instrument for data visualization and transferring to a computer in real time.

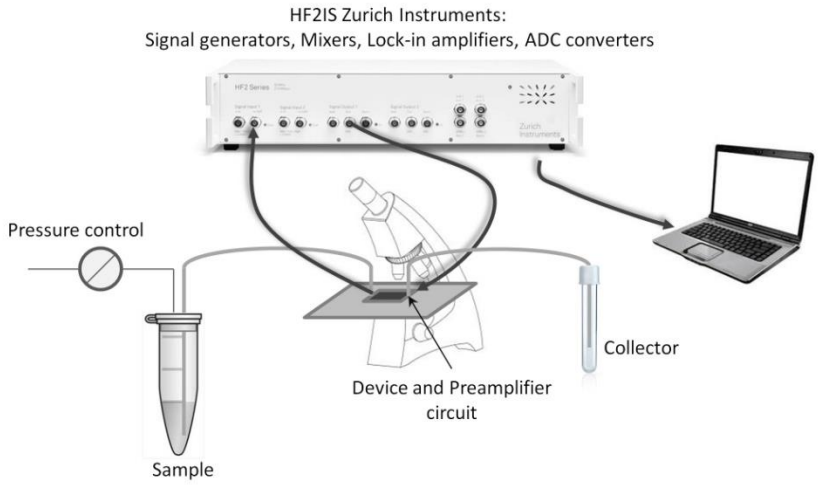

Figure 53. The measurement setup for impedance measurements of flowing particles

5.5.1 Preamplifier and demodulating scheme

The amplification system used in this project includes also a differential stage of auto-balanced bridges besides the lock-in amplification stage (HF2IS Zurich Instruments) which enables simultaneous measurements with multiple frequencies. The lock-in amplifier principle is described in section 2.5.

The host board where the chip is mounted provides also the preamplifier custom circuit described in (Gawad S. , 2004) whose block diagram is reported in Figure 54 and it involves a double channel I/V conversion stage, a differential amplifier and an output amplifying stage.

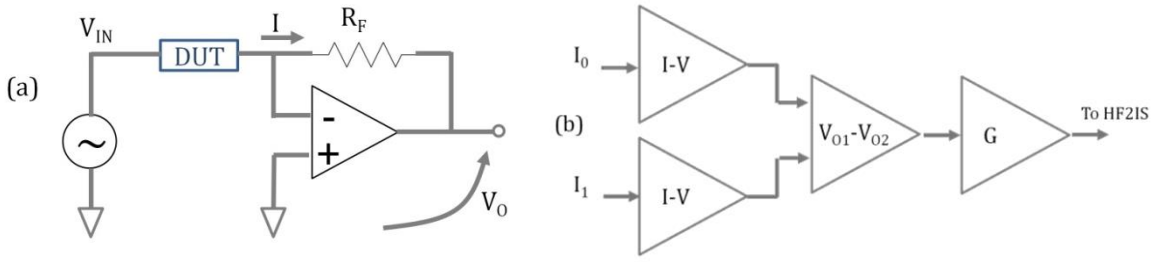

Figure 54. (a)Auto balanced bridge circuit and in (b) dual channel preamplifier block diagram

The auto-balanced bridge is found in most of the impedance analyzer instruments. The Opamp role in this circuit is to convert the current flowing through the feedback resistor into a voltage and to provide large bandwidth over several orders of impedance magnitudes with low input noise.

Multiple frequency sine waves are summed and applied to the sensor electrodes from the HF2IS output. The output of the preamplifier board is sent back to the demodulators of the HF2IS to retrieve the signal (in phase and out of phase) and the demodulated cell signals are sent to the computer.

The output signal is essentially a DC voltage whose value in time depends on the current difference between the two electrode couples.

5.6 Analytical and numerical modeling of liquid electrodes in 2D geometry

In order to evaluate the sensitivity of the sensor, the electrical field distribution within the microchannel has to be known. Several previous works have evidenced the possibility of calculating an analytical expression for the field distribution (Linderholm & Renaud, 2005) (Linderholm, Seger, & Renaud, 2006) .

In this study we preferred the numerical approach to the analytical one for the sensor characterization. The morphology of the electrodes and the fact that the field is generated by planar electrodes in a three dimensional structure complicate the analytical expression of the electrical field and require several successive conformal mapping steps. However, to prove the validity of our numerical model we calculate the analytical expression for the electrical field distribution of the simple geometry shown in Figure 55. Comparison with numerical results will be shown and the assumption that the liquid electrodes can be considered as equipotential surfaces will be also discussed.

We need to determine the cell constant which is a parameter defined by the geometry of the sensor. It describes the dependence between the resistivity of the medium filling the microchannel and the measured resistance. In (Olthuis, Streekstra, & Bergveld, 1995) it is defined as:

$$\kappa = \frac{R}{\rho}, \text{and since } RC = \frac{\varepsilon_0 \varepsilon_r}{\sigma} \Rightarrow \kappa = \frac{\varepsilon_0 \varepsilon_r}{C}$$

where R is the resistance, $\rho=1/\sigma$ is the resistivity and C is the capacitance between the electrodes. Therefore if the capacitance C is known, the expression for κ can be determined.

First, we make a series of geometrical transformations to easily find the expression for the potential distribution within the structure. We will transform a two dimensional cross-section with electrodes in the bottom wall of the geometry in Figure 55 into a cross-section where the electrodes are parallel with a uniform electric field distribution.

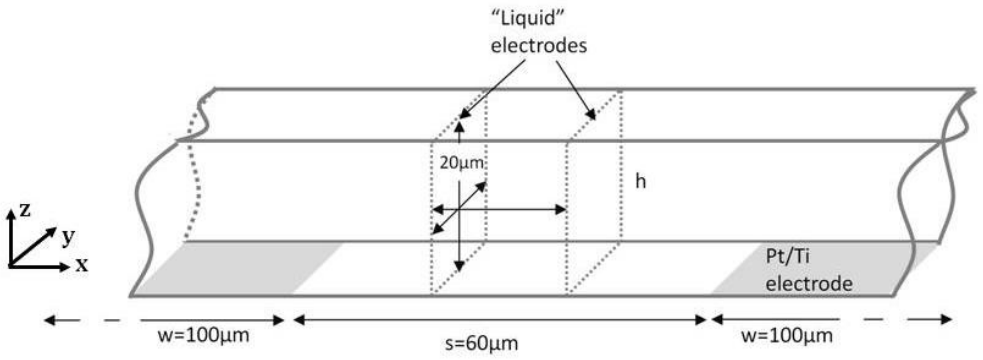

Figure 55. Scheme of the microstructure to compare the analytical and the numerical expression of the electric field. The channel is supposed to have infinite width and each of the electrodes is 100μm.

Having assumed that the width of the structure is infinite we can model as a rectangle the length-wise cross section of the microchannel with the electrodes on the substrate. Since this 2D geometry is symmetrical it can be simplified with its half by placing a conductor in correspondence to the symmetry line as in Figure 56.a (Linderholm & Renaud, 2005). The potential of the electrode in the symmetry line is equal to half of the difference between the two starting planar electrodes. Also, a multiplication with a factor of two is required in the end when the electric field is calculated.

The geometry of the real microchannel defined in the Z-plane with coordinates $z=x+iy$ is defined by the points $z_1=h/2$, $z_2=-h/2$, $z_3=-h/2+is/2$ and $z_4=-h/2+i(s/2+w)$ where h and s were defined in Figure 55. Using a sine transformation of the Z plane the rectangle is

transformed in a half plane with the electrodes along the bottom wall as shown in Figure 56.b. The bilinear transformation is made to in order to equalize the electrodes' length thus permitting to pass in the V-plane:

$$v = \frac{u + B}{Cu + D} \qquad \textbf{[54]}$$

After imposing that v_3=-v_2=*1* the following set of equations is obtained:

$$\frac{u_1 + B}{Cu_1 + D} = -\frac{u_4 + B}{Cu_4 + D}, \qquad \frac{u_2 + B}{Cu_2 + D} = -1, \qquad \frac{u_3 + B}{Cu_3 + D} = 1 \qquad \textbf{[55]}$$

After solving the set of equations for B, C and D we get the expression for v_4*:*

$$v_4 = \frac{(u_3 - u_2)(u_4 - u_1)}{u_4(u_3 + u_2 - 2u_1) + 2\sqrt{(u_4 - u_3)(u_4 - u_2)(u_3 - u_1)(u_2 - u_1)} + u_1u_2 + u_3(-2u_2 + u_1)} \qquad \textbf{[56]}$$

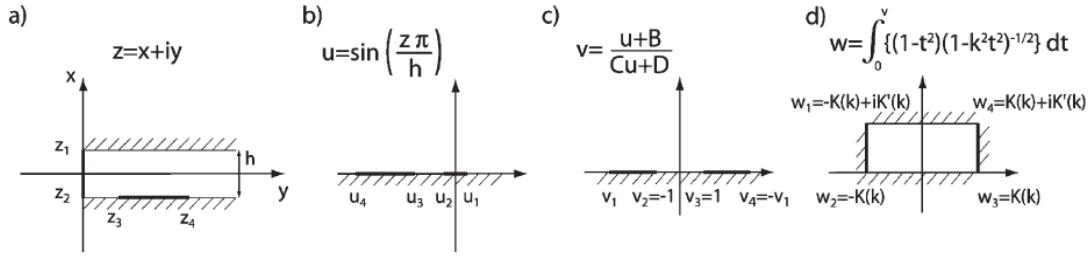

Figure 56. (a)Cross-section of half of the microchannel. To use the SC transform the sine transformation is performed in (b) to place the electrodes in the real axis of the U-plane. In (c) the result of the bilinear transformation that equalizes the electrode length and imposes symmetry with respect to the origin. (d) Schwartz-Christoffel mapping to obtain a parallel plate measurement cell in which the potential distribution and resistance can easily be calculated.

The Schwartz-Christoffel (SC) conformal mapping is now possible and defined; in Figure 56.d the final coordinates are shown. *K(k)* is the elliptic integral of first order that can be

calculated with Matlab or another software package. The modulus *k* of the integral is equal to:

$$k_{\mu channel} = \frac{1}{v_4} \quad \textbf{[57]}$$

in our case and the final expression for the cell constant as defined in (Olthuis, Streekstra, & Bergveld, 1995) considering the full geometry in Figure 55 is:

$$\kappa_{\mu channel} = 4\frac{K(k)}{K(k')} \quad \textbf{[58]}$$

with $k' = \sqrt{(1-k^2)}$. The set of equations were implemented in a Matlab script and the complete elliptic integral of first kind was calculated by a built-in function[5]. In Figure 57 the norm of the electric field is presented for this structure in correspondence to a longitudinal cross-section of the microchannel confined by the liquid electrodes.

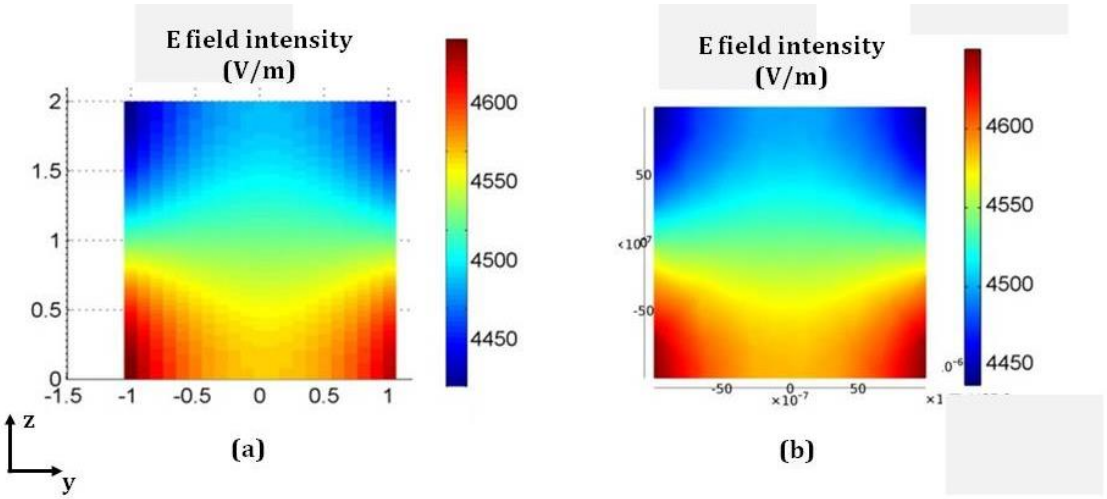

Figure 57. Comparison between the analytical expression (a) of the electrical field calculated via conformal mapping and the two-dimensional numerical finite elements simulation with Comsol multiphysics(b). Visualized slices are in correspondence to the central part of the structure (parallel with the text plane) and perpendicular with the liquid electrodes.

5.7 Numerical modeling of the sensing area

From now on, a three dimensional FEM model implemented in Comsol Multiphysics is used to determine the electric field distribution. The measurement channel along x and the trapezoidal dead end chambers containing the electrodes are added as shown in Figure 58.

[5] The Matlab built-in function is *ellipke.m*

The trapezoidal subdomains are connected to the measurement channel by the access channels which are 20µm long. The CAD model was designed with the SolidWorks software and simulated using Comsol Livelink interface. The electrodes are situated in the bottom plane confined by the trapezoidal frames.

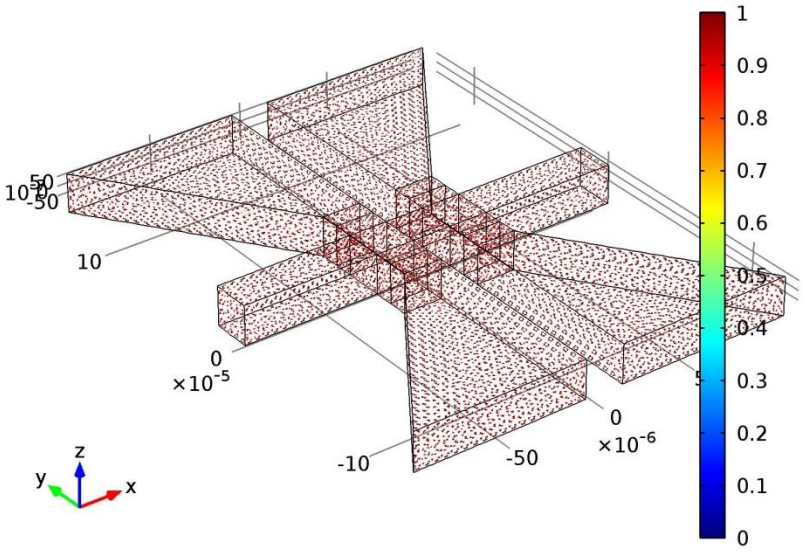

Figure 58. Geometry and mesh used to solve the potential distribution within the sensing area visualized in Figure 51.The number of elements for the mesh was 62357. For better visualization mesh elements were shrank with a factor 0.3. The color bar represents the mesh quality which is quite acceptable in all subdomains.

The objective of the simulation is to calculate the electric field distribution for determining the uniformity of the field in the main channel in order to evaluate the sensitivity of the device. The field perturbation due to the presence of the particle with spherical shape (single shell model) is also predicted.

A sine wave with amplitude $V_{pp} = 0.35\ V$ and in the frequency range typically from 10^5 to 10^7 was applied to the excitation electrodes. The suspension fluid electrical conductivity σ was 1.5S/m according to the pure PBS buffer suspension used during the experiments. In Figure 59.a the arrows represent the current density flowing from the excitation electrodes to the measurement electrodes. The electrical field lines are conveyed through the access channels and the fringing effect is noticeable in correspondence to the main channel opening corners.

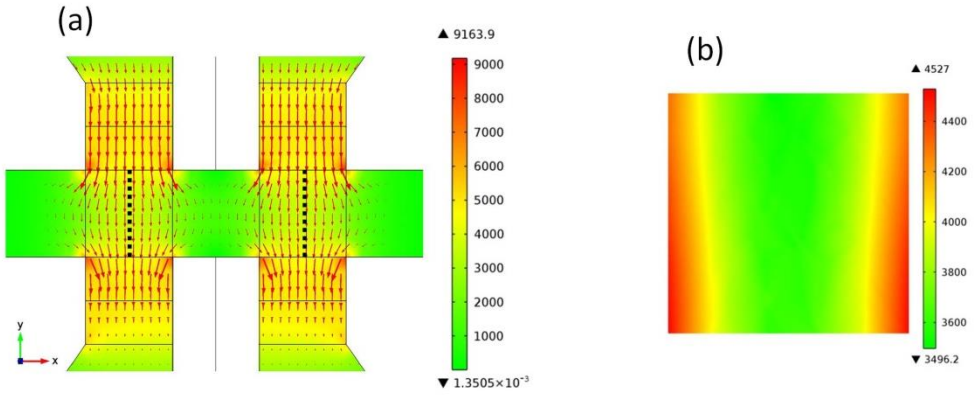

Figure 59. Top view of the electric field and current distribution (a). The electric field slice in (b) was obtained from the vertical dashed line in (a) in order to compare the field uniformity in the measurement channel.

If we compare Figure 59.b with Figure 57 a difference of the field distribution can be noticed. The presence of the main channel permits the current to flow following the lines shown in Figure 59.a. This helps to uniform the field intensity along the z direction but, on the other hand, the difference between the maximum and minimum of the field norm is increased in this new structure resulting in a coefficient of variation defined as the ratio of the standard deviation value and the average *CV=3.2%* for the structure without the measurement channel in Figure 57 against *CV=18%* for the geometry displayed in Figure 59. Obviously this directly impacts on the sensor sensitivity and it is necessary a deep and clear understanding of the phenomenon in order to characterize the sensor.

A particle flowing in these lateral positions would perturb more the current distribution than a particle flowing in the middle. It is clear that the differential measured current will depend on the particle distance from the access channels in the y direction. In the next section this point will be studied more in detail. A single shell model for a spherical shell will be used to determine the sensitivity of the device.

5.8 Modeling of single particles in suspension

The internal structure of biological material consists of several interfaces and components. When we try to model a single shell cell i.e. a spherical domain surrounded by a thin membrane the simulation gets immediately problematic due to large geometry ratios. The wall thickness is very small compared to the particle radius - 5nm and 5µm respectively. For accurate solving and efficient geometry definition the Maxwell Mixture Theory (MMT) is used; it permits to transform by analytical calculation the single shell model into a geometrically homogeneous cell with equivalent permittivity and conductivity. These parameters are frequency-dependent for the effective 0-shell model.

MMT has been used in several works to give an elegant description of the dielectric properties of the mixture in low volume fraction cases between particles and suspension fluid. For a single shell spherical cell the equivalent complex permittivity of the solution can be expressed as (Eqn. [32]):

$$\tilde{\varepsilon}_{mix} = \tilde{\varepsilon}_m \frac{1 + 2\varphi \tilde{f}_{CM}}{1 - \varphi \tilde{f}_{CM}}$$

where $\tilde{\varepsilon}_{mix}$, $\tilde{\varepsilon}_m$ are the complex permittivity for the mixture and the medium respectively. φ is the volume fraction of the particle and the detection volume between the electrodes while $\tilde{f}_{CM}$ is the complex Clausius-Mossoti factor and was defined in section 2.3.1 as :

$$f_{cm}(\omega) = \frac{\tilde{\varepsilon}_p - \tilde{\varepsilon}_m}{\tilde{\varepsilon}_p + 2\tilde{\varepsilon}_m}$$

We report here again the complex permittivity of a spherical particle with radius *R* and membrane thickness *d*:

$$\tilde{\varepsilon}_p = \tilde{\varepsilon}_{mem} \frac{\gamma^3 + 2\left(\frac{\tilde{\varepsilon}_c - \tilde{\varepsilon}_{mem}}{\tilde{\varepsilon}_c + 2\tilde{\varepsilon}_{mem}}\right)}{\gamma^3 - \left(\frac{\tilde{\varepsilon}_c - \tilde{\varepsilon}_{mem}}{\tilde{\varepsilon}_c + 2\tilde{\varepsilon}_{mem}}\right)}$$

being $\gamma = R/R - d$ and $\tilde{\varepsilon}_{mem}, \tilde{\varepsilon}_c$ the complex permittivity of the cell membrane and cell cytoplasm respectively. Since the total measurement volume is approximately equal to 60µm x 20µm x 20µm = 24pL and the volume of a cell with radius 5µm is nearly equal to 0.5pL, in the presented cytometer the volume fraction fulfills the necessary condition $\varphi << 1$ for the Maxwell mixture theory to hold. By separating the real and the imaginary part of Eqn. [29] reported above, we get the values of permittivity and conductivity for the FEM model. Now the numerical problem is ready to be solved. This approach is obviously valid also for modeling polystyrene beads by using the same values of σ and ε in both membrane and internal parts of the particle. In Table 7 the list of parameters used for the simulations is reported. Unless differently specified, all measurements were performed in PBS at room temperature with σ≈1.5S/m and pH=7.4. For applications involving the use of biological cells, the PBS solution is supplemented with 0.1% (*w/w*) of bovine serum albumin (BSA) to reduce cell adhesion to the channel walls.

Table 7. Shell model parameters used in FEM simulations (Morgan & Green, 2002)

Parameters	Bead	HeLa cell
$\boldsymbol{\sigma}_{\text{medium}}$ [S/m]	1.5	1.5
$\boldsymbol{\sigma}_{\text{membrane}}$	1e-8	1e-6
$\boldsymbol{\sigma}_{\text{cytosol}}$	-	0.5
$\boldsymbol{\varepsilon}_{\text{medium}}$ [1]	78	78
$\boldsymbol{\varepsilon}_{\text{membrane}}$	2.54	2.5
$\boldsymbol{\varepsilon}_{\text{cytosol}}$	-	60
R [m]	4e-6	5e-6
d	-	5e-9

The dependence on the frequency of the single shell particle dielectric properties is illustrated in Figure 60 where the green arrows are proportional to the current density whilst the grayscale map represents the electric field. At low frequency the particles' internal domain is minimally crossed from the current arrows. In this case, the induced polarization field is clearly visible on the particle's sides. At 15MHz more current flows

through the particle. The integral of the current on the right boundary contains information on the cell size for the former and on the cytosol properties and cell size also for the latter.

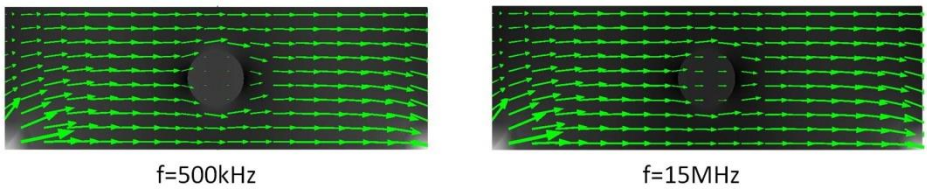

Figure 60. Low and high frequency current density distribution (arrows).

The principal advantage of FEM is that the position of the particle can be easily varied in order to obtain the impedance variation as the cell flows into the cytometer. If we refer to the geometry presented in Figure 61, X position is varied with a 5µm step along the microchannel and this simulation is repeated for three different Y positions. The obtained differential current values are reported in Figure 61. The dependence from the y coordinate of the pulse peak to peak amplitude is clearly revealed.

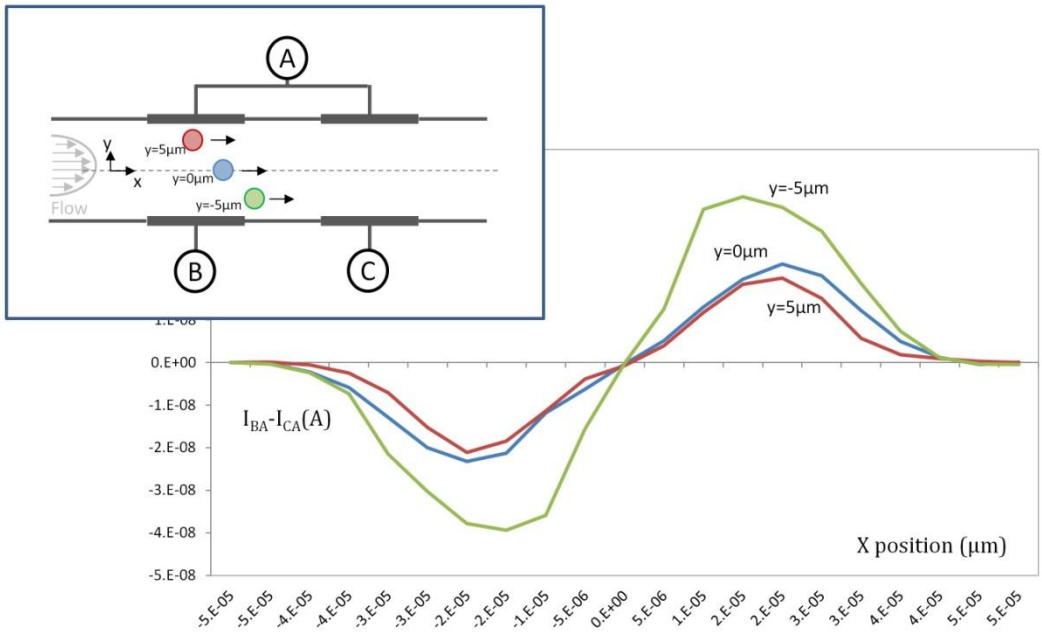

Figure 61. Beads flowing along the microchannel with X coordinate parameterized. To assess random position effects also Y is varied from the measurement to the excitation side.

It can be seen that the highest signal corresponds to the measurements' side (y<0) and the reason of asymmetry will be explained below. This aspect is very important because it prevents us from using the device for particle size measurements.

In order to investigate the dependence of the signal from the particle radius we varied its position in the y direction between -10μm and 10μm; these are the borders of the liquid electrodes. The differential value between the two sensing electrodes multiplied by the amplification stages is visualized in Figure 62. It can be observed that the maximum values are different in correspondence to different radius particles but in a real case with a mixture of particles of different sizes flowing in random y positions the projection of the amplitudes in the y axis will be certainly overlapped for different size populations.

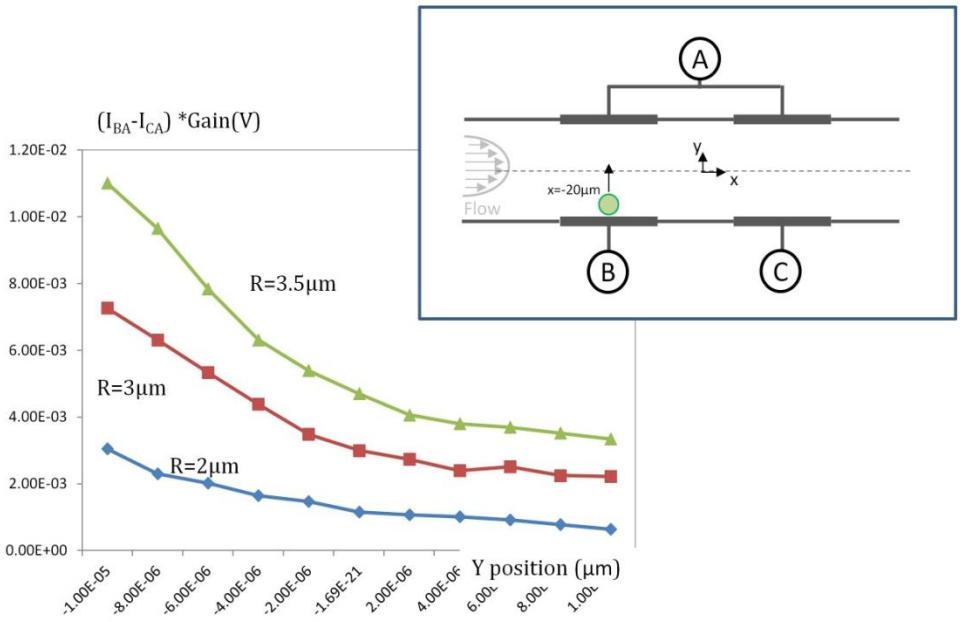

Figure 62. Differential current between the electrode couples when a particle Y position is varied between the AB electrodes pair. The radius of the particle is also parameterized to predict size based discrimination issues.

The origin of this asymmetry can be understood from the charts in Figure 63. Let us name A_1 and A_2 the left and the right excitation electrodes in Figure 62 respectively. On the left of Figure 63, the current values that enter in electrode C are shown and the *d* parameter is the distance between the A_1B and A_2C couples. The X axis indicates one more time the position of the bead between the A_1B couple with parametric Y position.

The modulus of the current that enters in C seems to vary with the bead moving between A_1 and B. This means that there is some cross coupling current between A_1 and C as well. Keeping the electrode couples far from each other helps to minimize the coupling effect as

it can be seen in the left chart where minimal variation is achieved when the electrodes are 160µm apart. This is confirmed also by the improved symmetry of the difference A_1B and A_2C in the chart on the right for d=80 and 160µm compared to the asymmetrical trend for d=20 and 40µm.

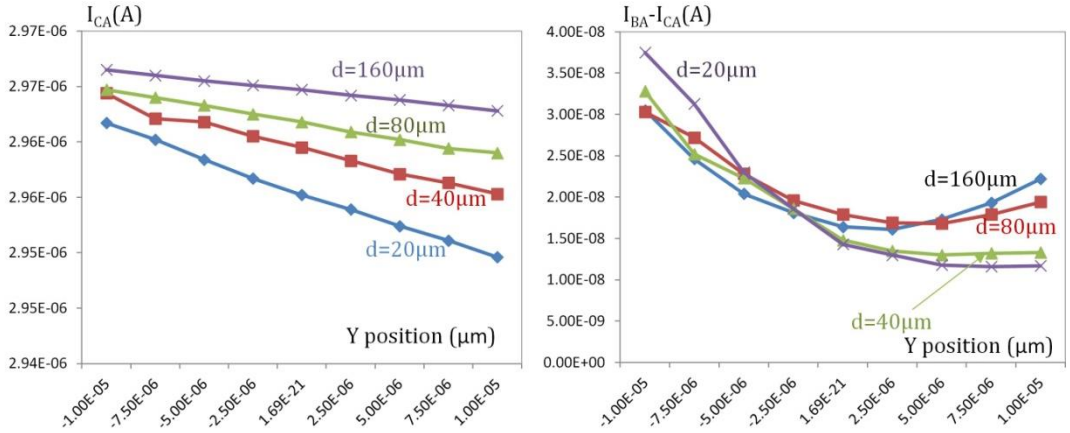

Figure 63. Cross-talk current between the electrode couples A_1B and A_2B. The current of the latter is shown on the left depending on the particle T position between the first couple. Differential current visualized on the right chart.

5.9 Experimental

5.9.1 Tests with polystyrene microbeads

Since the simulated measured signal amplitude dispersion along Y is relevant (Figure 62) and the cell size is also variable, we decided to perform some tests with microbeads. The data dispersion was evaluated with size-calibrated beads with diameter of 4, 6 and 7 µm. The populations were measured separately. The chip does not include any particle focusing structure and the first result that we achieve when we look at the histograms in Figure 64 is that the discrimination of differently sized beads is very difficult. All the histograms are overlapped and except for the mean value, no other useful information can be obtained in order to discriminate between the different populations of microbeads. The data were obtained from almost one thousand events for each case and the frequency corresponding to the shown data was equal to 500 kHz. 2-samples moving average was used for interpolation for better visualization. The measurements were performed with beads suspended in phosphate buffered saline at room temperature.

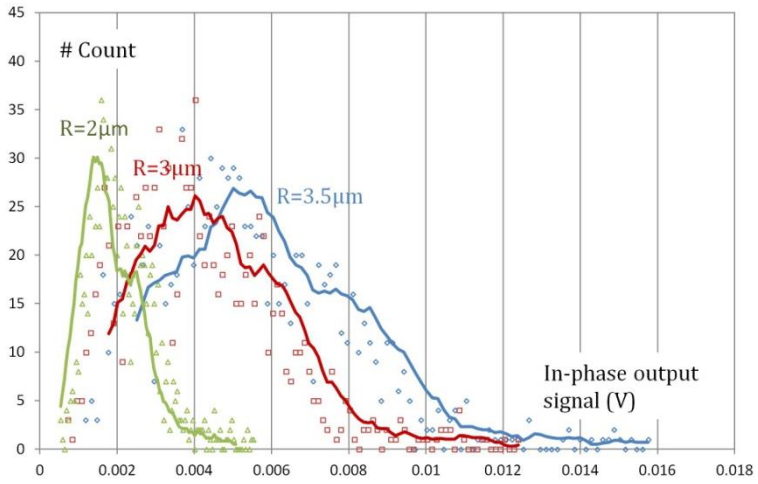

Figure 64. Differentiation of size calibrated 4,6 and 7µm beads.

We expected from simulations that it would have been difficult to differentiate particles based on their size. However, the objective of this work is to monitor the dielectric properties of cells when exposed to pore-forming toxins. In case of variation of these internal properties the ratio between high and low frequency signal amplitudes helps to

partial outsize the position dependence. Experiments with cells are introduced in the next section.

5.9.2 HeLa cells

The aim of this section is to demonstrate that the system can differentiate cells depending on their dielectric properties. HeLa (Human epithelial carcinoma) cells were incubated at 37°C in HBSS. Cells were removed from culture by trypsinisation and suspended PBS to a concentration of 10^6cells/mL before experiments. Priming of the chip with PBS was performed prior to use and a sample of suspended cells was injected applying a positive pressure to the inlet reservoir of 50-80mBar. This ensures a transit time for particles from 6 to 10ms. The transit time can be determined by subtracting the instants corresponding to the high and low peaks of the measured signals (see Figure 50). Assuming that the particles velocity is nearly constant, we can measure it by dividing the transit time with the electrodes' distance which is 40μm.

The measurements' frequencies were experimentally chosen equal to 500 kHz (LF) and 15 MHz (HF) and the amplitude of the excitation signal was equal to $0.35V_{pp}$. Cells are expected to differ substantially from beads in the β-dispersion range and above. Furthermore, a comparison between beads and cells is made in terms of electrical opacity which is defined as the high frequency to the low frequency signal ratio. This value is obtained after processing the acquired data.

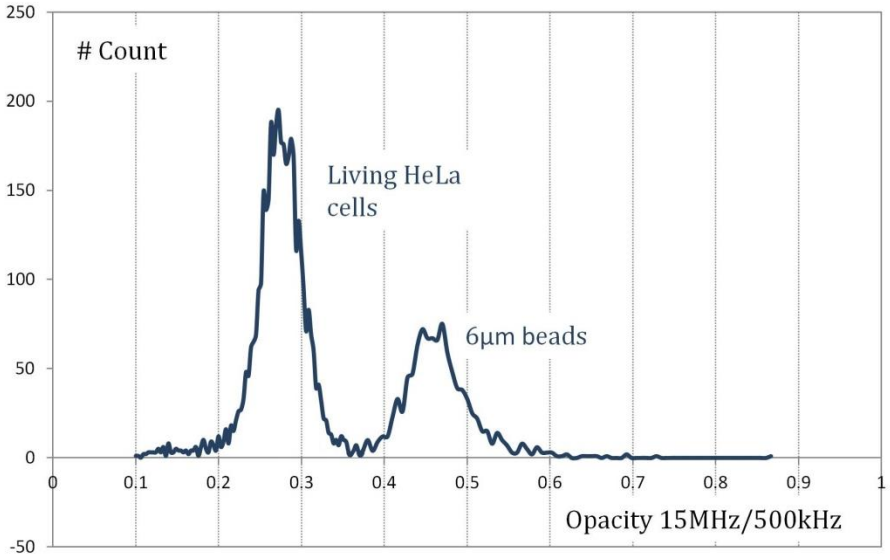

Figure 65. Histogram of the opacity of a mixture of beads and cells measured with the flow cytometer.

The scattering observed for the signals at 500kHz in Figure 64 is now eliminated by the division of the HF and LF signal amplitudes. The average opacity is 0.28 with dispersion σ close to 0.024 for cells. The opacity of beads is nearly 0.46 with dispersion 0.038. The values state that the HF peak to peak amplitude signal for beads is nearly half the LF amplitude while for cells it is about one forth.

The experiments with beads and living cells were performed to test the frequency response of the system and its sensitivity, and were also useful to determine the optimal values for experimental parameters such as positive pressure to apply at the inlet and filter settings at the demodulator output. HF and LF frequency values that greatly impact on the system performance were experimentally calculated as well.

Successively, dynamic changes of HeLa cells dielectric properties were induced by exposing the cells to a pore-forming toxin named Listeriolysin-O (LLO) and measurements were performed to track these variations in time.

5.9.3 Listeriolysin O: The cholesterol-dependent cytolysin of Listeria monocytogenes

5.9.3.1 Introduction

Cholesterol-dependent cytolysins represent a large family of pore forming toxins produced by several bacteria such as Listeria monocytogenes. The pore forming toxin is a secreted protein that can inflict plasma membrane damages to an exposed cell. Being this an ancient form of attack, cells have evolved defense mechanisms to deal with these injuries. Several response pathways are triggered with the aim to restore the plasma membrane integrity and ion homeostasis (Gonzalez, Bischofberger, Freche, Ho, Parton, & Van der Goot, 2011). Furthermore, cells under attack enter a quiescent-like state. They minimize energy consumption by arresting protein synthesis and activating energy storage in lipid droplets while waiting for the membrane to be resealed.

LLO is a soluble pore forming protein secreted by the pathogen bacteria in the extracellular environment. It can be added to the cell suspension sample to successively investigate its effects on the cell population. Exposure to high doses of PFTs leads to apoptotic (Nelson, Robert, & Buckley, 1999) or necrotic (Kennedy, Smith, Lyras, Chakravorty, & Rood, 2009) cell death. More recently, it has been observed that in case of sublytic doses cells can respond to the attack by triggering defense mechanisms and possibly even warning other cells of the aggression (Gonzalez, Bischofberger, Freche, Ho, Parton, & Van der Goot, 2011). Generally speaking, the morphology of the pores created in the plasma membrane is very different depending on the type of toxin present in the extracellular medium but in the case of LLO these pores are formed from about 50 monomers. Their dimension reaches 30nm (Gilbert, 2010).

Taking a cue from the recent study of (Gonzalez, Bischofberger, Freche, Ho, Parton, & Van der Goot, 2011) we wanted to measure eventual changes of the dielectric properties of HeLa cells when exposed to LLO insult.

Since the membrane repair process requires about 2 hours for LLO attack (Gonzalez, Bischofberger, Freche, Ho, Parton, & Van der Goot, 2011) we wondered whether during that period of time there was any significant information that could be obtained in order to describe cell membrane repair with our cytometer.

From an applicative point of view, the reversible permeabilization for the delivery of proteins into living cells through the pores formed on the plasma membrane is very interesting. Protocols can be found in literature attesting that reversible membrane permeabilization requires low doses of toxin to achieve the target goal, for example: permeabilization of 60-80% of cells (Walev, Bhakdi, Hofman, Djonder, Valeva, & Aktories, 2001). The correct dose is also dependent from the cell target type and their density. The impedance flow cytometer here presented is an alternative to traditional FACS for fast and efficient titration of the concentration of LLO.

5.9.3.2 Impedimetric measures of cells continuously exposure to LLO

After the basic experimental steps with very different particles in terms of dielectric parameters such as HeLa cells and polystyrene beads, the response of HeLa cells to the presence of LLO was analyzed.

Adherent HeLa cells were incubated in six-well plates and the cultures were split every three or four days by trypsinisation to maintain growth. For experimental purposes cells were suspended in PBS and were exposed to several concentrations of LLO toxin (from 100 to 500ng/mL). After 10 min at 37°C cells were resuspended in HBSS. Each well content was trypsinised periodically every 20 min. for impedance measurements. The content of all wells was measured within the next two hours from the first sampling.

Staining with propidium iodide (PI) was performed to assess the permeabilization due to the bacterial toxin presence (Figure 66). PI is a membrane-impermeant dye commonly used to asses DNA content.

Initially, trypsinised HeLa cells (suspension) were exposed to LLO with concentration equal to 500ng/mL. The toxin was present in the suspension medium for all the experiment duration. The cells' impedance was measured every 10 min after LLO introduction.

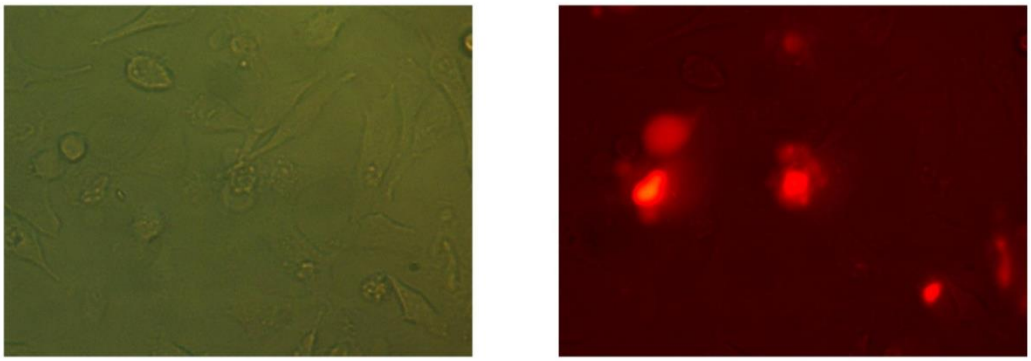

Figure 66. (a)Bright field view of HeLa cells magnified 40x. (b)Propidium iodide (PI) staining was performed to verify that LLO could exert membrane permeabilization.

The measured signal modulus is indicated in Figure 67. We point out one more time the advantage of using impedance spectroscopy that permits to measure the real and imaginary part of the measured signal from which the modulus and the phase can be calculated as shown in the Lock-in section. Each measurement point corresponds to an average of more than 500 cells pulse shaped signal. It can be seen that as a result of the toxin effect, the amplitude of the modulus increases at all frequencies.

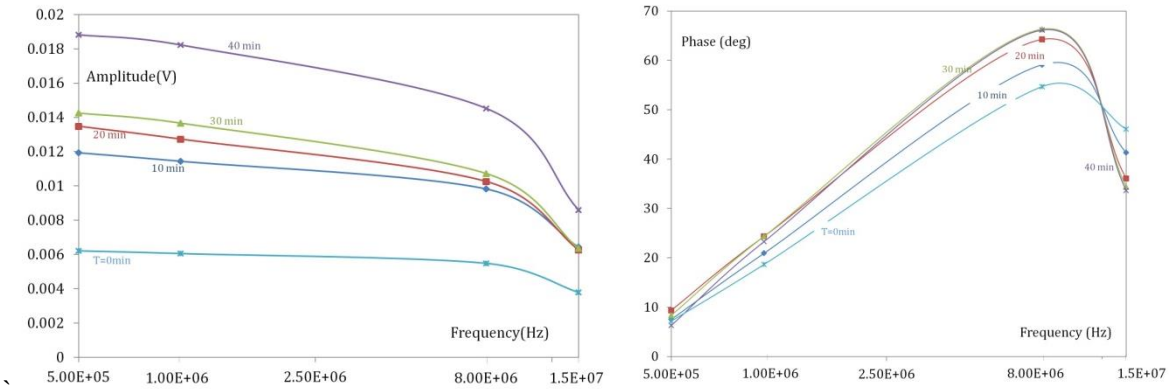

Figure 67. Measured amplitude of HeLa cells when continuously exposed to LLO at 500ng/mL.

This effect is immediately observed at low frequencies and it is clearly visible also for the 40min. curve at HF.

The impossibility to perform particle sizing mentioned in the beginning of the experimental section prevents us from extracting much more information from the signal amplitude at various frequencies other than its average. The dependence of the

measurement from the horizontal position of the particle in the microchannel generates some scattering noise. This signal dispersion is more emphasized for cells because the size variation of the cell diameter contributes together with the horizontal position effect. However, taking the ratio of the HF signal to the LF signal nullifies these effects. The size variation contribute is eliminated because the extracellular current is the same at both frequencies. We also make implicitly the assumption that the position of the cell along the Y direction is the same for both electrodes pairs. The constancy of the position in Y for a microfluidic channel which is characterized by laminar flow is always guaranteed and this is verified by the symmetry with respect to the X axis of the pulse shape signal due to a flowing cell.

The phase defined in Eqn. [39] undergoes great amplitude variation at high frequencies. Experimental evidence showed that the opacity between the 15 MHz and the 500kHz signals is a good parameter for monitoring the physiological/morphological changes in cell under LLO attack. Compared to the phase at 8MHz the opacity defined above, presents a clearer separation between the two cells' subpopulations.

In the histograms in Figure 68 the opacity (500kHz/15MHz) of the signals is visualized for the measurements at 0, 10, 20, 30 and 40 min.

The first measurement is performed before the toxin introduction. It can be noticed an immediate shifting to smaller values of opacity for most of the cells. Yet, a population equal to that of the first measurement in terms of opacity continues to be present. This fact is in line with other studies (Gonzalez, Bischofberger, Freche, Ho, Parton, & Van der Goot, 2011) that evidence the presence of a certain percentage of cells depending on the toxin concentration which is immune to the attack.

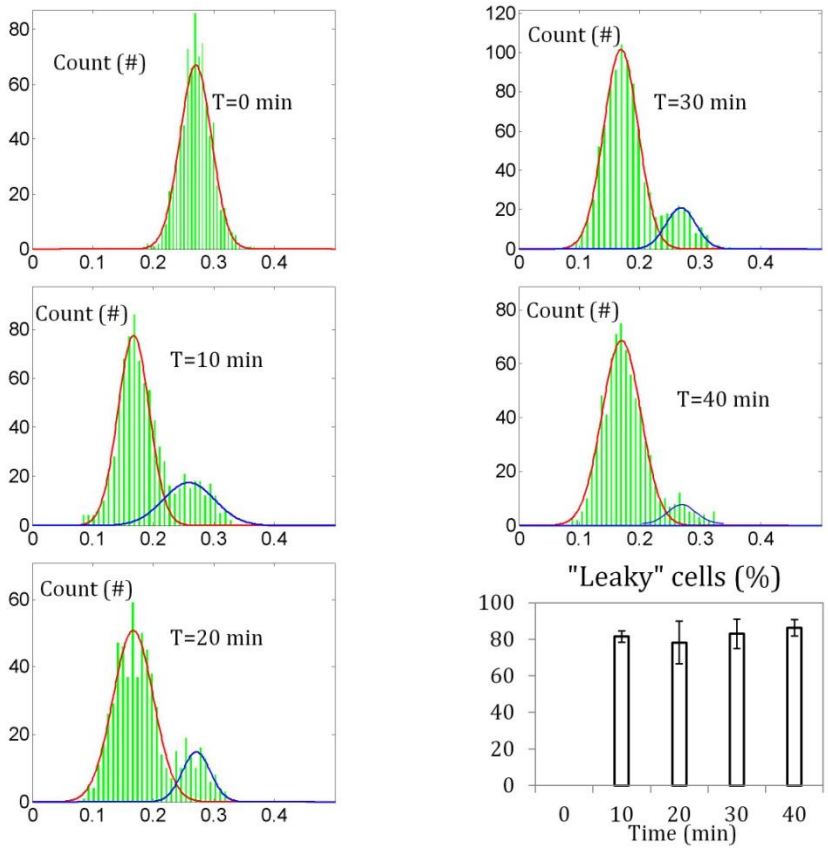

Figure 68. Opacity histograms (15MHz/500kHz) corresponding to the amplitudes in Figure 67. Intact cells have higher opacity.

In the last chart the ratio of the damaged cells is plotted over time. A possible explanation of the fact that at t=20min the dead cells number is lower can be the smaller number of samples obtained from this experiment compared to t=10min as shown in Table 8. Histogram data were fitted with a Matlab script in order to obtain the average, amplitude and standard deviation for each subpopulation. The Gaussian fitting parameters are shown in Table 8.

To calculate the fitting parameters, a second order Gaussian fitting model was used, obtaining a set of parameters of the form:

$$f(a_1, b_1, c_1, a_2, b_2, c_2, x) = a_1 \cdot exp(-((x-b)/c_1)^2) + a_2 \cdot exp(-((x-b_2)/c_2)^2) \quad \textbf{[59]}$$

where a_1, a_2 are the amplitudes of the curves, b_1, b_2 are the averages and c_1, c_2 are the standard deviations of the bell shaped distributions. The first histogram was fitted with a first order Gaussian model. For determining the ratio of the "leaky" cells (lower opacity) the amplitudes' ratio $a_1/(a_1+a_2)$ was used since for a normal distribution with mean μ and variance σ^2 as the following:

$$f(x) = \frac{1}{\sigma\sqrt{2\pi}} e^{-\left(\frac{(x-\mu)}{\sqrt{2}\sigma}\right)^2} \quad \textbf{[60]}$$

it is true that:

$$\int_{-\infty}^{\infty} f(x) = 1 \quad \textbf{[61]}$$

This renders the area confined by the density curves equal to the amplitude.

The results shown in Figure 68 were very encouraging; it showed that the cytometer could detect cells' physiological and/or morphological changes. However, after 40 min no contrast phenomenon that would suggest cell recovery was noticed. This experiment was reproduced several times with similar results. No resealing of cells was encountered even with lower concentrations of continuously delivered toxin.

Table 8. Fitting parameters

Time(min.)	0	10	20	30	40
Samples #	722	815	629	911	732
$\boldsymbol{\mu}_1$	-	0.17	0.17	0.17	0.17
$\boldsymbol{\mu}_2$	0.27	0,26	0.27	0.27	0.25
$\boldsymbol{\sigma}_1$	-	0.06	0.033	0.035	0.028
$\boldsymbol{\sigma}_2$	0.037	0.037	0.047	0.04	0.045
A_1	67.1	77.4	50.8	101.4	68.7
A_2	-	17.5	14.8	20.9	7.1
Intact cells (%)	100	81.6	77.4	82.9	90.6
Leaky cells (%)	0	18.4	22.6	17.1	9.4

5.9.3.3 Measurements with pulsed exposure to LLO

The approach we decided to follow was to remove LLO from the medium 10 minutes after its introduction to try to accelerate the cell recovery process (Gonzalez, Bischofberger, Freche, Ho, Parton, & Van der Goot, 2011), (Walev, Bhakdi, Hofman, Djonder, Valeva, & Aktories, 2001).

In all the subsequent experiments, the followed procedure consisted in 10 min exposure pulses of LLO. Cells were suspended in six-well plates. Two plates were used for each experiment: the first for the untreated control sample measurement and the second for the toxin effect probing. Toxin was added at given concentrations and after 10 min it was removed from all wells. Cells were trypsinised afterwards (4 minutes) one well at a time every 20 minutes and impedance measurements followed (2 minutes).

Compared to the measurements summarized in Table 8, the substantial difference lies in the fact that the cells' exposure to LLO is finite in time; after 10 min. the toxin is removed thoroughly via PBS washing of adherent cells. Since the medium removal is much easier with adherent cells (no need to centrifuge), HeLa cells were left in adhesion at 37℃, 5% $CO_{2,}$ during all the experiment until the impedance measurement moment which was preceded by trypsinisation. The experiment was reproduced two times for each control (data acquired from untreated cells over time at selected frequencies); pulsed LLO and continuous LLO curve. t=0 minutes corresponds to the control measure before adding the toxin. Measurements were performed at t=0, 20, 30, 50, 70, 90, 110 min approximately.

As an example, a scatter plot for 4156 data points corresponding to the control measurement at t=70min. is shown in Figure 69.

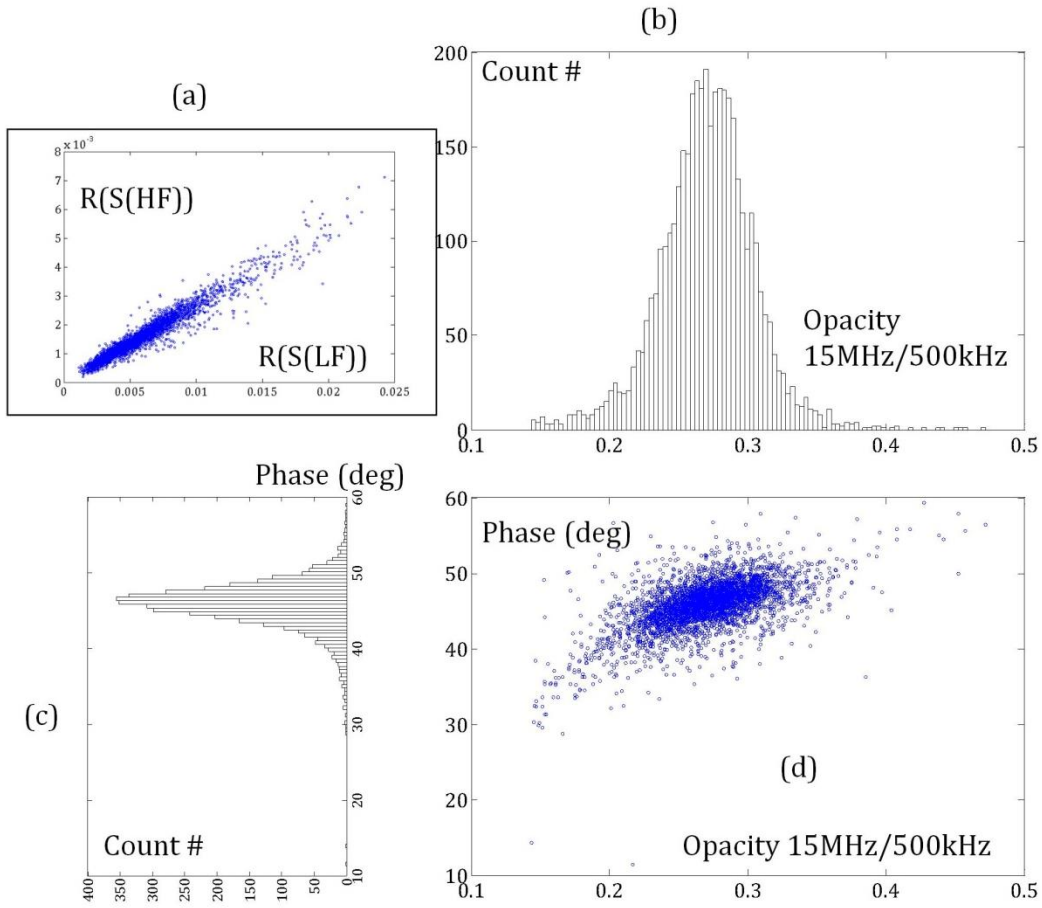

Figure 69. (a)In-phase signal at 500kHz(X axis) vs. in-phase signal at 15MHz. In (b) and (c) the opacity 15MHz/500kHz and phase at 8MHz for the data in (a) are shown. (d) Scatter plot of the histograms (b) and (c).

The detected signal opacity is homogeneous and the large samples' number makes the distribution look very similar to a normal probability density function.

Similarly, at the same time t=70 minutes, 2100 cells were measured from the cell suspension which was mixed with LLO at a concentration of 500 ng/mL for 10 minutes starting at t=0. It is clearly visible from Figure 70.a that the populations consist of two types of cells that respond differently to signals at the same frequency. The analysis of the scatter plot by projecting the histograms yields interesting results.

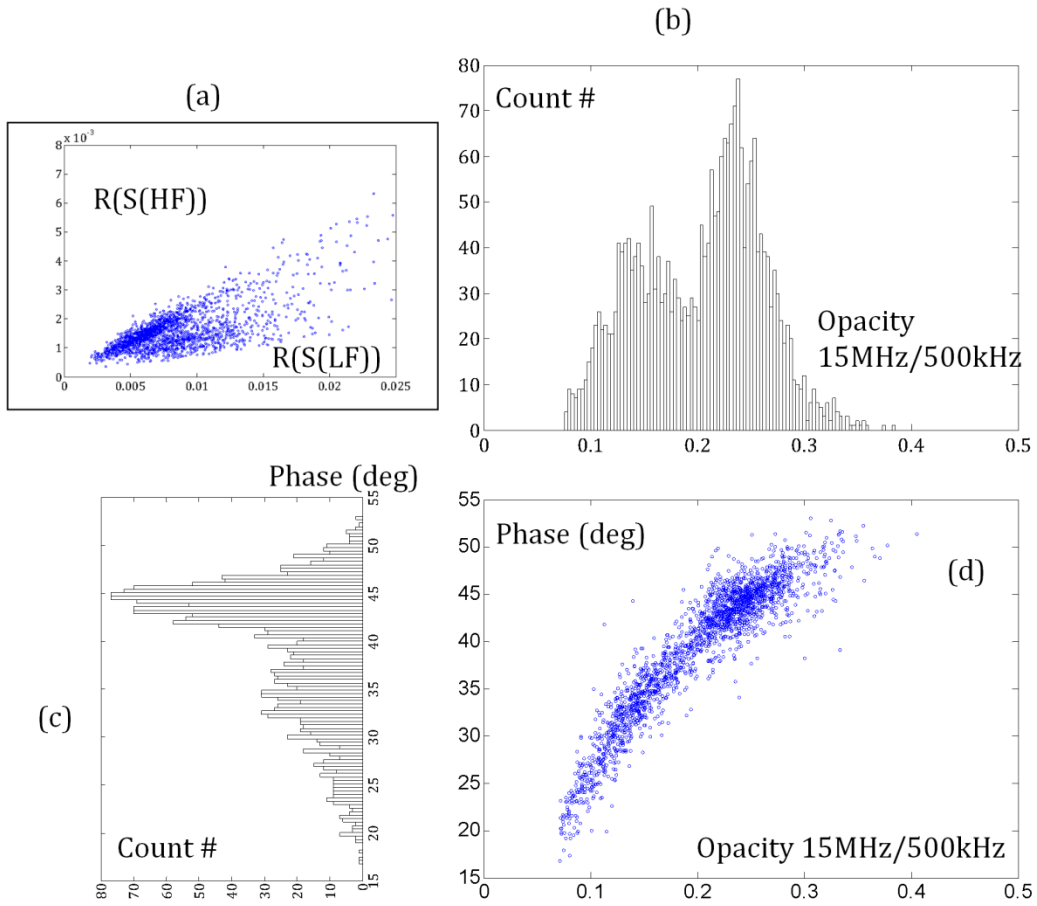

Figure 70. Compared to Figure 69.a from (a) the presence of a new population below the one of the healthy cells (less steep) is noticed. The histograms of the opacity in (b) and of the phase at 8 MHz (c) highlight the heterogeneous behavior. Scatter plot of phase and opacity in (d).

Again, the mixed population in Figure 70.b and Figure 70.c shows the same distributions indicated in Figure 68 . The new population at lower opacity is visible from the phase distribution as well.

To fit the data in Figure 70.d a Gaussian mixture model (GMM) was used via a Matlab built-in function. It makes use of the expectation maximization (EM) algorithm, which assigns posterior probabilities to each component density with respect to each observation. Clusters for data division are assigned by selecting the component that maximizes the posterior probability that a point has to belong to that cluster. The resulting mean opacities are 0.1364 and 0.2432 for cells subjected to the LLO insult ("leaky") and intact cells respectively. In the same order mean value for phases was 31.9 and 43.9 with a count

mixing proportion: 0.44 and 0.56. The posterior method returns also those posterior probabilities that indicate that each data point has some probability of belonging to each cluster. In Figure 71 the probability of each cell to belong to intact or damaged populations is indicated.

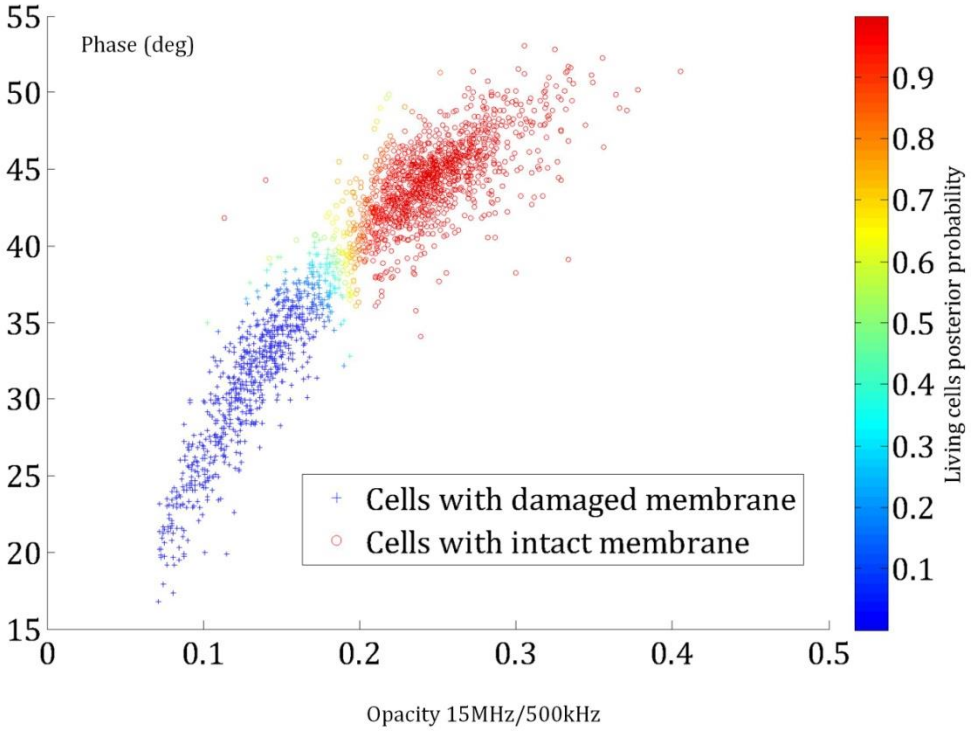

Figure 71. Partition of the data into two clusters using GMM. The cluster method assigns each point to one of the two components in the mixture distribution.

Figure 72 shows the detected intact cells subpopulation percentage over time detected by the procedure described above for each measurement. The very interesting fact is that when LLO is left in suspension for only the first 10 minutes, cell recovery was observed. In average 73.5% of cells were affected from the toxin and after 110 min from LLO introduction 60.3 % of cells was found to have the same opacity as control cells did.

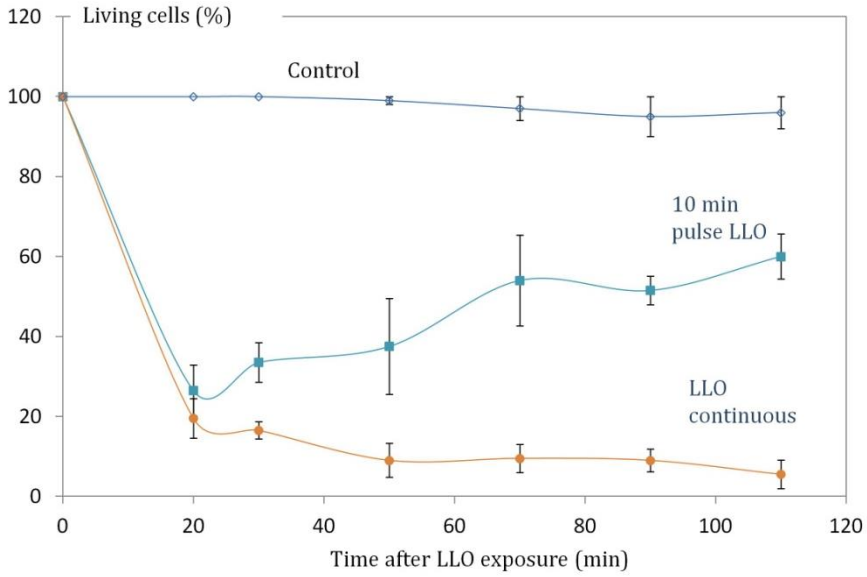

Figure 72. Ratio between viable and non-viable cells in two different experiments reproduced two times each. Pulsed LLO gives rise to membrane cell repair bringing back the dielectric properties of about 60% of cells to those of control samples. A finite in time effect of 10 min. for LLO is fundamental for the recovery to take place.

The results show a satisfying separation between the continuous LLO approach and the pulsed one. Percentages were obtained by considering the opacity and the phase at 8MHz.

5.10 Discussion

So far measurements showed that discrimination between injured cells from LLO and intact cells is possible. We clearly see an increase at both LF and HF signal amplitudes at different rate. This can be associated in a first approximation to an increase of cells' size when injured. Since the impedance measurement depends on the fraction between the cell volume and the volume of the measurement site small cell radius variations affect volume variation following a cubic law.

This phenomenon can be explained considering that when the cell membrane is incorporating the pore forming proteins, it becomes much more permeable and water flows inside as result of osmotic flow. The cells are swelling and their size increases. Since the

LF signal is proportional to the extracellular current thus directly related to the cell dimension this explains it increases after LLO is added as reported in Figure 67.

However, the cytosol osmolarity decreases during swelling because of water dilution. This decrease of osmolarity makes the cytosol less conductive; this is translated from an electrical point of view, as a decrease of the electrical opacity defined as HF/LF.

This hypothesis explains the overall decrease of opacity after induction. Yet, a sub-population of the cells remains intact; the rest is the "leaky" sub-population. When the cells are recovering, they have been able to remove the pores and their ion pump channels are re-establishing the good osmolarity. The size of the cell should also go back to normal and this explains the turnaround of the low frequency amplitude which starts to decrease after the LLO removal. In any case, no increase of cells' size could be detected optically by means of PI staining.

Incubating of cells during the experiment is for sure an advantage in terms of cells' culture optimal conditions. The drawback in this case is the fact that before performing the first impedance measurement we have to wait 10 min. for the toxin to make effect and 4 min of incubation during the trypsinisation procedure. If we add the time it takes to perform these procedures the result is that the first impedance measurement could be performed only after about 20 minutes from the LLO introduction. This is certainly not an advantage. In contrast, when using suspension of HeLa cells, measurements can be performed immediately after the toxin introduction. In this case an online monitoring of the LLO attack is possible.

Non adherent cells (e.g. K562, CHO, erythrocytes) can be taken in consideration for the toxicity monitoring by means of the flow cytometer.

5.11 Conclusions and outlook

The main objective of the study disclosed in this chapter was to develop an impedimetric method to measure single cell dielectric properties in continuous flow. To this end, the modeling of the chip (based on a previous design) by means of analytical and simulation software tools was initially shown. Then, the fabrication of the microfluidic devices by means of standard photolithography techniques was described. The electrical setup which features the possibility of performing measures at multiple discrete frequencies is one of the main achievements of this study. After a performance analysis of the electrical setup, measurements were accomplished with size calibrated microbeads and HeLa cells. The results showed a scarce capability of size discrimination for beads and cells. Measurements with cells indicate the relaxation frequency to be between 1MHz and 10MHz. A very good discrimination with no overlapping between beads and cells, in the opacity parameter, was possible.

The effect of LLO pore forming toxin was clearly detectable on HeLa cells. The toxin was added in suspension and in adherent cells and for the latter cell recovery after the toxin insult was also detectable. Cells could be kept in a controlled temperature and humidity environment during the resealing process. Monitoring of the dynamic cell response to the toxin is made possible by the multifrequencial measures which play a key role in terms of sensitivity offering the possibility to combine high and low frequency measures.

Some of the different aspects that can be considered for improving the cytometer are listed below:

(5) The plane of the electrodes can be elevated with respect to the glass substrate: for instance 10μm of height. This would permit to bring closer the electrodes' tips to the measurement channel preserving the homogeneity of the field lines in correspondence to the liquid electrodes surface. In this manner the sensitivity of the device would benefit from the measurement site volume diminishing.

(6) For particle sizing applications an array of liquid electrodes can be used upstream to the measuring site to combine impedance measurements with precise positioning of

microparticles within the microchannel by nDEP forces. This arrangement could reduce the dispersion of the measured amplitude (impedance variation) due to the particles positioning within the microchannel.

6 Conclusions

In this work we presented a design based on open microwell arrays for the automated continuous-flow sorting of single or small clusters of cells. The main feature of the proposed device is the parallel analysis of cell-cell and cell-particle interactions in each microwell of the array. High throughput sample recovery with a fast and separate transfer from the microsites to standard microtiter plates is also possible thanks to the chosen technology (Flexible PCB) which permits to produce cost effective large area arrays featuring geometries compatible with laboratory equipment.

The first presented approach for single-cell isolation into microwells was based on the accurate delivery of liquid volume in the range of 200pL by a piezoelectric droplet dispenser. A 3D model of the array surface was reconstructed using a procedure that interpolates the position of all the microwells in the array, starting from a subset of sampled microwells.

For a flexible substrate array of microsites, with 1536 microwells, the surface was reconstructed starting from a subset of only 24 sampled locations, where the largest absolute positioning error was found to be within ours specifications of 130 μm. The main feature of the proposed procedure is its speed which permits to execute a calibration in about 150 seconds compared to 9600 seconds required from a straightforward calibration carried out at each location. Additionally, the 3D reconstruction method can be easily adapted to devices with different geometrical features such as area and thickness.

As a final conclusion, we demonstrated that our procedure allows an automated system based on a motorized microscope, a camera and a drop-on demand single jet dispenser to provide an efficient fluidic interface for large area devices fabricated on flexible substrates fulfilling the initial specifications.

Due to operative problems mainly related to the recovery procedure speed, the approach based on piezoelectric external dispensing was replaced with another method which is in addition self-contained since it embeds the electrical field-based structures for individual isolating of a controlled number of cell/particles in suspension.

The isolation is performed in this new technique by negative dielectrophoretic forces which convey the particles' into the microwells. Particles such as cells and beads flow in electrically active microchannels on whose substrate the electrodes are patterned. The introduction of particles within the microwells is automatically performed by generating the required feedback signal by a microscope-based optical counting and detection routine.
In order to isolate a controlled number of particles we created two particular configurations of the electric field within the structure. The first one permits their isolation (*Load mode*) whereas the second one creates a net force which repels the particles from the microwell entrance – (*Forward mode*). Both configurations were modeled numerically by combining the effects of a focusing and a deflection stage in order to calculate the geometrical design parameters. The efficiency of the focusing and deflection stages was initially assessed in order to determine the range of operating signal amplitudes and fluid velocity. They were tested with different applied signals and fluid flow rates. Low conductivity buffers were used for these tests (σ = 0.15 S/m) and the frequency of the electric signals for nDEP forces is equal to 100KHz. *Forward mode* presents a yield of 100% for particle velocities higher than 60μm/s. The yield of the efficiency of the *Load mode* is about 93% in average for fluid velocities up to 80μm/s which represents the limit velocity for cell sedimentation into the microwells. The efficiency limit is determined by the impossibility of the optical detection routine to separate rotating cluster of two or more cells in adhesion.
For this reason and also for increasing the parallelism at which the cell-isolation function is implemented, a new structure based on coplanar electrodes to detect particle presence was designed. A lock-in scheme was used to monitor the impedance of the channel perturbed by flowing beads suspended in PBS (σ = 1.5 S/m). The module was also combined with the dielectrophoretic focusing stage situated upstream of the measurement stage, to study the dependence of the signal amplitude on the lateral position of the flowing 25μm beads. Choosing appropriate frequencies for focusing and sensing allows avoiding cross-talk between the signals. Focusing the particles in the middle of the channel leads to a reduction of the amplitude dispersion with coefficient of variation CV=11% which is quite small compared to the value obtained for random position particles (CV=50%).

The impedance spectroscopy technique for cell dielectric properties measurements was also used within a research project carried on at the EPFL (*École Polytechnique Fédérale de Lausanne*). A chip optimized for impedimetric measures with characteristic length of 20μm was fabricated using a simple single metal layer photolithography technique in the Center of Micro and Nanotechnology Institute (CMI) of EPFL.

After a characterization of the system performance, multifrequencial measurements were accomplished with size calibrated microbeads and HeLa cells. Multiple discrete frequency measures are performed in order to distinguish the different response of cells to the applied external electrical field at frequencies below and above the interfacial dispersion (β-dispersion). Measurements with cells indicate the β-dispersion frequency between 1MHz and 10MHz. Clear discrimination with no overlapping between beads and cells, in the opacity parameter, was possible.

The effect of a pore forming toxin (LLO) on HeLa cells was clearly distinguishable. Cells were exposed to the toxin and cell recovery after the toxin insult could be detected. Cells could be kept in a controlled temperature and humidity environment during the resealing process. This study enables the possibility to use a very simple fabrication process for disposable impedance based flow cytometers.

Pubblications

Journal articles:

E. Duqi, M. Bocchi, L. Giulianelli, N. Pecorari, E. Franchi Scarselli, R. Guerrieri, *FAST CALIBRATION OF A DISPENSER NOZZLE FOR DELIVERY OF MICRODROPLETS OVER A FLEXIBLE SUBSTRATE,* «Sensors and Actuators A: Physical», 2011, 168, pp. 320 – 327.

M. Bocchi, L. Rambelli, A. Faenza, L. Giulianelli, N. Pecorari, E. Duqi, R. Guerrieri, *INVERTED OPEN MICROWELLS FOR SINGLE-CELL TRAPPING, CELL-CELL INTERACTION ANALYSIS AND LIVE CELL FUNCTIONAL SORTING*, Lab Chip 2012, Under revision.

G. Mernier, E. Duqi, P. Renaud. *CHARACTERIZATION OF AN IMPEDANCE FLOW CYTOMETER USING LIQUID ELECTRODES*, Submitted to Lab Chip 2012.

Conference proceedings:

E. Duqi, A. Faenza, L. Giulianelli, N. Pecorari, L. Rambelli, N. Lopez, M. Bocchi, E. Franchi Scarselli, R. Guerrieri, *AUTOMATED ISOLATION OF A PROGRAMMABLE NUMBER OF CELLS INTO MICROWELLS USING DEP FORCES AND OPTICAL DETECTION*, Proceedings, The 6th International Conference on Microtechnologies in Medicine and Biology, 2011, pp. 1 - 2 (The 6th International Conference on Microtechnologies in Medicine and Biology, Lucerne (Switzerland), 4-6 May 2011)

A. Faenza, E. Duqi, N. Pecorari, L. Rambelli, L. Giulianelli, N. Lopez, M. Bocchi, R. Guerrieri, *CONTROLLED ISOLATION AND PATTERNING OF K562 LEUKEMIA CELLS USING ELECTRICALLY ACTIVATED MICROCHANNELS*, Proceedings, The 6th International Conference on Microtechnologies in Medicine and Biology, 2011, pp. 1 - 2 (The 6th International Conference on Microtechnologies in Medicine and Biology, Lucerne (Switzerland), 4-6 May 2011)

M. Bocchi, L. Rambelli, E. Duqi, A. Faenza, L. Giulianelli, N. Lopez, N. Pecorari, R. Guerrieri, *INVERTED OPEN MICROWELLS FOR ANALYSIS AND FUNCTIONAL SORTING OF SINGLE LIVE CELLS*, Proceedings, 2011, pp. 1722 - 1724 (15th International Conference on Miniaturized Systems for Chemistry and Life Sciences, MicroTAS 2011, Seattle, WA (USA), October 2-6, 2011)

Bibliography

(1) Abonnenc, M., Altomare, L., Baruffa, M., Ferrarini, V., Guerrieri, R., Iafelice, B., et al. (2005). Teaching cells to dance: The impact of transistor miniaturization on the manipulation of populations of living cells. *Solid State Electron*, 674–683.

(2) Allain, L., Askari, M., Stokes, D., & Vo-Dinh, T. (2001). Microarray sampling-platform fabrication using bubble-jet technology for a biochip system. *Fresenius J. Anal. Chem.*, 146-150.

(3) Allegro, S., Chanel, C., & Jacot, J. (1996). Autofocus for automated microassembly under a microscope. *International Conference On Image Processing Proceedings*, 677-680.

(4) Andersson, H., & Van der Berg, A. (2003). Microfluidic devices for cellomics: A review. *Sensors and Actuators: B*, 315-325.

(5) Andersson, H., Van der Wijngaart, W., Enoksson, P., & Stemme, G. (2000). Micromachined flow-through filter-chamber for chemical reactions on beads. *Sens. actuators*, 203-208.

(6) Arai, Y., Yasuda, R., Akashi, K., Harada, Y., Miyata, H., Kinosita, K., et al. (1999). Tying amolecular knot with optical tweezers. *Nature* , 446-448.

(7) Arnold, W. (2001). Positioning and levitation media for the separation of biological cells. *IEEE Transactions on Industry Applications*, 1468–1475.

(8) Ayliffe, A., Frazier, B., & R. R. (1999). Electric impedance spectroscopy using microchannels with integrated metal electrodes. *J. MEMS*, 50-57.

(9) Bassous, E., Taub, H., & Kuhn, L. (1977). Ink jet printing nozzle arrays etched in silicon. *AppL Phys. Lett.*, 135-137.

(10) Beebe, D., Mensing, G., & Walker, G. (2002). Physics and applications of microfluidics in biology. *Annual Review of Biomedical Engineering*, 261-286.

(11) Bocchi, M., Lombardini, M., Faenza, A., Rambelli, L., Giulianelli, L., Pecorari, N., et al. (2009). Dielectrophoretic trapping in microwells for manipulation of single cells and small aggregates of particles. *Biosensors and Bioelectronics*, 1177–1183.

(12) Bocchi, M., Rambelli, L., Faenza, A., Giulianelli, L., Pecorari, N., Duqi, E., et al. (2012). Inverted open microwells for single-cell trapping, cell-cell interaction analysis and live cell functional sorting. *Lab Chip*.

(13) Braschler, T., Demierre, N., Nascimento, E., Silva, T., Oliva, A., & Renaud, P. (2007). Continuous separation of cells by balanced dielectrophoretic forces at multiple frequencies. *Lab Chip*, 280-286.

(14) Braschler, T., Metref, L., Zvitov–Marabi, R., Van Lintel, H., Demierre, N., Theytaz, J., et al. (2007). A simple pneumatic setup for driving microfluidics. *Lab Chip*, 420-422.

(15) Bruus, H. (2007). *Theoretical microfluidics.* Oxford: Oxford University Press.

(16) Buhmann, M. (2000). Radial basis functions. *Acta Numer.*, 1-38.

(17) Carlson, R., Gabel, S., Chan, S., & Austin, R. (1997). Self-sorting of white blood cells in a lattice. *Phys. Rev. Lett*, 2149-2152.

(18) Cheung, K., Di Berardino, M., Schade-Kampmann, G., Hebeisen, M., Pierzchalski, A., Bocsi, J., et al. (2010). Microfluidic impedance-based flow cytometry:Theoretical and practical considerations. *Lab on chip, 77A*(7), 648-666.

(19) Clayton, J. (2005). Go with the microflow. *Nature Meth.*, 621-627.

(20) Cummings, E., & Singh, A. (2003). Dielectrophoresis in Microchips Containing Arrays of Insulating Posts: Theoretical and Experimental Results. *Anal. Chem.*, 4724–4731.

(21) De Gennes, P., Brochard-Wyart, F., & Quere, D. (2003). *Capillarity and wetting phenomena: drops, bubbles, pearls, waves.* New York: Springer.

(22) De Heij, B., Steinert, C., Sandmaier, H., & Zengerle, R. (2003). A tuneable and highly-parallel picolitre-dispenser based on direct liquid displacement. *Sensors and Actuators: A Physical*, 88-92.

(23) Demierre, N., Braschler, T., Linderholm, P., Seger, U., & Renaud, P. (2007). Characterization and optimization of liquid electrodes for lateral dielectrophoresis. *Lab Chip*, 355-365.

(24) Di Carlo, D., Aghdam, N., & Lee, L. (2006). Single-Cell Enzyme Concentrations, Kinetics, and Inhibition Analysis Using High-Density Hydrodynamic Cell Isolation Arrays. *Anal. Chem*, 4925–4930.

(25) Di Carlo, D., Wu, L., & Lee, L. (2006). Dynamic single cell culture array. *Lab Chip*, 1445-1449.

(26) Dittrich, P., & Manz, A. (2006). Lab-on-a-chip: microfluidics in drug discovery. *Nat Rev Drug Discov*, 210-218.

(27) Duffy, D., McDonald, J., Schueller, O., & Whitesides, G. (1998). Rapid prototyping of microfluidic systems in poly(dimethylsiloxane). *Anal. Chem*, 4974-4984.

(28) Duqi, E., Bocchi, M., Giulianelli, L., Pecorari, N., Franchi Scarselli, E., & Guerrieri, R. (2011). Fast calibration of a dispenser nozzle for delivery of microdroplets over a flexible substrate. *Sensors and Actuators A: Physical*, 320-327.

(29) Et Ali, J., Sorger, P., & Jensen, K. (2006). Cells on chips. *Nature*, 403-411.

(30) Faenza, A. (2011). *Microsystems for electronic positioning and monitoring of single cells and particles*. PhD thesis, Bologna: Research Doctorate in Electronics, Computer Science and Telecomunications.

(31) Feynman, R. (1992). There's plenty of room at the bottom. *Microelectromechanical Systems, Journal of*, 60-66.

(32) Foster, K., & Schwan, H. (1989). Dielectric properties of tissues and biological materials: a critical review. *Crit Rev Biomed Eng*, 25-104.

(33) Fredrickson, C., & Fan, Z. (2004). Macro-to-micro interfaces for microfluidic devices. *Lab Chip*, 526-533.

(34) Galanzha, E., Shashkov, E., Tuchin, V., Zharov, V., & . (2008). In vivo multispectral, multiparameter, photoacoustic lymph flow cytometry with natural cell focusing, label-free detection and multicolor nanoparticle probes. *Cytometry Part A*, 884-894.

(35) Gawad, S. (2004). Thesis:Dielectric spectroscopy in a microfabricated flow cytometer. *Lausanne, EPFL*.

(36) Gawad, S., Cheung, K., Seger, U., Bertsch, A., & Renaud, P. (2004). Dielectric spectroscopy in a micromachined flow cytometer. *Lab Chip*, 241-251.

(37) Gawad, S., Schild, L., & Renaud, P. (2001). Micromachined impedance spectroscopy flow cytometer for cell analysis and particle sizing. *Lab chip*, 76-82.

(38) Gilbert, R. (2010). Cholesterol-dependent cytolysins. *Adv Exp Med Biol*, 56-66.

(39) Gonzalez, M., Bischofberger, M., Freche, B., Ho, S., Parton, R., & Van der Goot, F. (2011). Pore-forming toxins induce multiple cellular responses promoting survival. *Cellular microbiology*, 1026-1043.

(40) Gravesen, P., Branebjerg, J., & Jensen, O. (1993). Microfluidics - a review. *J. Mioromech. Microeng.*, 168-182.

(41) Gravesen, P., Branebjerg, J., & Jensen, O. (1993). Microfluidics-a review. *Journal of Micromechanics and Microengineering*, 168-182.

(42) Hanai, T., Asami, K., & Koizumi, N. (1979). Dielectric theory of concentrated suspensions of shell-spheres in particular reference to the analysis of biological cell suspensions. *Bull. Inst. chem. Res.*, 297-305.

(43) Hoffmann, R., & Britt, W. (1979). Flow-system measurement of cell impedance properties. *J Histochem Cytochem*, 234-240.

(44) Holmes, D., & Morgan, H. (2010). Single cell impedance cytometry for identification and counting of CD4 T-cells in human blood using impedance labels. *Anal. Chem.*, 1455–1461.

(45) Jahnke, H., Rothermel, A., Sternberger, I., Mack, T., Kurz, R., Pänke, O., et al. (2009). An impedimetric microelectrode-based array sensor for label-free detection of tau hyperphosphorylation in human cells. *Lab chip*, 1422-1428.

(46) Jones, T. (1995). *Electromechanics of particles.* Cambridge: Cambridge University Press.

(47) Kennedy, C., Smith, D., Lyras, D., Chakravorty, A., & Rood, J. (2009). Programmed cellular necrosis mediated by the pore-Forming α-toxin from Clostridium septicum. *PLoS Pathog*, e1000516.

(48) Koch, M., Evans, A., & Brunnschweiler, A. (1999). Design and fabrication of a micromachined Coulter counter. *J. Micromech. Microeng.*, 159-161.

(49) Koltay, P., Steger, R., Bohl, B., & Zengerle, R. (2004). The dispensing well plate: a novel nanodispenser for the multiparallel delivery of liquids(DWP Part 1). *Sensors and Actuators: A Physical*, 483-491.

(50) Krinke, D., Jahnke, H., Mack, T., Hirche, A., Striggow, F., & Robitzki, A. (2010). A novel organotypic tauopathy model on a new microcavity chip for bioelectronic label-free and real time monitoring. *Biosensors and Bioelectronics,* 162-168.

(51) Kuttel, C., Nascimento, E., Demierre, N., Silva, T., Braschler, T., Renaud, P., et al. (2007). Label-free detection of Babesia bovis infected red blood cells using impedance spectroscopy on a microfabricated flow cytometer. *102*, 63-68.

(52) Lee E, K. L. (2006). Forensic visualization of foreign matter in human tissue by near-infrared spectral imaging: Methodology and data mining strategies. *Cytometry Part A*, 888–896.

(53) Lee, P., Hung, P., Shaw, R., Jan, L., & Lee, L. (2005). Microfluidic application-specific integrated device for monitoring direct cell-cell communication via gap junctions between individual cell pairs. *Appl. Phys. Lett.*, 86, 223902.

(54) Linderholm, P., & Renaud, P. (2005). Comment on 'AC frequency characteristics of coplanar impedance sensors as design parameters'. *Lab Chip*, 270-279.

(55) Linderholm, P., Braschler, T., Vannod, J., Barrandon, Y., Brouard, M., & Renaud, P. (2006). Two-dimensional impedance imaging of cell migration and epithelial stratification. *Lab Chip*, 1155-1162.

(56) Linderholm, P., Seger, U., & Renaud, P. (2006). Analytical expression for electric field between two facing strip electrodes in microchannel. *Electron Lett IEE*, 145-147.

(57) Malleo, D., Nevill, J., Lee, L., & Morgan, H. (2009). Continuous differential impedance spectroscopy of single cells . *Microfluid Nanofluid*, 191-198.

(58) Meissner, R., Eker, B., Kasi, H., Bertsch, A., & Renaud, P. (2011). Distinguishing drug-induced minor morphological changes from major cellular damage via label-free impedimetric toxicity screening. *Lab Chip*, 2352-2361.

(59) Mernier, G., Duqi, E., & Renaud, P. (2012). Characterization of liquid electrodes for flow cytometry. *Lab Chip*, In submission.

(60) Morgan, H., & Green, N. (2002). *AC electrokinetics: colloids and nanoparticles.* Hertfordshire(UK): Research Studies Press Ltd.

(61) Motchenbacher, C., & Connely, J. (1993). *Low-noise electronic system design.* New York: John Wiley &sons.

(62) Nelson, K., Robert, A., & Buckley, J. (1999). Channels formed by subnanomolar concentrations of the toxin aerolysin trigger apoptosis of T lymphomas. *Cellular Microbiology*, 69-74.

(63) Olthuis, W., Streekstra, W., & Bergveld, P. (1995). Theoretical and experimental determination of cell constants of planar interdigitated electrolyte conductivity sensors. *Sens. Actuators. B*, 252-256.

(64) Pamme, N. (2007). Continuous flow separations in microfluidic devices. *Lab Chip*, 1644-1659.

(65) Rettig, J., & Folch, A. (2005). Large-Scale Single-Cell Trapping And Imaging Using Microwell Arrays. *Anal. Chem.*, 5628–5634.

(66) Rosenthal, A., & Voldman, J. (2005). Dielectrophoretic traps for single-particle patterning. *Biophysical Journal*, 2193–2205.

(67) Saunders, R., Gough, J., & Derby, B. (2008). Delivery of human fibroblast cells by piezoelectric drop-on-demand inkjet printing. *Biomaterials*, 193-203.

(68) Schnelle, T., Hagedorn, R., Fuhr, G., Fiedler, S., & Müller, T. (1993). Three-dimensional electric field traps for manipulation of cells - calculation and experimental verification. *Biochim. Biophys. Acta*, 127-140.

(69) Schwan, H. (1957). Electrical properties of tissue and cell suspensions. *Adv. Biol. Med.Physics*, 147-209.

(70) Schwann, H. (1957). Electrical properties of tissue and cell suspensions. *Adv. Biol. Med.Physics*, 147-209.

(71) Schwann, H. (1983). Electrical properties of blood and its constituents:alternating current spectroscopy. *Blut*, 185-197.

(72) Skelley, A., Kirak, O., Suh, H., Jaenisch, R., & Voldman, J. (2009). Microfluidic control of cell pairing and fusion. *Nat Methods*, 147-152.

(73) Stephens, D., & Pepperkok, R. (2001). The many ways to cross the plasma membrane. *Proc. Natl. Acad. Sci. U. S. A.*, 4295-4298.

(74) Sun, T., & Morgan, H. (2010). Single-cell microfluidic impedance cytometry: a review. *Microfluid Nanofluid*, 423-443.

(75) Sun, Y., Duthaler, S., & Nelson, B. (2004). Autofocusing in computer microscopy: selecting the optimal focus algorithm. *Microsc. Res. Techn.*, 139-149.

(76) Taff, B., & Voldman, J. (2005). A Scalable Addressable Positive-Dielectrophoretic Cell-Sorting Array. *Anal. Chem.*, 7976-7983.

(77) Tan, W., & Takeuchi, S. (2007). A trap-and-release integrated microfluidic system for dynamic microarray applications. *Proc. Natl. Acad. Sci*, 1146-1151.

(78) Terry, S., Jerman, J., & Angell, J. (1979). A gas chromatographic air analyzer fabricated on a silicon wafer. *IEEE Trans. Electron Devices*, 1880-1886.

(79) Walev, I., Bhakdi, S., Hofman, F., Djonder, N., Valeva, A., & Aktories, K. (2001). Delivery of proteins into living cells by reversible membrane permeabilization with streptolysin-O. *Proc Natl Acad Sci USA*, 3185-3190.

(80) Watson DA, B. L. (2008). A flow cytometer for the measurement of Raman spectra. *Cytometry Part A*, 119–128.

(81) Whitesides, G. (2006). The origins and future of microfluidics. *Nature*, 368-373.

(82) Zheng, S., Lin, H., JQ, L., Balic, M., Datar, R., Cote, R., et al. (2007). Membrane microfilter device for selective capture, electrolysis and genomic analysis of human circulating tumor cells. *21st InternationalSymposium on Miroscale Bioseparations*, 154.